12-18-2013

Coronary Artery Calcium Quantification in Contrast-enhanced Computed Tomography Angiography

Abinashi Dhungel
Georgia State University

CORONARY ARTERY CALCIUM QUANTIFICATION IN CONTRAST-ENHANCED COMPUTED TOMOGRAPHY ANGIOGRAPHY

by

ABINASHI DHUNGEL

Under the Direction of Dr. Michael Weeks

ABSTRACT

Coronary arteries are the blood vessels supplying oxygen-rich blood to the heart muscles. Coronary artery calcium (CAC), which is the total amount of calcium deposited in these arteries, indicates the presence or the future risk of coronary artery diseases. Quantification of CAC is done by using computed tomography (CT) scan which uses attenuation of x-ray by different tissues in the body to generate three-dimensional images. Calcium can be easily spotted in the CT images because of its higher opacity to x-ray compared to that of the surrounding tissue. However, the arteries cannot be identified easily in the CT images. Therefore, a second scan is done after injecting a patient with an x-ray opaque dye known

as contrast material which makes different chambers of the heart and the coronary arteries visible in the CT scan. This procedure is known as computed tomography angiography (CTA) and is performed to assess the morphology of the arteries in order to rule out any blockage in the arteries.

The CT scan done without the use of contrast material (non-contrast-enhanced CT) can be eliminated if the calcium can be quantified accurately from the CTA images. However, identification of calcium in CTA images is difficult because of the proximity of the calcium and the contrast material and their overlapping intensity range. In this dissertation first we compare the calcium quantification by using a state-of-the-art non-contrast-enhanced CT scan method to conventional methods suggesting optimal quantification parameters. Then we develop methods to accurately quantify calcium from the CTA images. The methods include novel algorithms for extracting centerline of an artery, calculating the threshold of calcium adaptively based on the intensity of contrast along the artery, calculating the amount of calcium in mixed intensity range, and segmenting the artery and the outer wall. The accuracy of the calcium quantification from CTA by using our methods is higher than the non-contrast-enhanced CT thus potentially eliminating the need of the non-contrast-enhanced CT scan. The implications are that the total time required for the CT scan procedure, and the patient's exposure to x-ray radiation are reduced.

INDEX WORDS: Coronary artery calcium, Quantification, Computed tomography angiography, Automatic vessel extraction

CORONARY ARTERY CALCIUM QUANTIFICATION IN CONTRAST-ENHANCED COMPUTED TOMOGRAPHY ANGIOGRAPHY

by

ABINASHI DHUNGEL

A Dissertation Submitted in Partial Fulfillment of the Requirements for the Degree of

Doctor of Philosophy

in the College of Arts and Sciences

Georgia State University

2013

CORONARY ARTERY CALCIUM QUANTIFICATION IN CONTRAST-ENHANCED COMPUTED TOMOGRAPHY ANGIOGRAPHY

by

ABINASHI DHUNGEL

Committee Chair: Michael Weeks

Committee: Saeid Belkasim

Robert Harrison

Mukesh Dhamala

Zhen Qian

Electronic Version Approved:

Office of Graduate Studies

College of Arts and Sciences

Georgia State University

December 2013

DEDICATION

I dedicate this dissertation to my wife Carina,

my parents Rajaram and Geeta,

and my sisters Laxmi and Pooja.

ACKNOWLEDGEMENTS

I would like to express my deepest gratidute to my advisor, Dr. Michael Weeks whose continuous support and guidance made this dissertation possible. He has always been very patient and kind, has inspired me to learn, and helped me develop confidence in shaping my ideas into research works. He always believed in me, kept me motivated, and inspired me to be an independent thinker.

I would like to express my thanks to my committee members Dr. Saeid Belkasim, Dr. Robert Harrison, Dr. Mukesh Dhamala, and Dr. Zhen Qian whose guidance and constructive feedbacks have been key to shaping the dissertation. Dr. Zhen Qian introduced me to the field of medical imaging and provided me with copious oppertunities to work in this field.

My thanks also goes to the Department of Computer Science for providing financial support and an excellent platform for conducting my PhD studies and research, Neuroscience Institute at Georgia State University for the financial support, and Piedmont Heart Institute for providing me internship oppertunity and a chance to work in the area of medical imaging.

The dream of my parents and sisters to see me as an educated man, always kept me encouraged and move forward. Their continuous love and support helped me to achieve success at every step of my life.

Finally, I would never have been able to finish the dissertation without the support of my lovely wife Carina. She always stood by me, provided me courage, and cheered me up. She has been extremely patient, supportive and been a part of everything including the smallest things in my life.

TABLE OF CONTENTS

LIST OF TABLES

LIST OF FIGURES

LIST OF ABBREVIATIONS

- CAC - Coronary Artery Calcium
- CAD - Coronary Artery Disease
- CT - Computed Tomography
- CTA - Computed Tomography Angiography
- RCA - Right Coronary Artery
- LAD - Left Anterior Descending
- LCx - Left Circumflex
- HU - Hounsfield Unit
- 2D - Two-dimensional
- 3D - Three-dimensional
- IVUS - Intravascular Ultrasound
- VH - Virtual Histology
- LAD - Left Anterior Descending
- CACS - Coronary Artery Calcium Score
- k-NN - k-Nearest Neighbor
- PDM - Point Distribution Model
- PCA - Principal Component Analysis
- PPV - Positive Predictive Value

- NPV - Negative Predictive Value
- ROC - Receptor Operative Curve
- LoG - Laplacian of Gaussian
- MRA - Magnetic Resonance Angiography
- MRI - Magnetic Resonance Imaging
- SHAPE - Screening for Heart Attack Prevention and Education
- PDF - Probability Density Function
- GVF - Gradient Vector Flow
- GUI - Graphical User Interface
- COW - Correlation Optimized Warping
- HM - Harmonic Mean

CHAPTER 1

INTRODUCTION

Coronary artery calcium (CAC) scoring is done to quantify the total calcium deposited in the coronary arteries which are the blood vessels supplying oxygen-rich blood to the heart muscle. The assessement of CAC score is important as the deposition of calcium in the arteries is highly indicative of the presence or the future risk of coronary artery diseases(CAD).

The CAC scoring is done by using a computed tomography (CT) scan which uses x-rays for imaging and three dimensional visualization of different anatomical organs. Calcium can be easily spotted in the CT images because of its higher opacity to x-ray compared to that of the surrounding tissue. However, the arteries and other coronary structures cannot be identified easily in the CT images. Therefore an x-ray opaque dye known as contrast material is injected to a patient and a second CT scan is done. The contrast material circulates through the heart, and the coronary arteries and different chambers of the heart can be easily identified in the CT scan. This procedure is known as computed tomography angiography (CTA) and is performed to assess the morphology of the arteries in order to rule out the blockage or abnormalities in the artery.

The CT scan done without the use of contrast material (non-contrast-enhanced CT) for the purpose of CAC scoring can be eliminated if the total amount of calcium can be accurately calculated from the contrast-enhanced CTA images. The implication being that the total time required for the CT scan procedure is reduced and more importantly the patient's exposure to x-ray radiation is reduced. Identification of the calcium is difficult in the CTA images since the contrast material circulating in the blood has an intensity that which overlaps with the intensity range of the calcium. In this work, first we present a comparative study of the calcium quantification by using a state-of-the-art non-contrast-

enhanced CT scan to conventional methods suggesting appropriate parameters for optimal calcium quantification. We then develop methods to accurately quantify calcium from the CTA images by estimating the probability of calcium voxels in the overlapped intensity range. We develop novel algorithms for extracting centerline of an artery, calculating the threshold of calcium adaptively based on the intensity of contrast along the artery, calculating the amount of calcium in mixed intensity range, and segmenting the artery and the outer wall. The accuracy of the calcium quantification from CTA by using our methods is higher than the non-contrast-enhanced CT thus potentially eliminating the need of the non-contrast-enhanced CT scan. The implications are that the total time required for the CT scan procedure, and the patient's exposure to x-ray radiation are reduced.

1.1 Coronary Anatomy and Atherosclerosis

Arteries are the blood vessels that supply oxygen-rich blood to different parts of the body. Arteries that supply blood to the heart muscle are known as the coronary arteries. Figure 1.1 shows two coronary arteries, the right coronary artery (RCA) and the left coronary artery branching out from a larger artery known as aorta which supplies blood to the other parts of the body [1]. As can be seen from the figure, the left coronary artery branches into the circumflex artery(LCx) and the left anterior descending (LAD) artery.

Atherosclerosis is a disease caused by plaque build-up in the arterial wall and is the most common cause of a dangerous cardiac event such as heart attack [3]. Plaque is made up of lipid, fibrous tissues, calcium etc. which builds up over time and narrows the internal space of artery known as lumen. Figure 1.2 shows the narrowing of artery which is also known as stenosis. A plaque can rupture inside an artery causing blood to clot on the ruptured surface. Heart attack or myocardial infarction is a life-threatening condition occurring when a large clot completely blocks the artery and the heart muscle dies because of lack of oxygen-rich blood [4]. Sometimes, the plaque may continue to build-up over several years and may completely block one of the coronary arteries leading to heart attack [4].

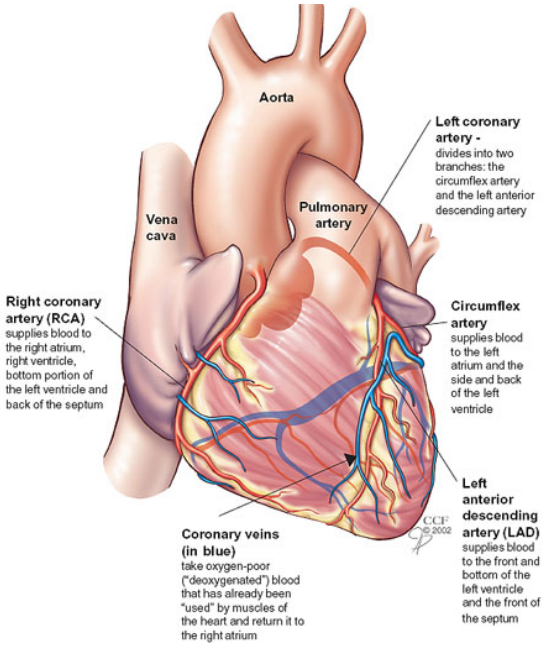

Figure 1.1 The heart and different coronary arteries. Picture adapted from [1]

.

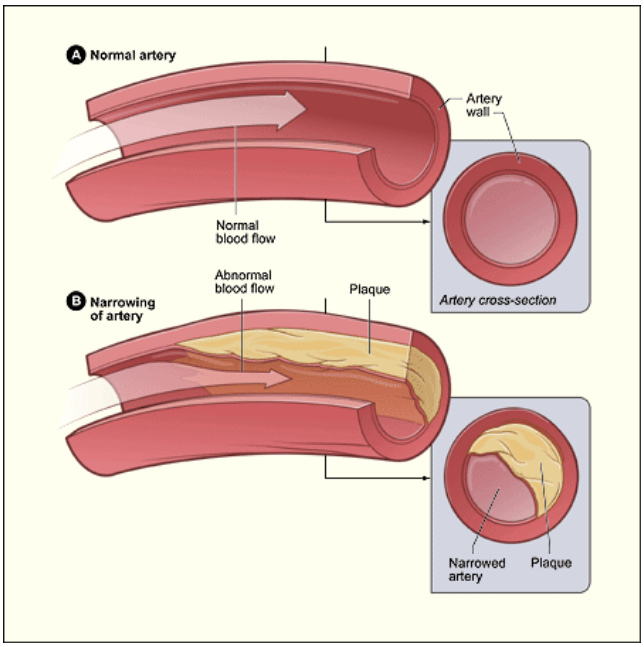

Figure 1.2 Narrowing of an artery due to plaque buildup. Picture adapted from [2].

The rupture prone or fast progressing plaques are also known as vulnerable plaques and the slower progressing ones are known as stable plaques [5]. The stable plaque results in its own complication called myocardial ischemia which reduces the blood flow to a part of heart resulting in slow death of heart tissue and decreased efficiency of blood circulation [6]. The composition of plaque is often divided into four different types of tissues called fibrous, fibrofatty, necrotic core and the calcified tissue [7].

The presence of calcified tissue or the calcium in coronary arteries is closely associated with the total atherosclerotic burden and is indicative of future cardiovascular diseases [3, 5, 8]. In this work, we are concerned with the detection and quantification of the calcium by using the computed tomography (CT) imaging.

1.2 Computed Tomography Imaging

Computed Tomography (CT) is used to generate images of different internal anatomical structures of a person. A CT scanner has a source that generates an x-ray beam which after passing through the patient's body is detected and converted into an electric signal by a detector array. As the x-ray passes through the patient's body, the photons constituting the x-ray beam are scattered or absorbed depending upon the initial x-ray energy as well as the tissue density. This reduction of x-ray beam is known as attenuation, and its numerical value is calculated from the electric signal produced by the detector array. The attenuation value is measured upon the strength of x-ray beam. Hence a relative attenuation value is obtained by calibrating the attenuation value of water to 0. The relative attenuation coefficient is measured in Hounsfield unit (HU) as follows, [9]

$$C = \frac{\mu - \mu_{water}}{\mu_{water}} \times 1000HU, \tag{1.1}$$

where C is the relative attenuation coefficient and μ is the actual attenuation coefficient in HU. High density tissues attenuate the x-ray beam more than low density tissues and have higher HU values. The x-ray generated by the source is restricted to a fan-shaped beam of

$45 - 60°$ angular width by a collimator which is a device to align an x-ray beam in a certain shape or direction. A second collimator placed perpendicular to the first collimator restricts the x-ray into a thin beam so that the x-ray passes through a thin slice of the patient's body. Both the source and the detector array revolve around the patient's body projecting x-ray at different angles, so that a slice in a patient body produce multiple projections in the detector array. These multiple projections are then reconstructed into an image of a single cross-sectional slice of the body. Multiple slices are obtained by moving the patient table forward to cover a desired portion of the body such as abdomen, chest etc. The final CT data is thus a 3-D data volume composed of tiny units called voxels represented by the attenuation coefficients in HU.

1.2.1 Coronary artery calcium (CAC) quantification and its clinical utility

The quantification of coronary artery calcium was first done by Agatston et al. [10] in 584 subjects, 475 among which did not have any coronary artery disease. Twenty contiguous slices, each with 3 mm thickness were acquired using an ultrafast computed tomographic scanner. The total calcium score was calculated by considering the area of each calcified plaque also known as a lesion and the peak intensity value in each plaque. A contiguous group of pixels in a slice was considered as a calcified lesion, if each pixel in the group was 130 HU or more and the total area of all the pixels in the group $>= 1mm^2$. If the peak intensity of a lesion was in the range 130 to 199 a density score of 1 was assigned. Similarly the density scores of 2 for the range of 200 to 299, 3 for the range 300 to 399 and 4 for peak $>= 400$ were assigned. The sum of all lesion scores which was obtained by multiplying the area of each lesion with the density score then gave the total calcium score. If there were no calcified lesions then the calcium score of 0 was assigned. The total calcium score was found to increase with age and patients with coronary artery diseases had significantly higher calcium scores than those without in all age groups considered ($p < 0.0001$).

The coronary artery calcium (CAC) score has been shown to be associated with the risk of future cardiovascular events in numerous studies. One such study done in 25,253 in-

dividuals without any coronary disease symptoms demonstrated CAC to be an independent predictor of mortality [8]. Other studies proved that it can predict future cardiovascular events independent of age, sex and race. Although the prevalence of calcium differs significantly with different race, age groups and gender [11, 12], CAC predicts future cardiovascular events independent of age, sex and race [13].

1.2.2 Computed Tomography Angiography

The coronary artery calcium (CAC) score of 0 indicates the absence of any calcified plaques and is associated with a very low risk of future cardiovascular events in the case of patients without any cardiovascular heart disease symptoms [14]. However, a CAC score of 0 is not sufficient to rule out the presence of non-calcified plaques in patients with symptoms as these plaques are not visible in non-contrast-enhanced CT. Several studies have reported the occurrence of obstructive (causing more than 50% stenosis) non-calcified plaques in symptomatic patients with 0 CAC [15, 16]. Computed tomography angiography (CTA) is done in symptomatic patients in order to assess a suspected coronary artery disease. CTA is done by injecting a contrast agent in blood. A contrast agent has relatively higher opacity to x-ray as compared to the opacity of soft tissues such as muscle, arterial wall etc. and is clearly visible in the CT image. With the contrast agent in the blood CTA allows the visualization of the coronary arteries and any stenosis can be easily detected. However, some of the calcified plaques might be obscured due to the presence of high opacity contrast agent. Both the contrast-enhanced CTA and non-contrast-enhanced CAC scoring are hence performed in conjunction.

1.3 Coronary artery calcium quantification using contrast-enhanced CTA

Injecting the contrast material helps to visualize the arteries clearly since the contrast material is opaque to the x-ray. However, some of the low density calcium the intensity range of which overlap with the intensity range of contrast material may not be visible in the CTA. Figures 1.3 (a) and 1.3 (b) show a slice from non-contrast-enhanced and contrast-

enhanced CT scans respectively. Both the scans were obtained from the same patient and approximately shows the same portion in the artery. In the non-contrast-enhanced figure, the calcium can be easily seen and can be extracted easily by using a fixed cutoff threshold such as 130 HU. The contrast-enhanced figure easily visualizes the arteries and larger vessels which contain blood dyed with the injected contrast agent. However some of the low density calcium have the same intensity as the contrast agent and may be inseparable by using a single cutoff threshold.

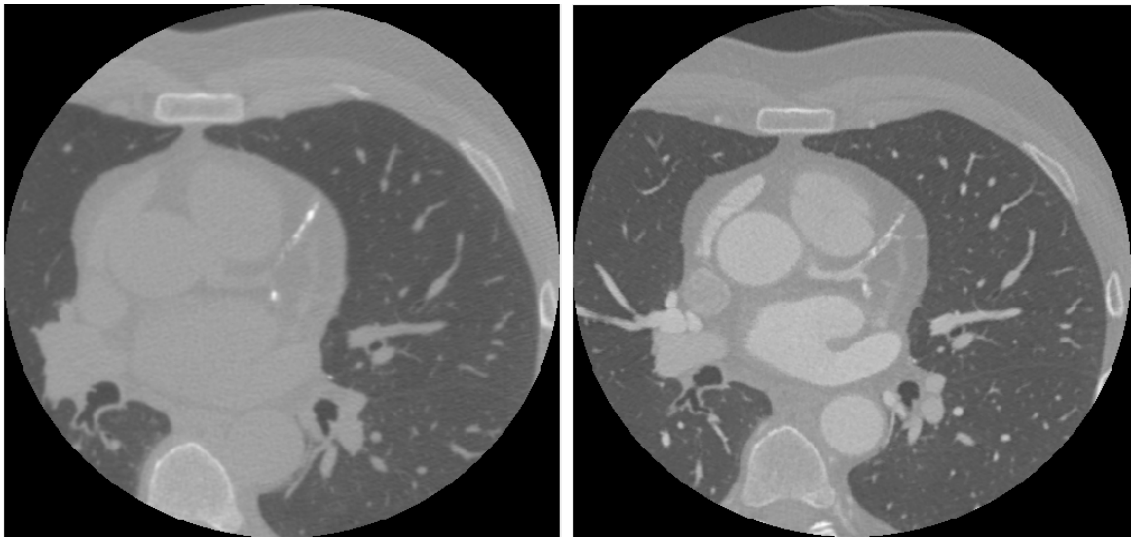

(a) (b)

Figure 1.3 A slice from (a) non-contrast-enhanced CT scan (b) contrast-enhanced CT scan of the same patient.

Coronary artery calcium quantification by using contrast-enhanced CTA has been attempted by several studies recently [17, 18, 19, 20, 21, 22, 23]. Most of these studies use a higher cutoff threshold such as 320 HU [17], 350 HU [21, 22] or even 600 HU [23] in order to separate the high density calcium from the contrast material. A single cutoff threshold is not appropriate for all the CTA data as the cutoff threshold should be proportional to the peak HU intensity level of the contrast. The peak HU intensity level depends upon factors such as patient physiology, contrast injection rate, contrast concentration, time elapsed since contrast administration, image noise etc. [24]. In chapter 5, we also observed the peak

contrast intensity differs not only for different patients but also for different arteries of a patient, and along the length of artery. Therefore use of a fixed cutoff threshold results in inaccuracies in calcium quantification. For example, a threshold of 350 HU overestimated the total calcium in [22], whereas the same threshold resulted in the underestimation of total calcium in [21]. In order to address this issue, adaptive cutoff thresholds have also been calculated based on the intensity profile of an artery [18, 19]. However, none of these methods make an attempt to separate calcium and the contrast in the overlapped intensity range and calculate artery-length adaptive cutoff thresholds.

1.4 IVUS-VH imaging technique used for detecting plaque

The intravascular ultrasound derived Virtual Histology^{TM} (Volcano Corporation) (IVUS-VH) is a clinically established method for characterization of different kind of plaque tissue. The IVUS-VH can detect four different kinds of plaque tissues, namely, fibrous, fibrofatty, necrotic, and dense calcium and visualize them with different color codes as shown in figure 6.1. The figure shows a frame of IVUS-VH obtained from the same patient whose non-contrast-enhanced and contrast-enhanced CT scans are shown in figures 1.3 (a) and 1.3 (b) respectively.

In IVUS-VH the images are formed by ultrasound waves. A catheter travels through artery emitting ultrasound waves which gets reflected from the arterial wall. The amplitude of the reflected waves are used to construct images of different layers of the arterial wall. The frequency of the reflected waves are used to classify different tissue components and different colors are assigned to these components. The white pixels are dense calcium, red ones correspond to the necrotic core, light-green are fibrofatty and green are fibrous tissues. The particular frame in figure 6.1 shows a highly calcified plaque which is found in an arterial wall in the proximity to the lumen.

The IVUS-VH has been shown to analyze different components with very high predictive accuracies. Nasu et al. demonstrated the accuracy of IVUS-VH by first obtaining IVUS-VH images from inside the arteries and then by comparing the color-coded tissue components

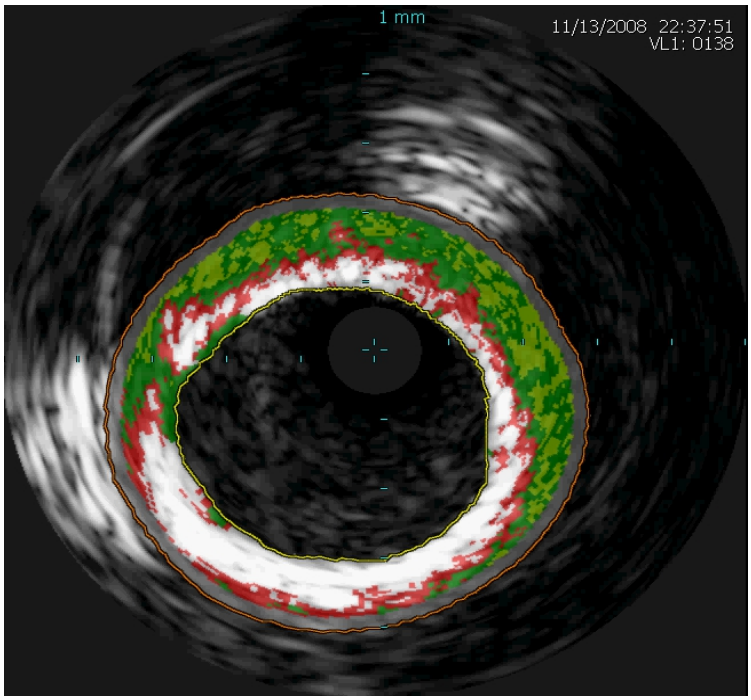

Figure 1.4 A frame of IVUS-VH showing different plaque components.

in the images with actual histology of the plaque tissues obtained by a procedure called directional coronary atherectomy [25]. The directional coronary atherectomy is a medical intervention to remove the arterial blockage by cutting away the plaque tissue from inside an artery. In another study by Nair et al. the IVUS-VH images were compared against the histology of the plaque tissue obtained from the arteries cut from dead subjects [7]. Both the studies reported the IVUS-VH to have a predictive accuracy of more than 96% for dense calcium. Therefore, we used the IVUS-VH in our preliminary study to assess the accuracy of the quantification of calcium from non-contrast-enhanced CT scan.

1.5 Dissertation Organization

The rest of the dissertation is organized as follows. In chapter 2 we present a review of recent literature of several different approaches used in quantifying calcium from the contrast-enhanced CTA and analyze their drawbacks. Chapter 3 presents the preliminary work of calcium quantification in non-contrast-enhanced CT scan. Although, the quantifica-

tion in non-contrast-enhanced CT is extensively studied, we present the study by using scans obtained from a state-of-the-art CT scanner which allows reconstruction with 0.5 mm slice thickness. We compare the calcium quantification by using 0.5 mm and the conventional 3.0 mm slice thickness reconstruction widths at different cutoff thresholds. We report several important findings such as for optimal calcium quantification by using 0.5 mm slice thickness reconstruction the cutoff threshold should be increased to 226 HU from the conventional threshold of 130 HU. We also found that optimal cutoff threshold has a high correlation with the noise level of the CT scan in 0.5 mm non-contrast-enhanced CT.

In chapter 4, we use the eigenvalues of Hessian matrix to automatically extract artery as well as the centerline of the artery. For finding the centerline, the distance transform of the extracted artery is considered. The centerline extracted in chapter 4 is used for finding a set of voxels located at its certain distance (3 to 5 mm) by using morphological operations. These voxels are then statistically analyzed for finding an appropriate cutoff threshold for quantifying high-density calcium in chapter 5. Calcium voxels in the overlapped intensity range with the contrast voxels consist of low-density calcium in the vicinity of high-density calcium as will be seen in chapter 5. Algorithms for finding both the low-density calcium and and adaptive cutoff threshold for high-density calcium are developed in chapter 5. Chapter 6 validates the calcium quantified from the contrast-enhanced CTA by comparing it with the IVUS-VH derived calcium volume and also compares the CTA calcium quantification with the non-contrast-enhanced CT quantification. In chapter 7 we present a method for segmenting the artery lumen and its surrounding wall based on the expectation maximization method [26]. In chapter 8 we summarize our work and identify possible improvements.

1.6 Dissertation Statement

In this dissertation we find an optimal cutoff threshold for quantifying calcium from non-contrast-enhanced computed tomography (CT) by using a state-of-the-art CT scanner and compare it with the conventional method of calcium quantification. We develop novel algorithms to calculate the total volume of coronary artery calcium from contrast-enhanced

computed tomography angiography (CTA) which includes an automatic centerline extraction algorithm, and a novel segmentation method based on expectation maximization algorithm to segment the artery lumen and its surrounding tissues. The implication of the dissertation is in the reduction of radiation dose to a patient by eliminating the need of the non-contrast-enhanced CT for calcium scoring as the method developed by using CTA performs a more accurate quantification than the non-contrast-enhanced CT.

1.7 Published works

The preliminary work of calcium quantification from non-contrast-enhanced CT has been published as a conference paper [27] and an abstract [28] in which we have found thresholds for optimal quantification of calcium volume in CT volume by validating against the IVUS-VH derived calcium volume. Another abstracts [29] shows that the calcium volume quantified with thinner slice thickness of 0.5 mm has better accuracy than the 3.0 mm slice thickness CT volume. We have also performed a detailed comparison of these two different slice thickness in terms of various statistical measures which is presented in chapter 3 and has been extended to a journal draft which is under review at the time of the dissertation writing. The abstract of calcium quantification by using contrast-enhanced CTA is published in [30] which also compares the accuracy with the non-contrast-enhanced CT. A detailed methodology for calcium quantification, from the CTA by automatically extracting arteries and statistical analysis of the voxels are presented in chapters 4, 5, and 6 which are unpublished but present novel ideas potentially contributing to several publications in future.

Although not directly related to the work presented in the dissertation, we have studied several areas during the course of Ph.D. These include quality measurement of wavelet based video compression published in [31], a novel video quality assessment method published in [32], and acceleration of a filtering algorithm in manycore and multicore architecture published in [33].

CHAPTER 2

CALCIUM QUANTIFICATION FROM COMPUTED TOMOGRAPHY ANGIOGRAPHY : LITERATURE REVIEW

Calcium quantification is commonly done by using three different scoring methods : the Agatston score [10], the volume score [34], and the mass score [35]. Accurate quantification using any of these methods require identification of calcified voxels from the background. Conventionally the quantification is done by using non-contrast-enhanced computed tomography (CT) scan by designating any voxel with intensity greater than 130 Hounsfield unit(HU) as a calcified voxel. The Agatston score assigns different scores to disjoint calcified area known as lesions based on the peak intensity in each area and combining all the scores assigned to these calcified lesions. The volume and mass score calculates the total volume and the mass of the calcium respectively from the total number of calcified voxels. The methods considered in this review perform quantification by using one or all the three methods.

The non-contrast-enhanced CT is not sufficient to rule out the presence of coronary artery disease (CAD) in case of patients with disease symptoms. Therefore, the computed tomography angiography (CTA) is done in symptomatic patients to study the morphology and to assess a suspected CAD. CTA is done by injecting an x-ray opaque dye called contrast agent which makes the arteries clearly visible in the scan by enhancing the intensity of blood flowing in interior space of the artery known as the lumen. Since calcification occurs in the artery wall, the high intensity of lumen in CTA may simulate calcification in the artery wall [21]. This results in unreliable calcium quantification because of the possibility of inclusion of contrast voxel as a calcium voxel or the exclusion of the calcium as contrast material.

Accurate calcium quantification is possible in CTA if the artery wall can be segmented from the lumen. However, it is difficult to separate the wall from the lumen because the cross section of a coronary artery occupies only a few voxels. In this chapter we review recent studies that attempted to quantify calcium from the contrast-enhanced CTA by using different methods.

2.1 Previous attempts of calcium quantification from CTA

Many studies have been done with the aim of replacing the non-contrast-enhanced coronary artery calcium scan (CAC) with the calcium quantification derived from the contrast-enhanced computed tomography angiography (CTA). These may be roughly divided into clinical studies and automatic methods. The clinical studies are done in a population of patients by using commercially available CT image analysis software for calcium quantification. Most of the clinical studies involve a significant amount of manual intervention, and the results are characterized by inter and intra-observer variability. Hence, the methods presented may not be applied practically to obtain an accurate and repeatable calcium quantification in CTA. One of the factors responsible for the drawbacks of these methods is the use of a single threshold and no attempts to address the variability of thresholds for different patients or multiple scans of a single patient. Another category of work focus on automatic extraction of arteries and their centerline but suffers the drawback in not addressing the variability of cutoff threshold along the length of artery, and separation of low-density calcium from the contrast voxels in the overlapped intensity range. Other works consider calcium and contrast detection in larger vessels such as carotid artery or aorta and not directly applicable to smaller vessels such as coronary arteries.

2.1.1 Clinical studies with fixed cutoff thresholds

Hong et al., used the fixed threshold of 350 HU to quantify calcium from 1.25 mm slice thickness contrast-enhanced CTA in 50 patients [22]. The Agatston score and calcium mass quantification done by a radiologist (Cheng Hong, Department of Clinical Radiol-

ogy, University of Munich, Munich, Germany) by using a commercial software (InSight, Neo-Imagery Technologies) were compared to the corresponding scores obtained from non-contrast-enhanced CT scan by using 130 HU threshold. Linear regression showed high correlation of both the Agatston score and the calcium mass (0.942, $p < 0.001$ and 0.977, $p < 0.001$ respectively) in contrast-enhanced and non-contrast enhanced scan. There was no significant difference in calcium mass score and it had lower variability in repeated quantifications than the Agatston score which was also significantly different in contrast-enhanced and non-contrast-enhanced CT scans. The study also compared the accuracy of calcium quantification in different slice thickness reconstructions of 3.0 mm, 1.25 mm, and 0.6 mm by using a cardiac CT phantom. A phantom consists of artificial organs and tissues and is used for calibration or validation study. The lower slice thickness reconstructions revealed more calcified cylinders in the phantom than the higher slice thickness reconstructions. The Agatston score in CTA was underestimated while the mass score was overestimated.

Mühlenbruch et al. performed a study similar to that of Hong et al. [22] by quantifying Agatston score and the calcium mass in phantoms and 36 patients by using a threshold of 350 HU [21]. The study found overestimation of the scores in patients and underestimation in the phantom and 57% of all patients were assigned to different risk groups by the calcium quantified from the CTA. Although, the study found the use of CTA unreliable in assessing the total amount of calcium in coronary arteries, more recent studies have shown a very high correlation, low limits of agreement, high agreement to risk stratification by non-contrast-enhanced quantification, etc., thus indicating the feasibility of reliable and accurate calcium quantification from CTA.

Glodny et al. used an arbitrary threshold of 600 HU to quantify calcium using volume score in contrast-enhanced CTA images in 113 patients and compared the volume with Agatston score and calcium volume score using a threshold of 130 HU in non-contrast-enhanced CT scan [23]. A CT workstation (AW 4.4, General Electric) was used to calculate Agatston score and the volume score from non-contrast enhanced CT. The same workstation was used to manually extract coronary arteries required for quantification from CTA. The

choice of 600 HU was to eliminate the entire heart and artery lumen in one threshold step and was based on the observation that smaller thresholds such as 350 HU used in previous studies [22, 21] were unable to separate the lumen. The volume score obtained in CTA had a strong correlation of more than 0.92 for two observers with both the Agatston score and the volume score in non-contrast-enhanced CT. Inter and intra observer variation were small. However, the high threshold led to exclusion of some low density calcium resulting in underestimation of total calcium compared to both the Agatston score and the volume score in non-contrast-enhanced CT.

Van der Bijl et al. obtained calcium scores in CTA in 100 patients and compared them to the corresponding non-contrast-enhanced calcium scores computed in 50 CT with a 0 Agatston score and with an Agatston score of 1 or more in another 50 patients [36]. They assigned two observers (with 2 - 4 years of experience in cardiac CT imaging) to manually identify and draw contours around calcified spots in CTA and used the conventional threshold of 130 HU to quantify the calcium. A software (Vitrea FX 1.0, Vital Images) was used to calculate calcium score automatically from the plaques in both the scans. Although good correlation and high sensitivity, specificity, positive predictive value, and negative predictive value of detecting coronary calcium with CTA was observed, high Agatston scores were underestimated by the CTA. Calcium spots were identified visually which might have excluded some of the calcified voxels resulting in the underestimation of the Agatston score.

A recent study by Bischoff et al. concluded the quantification of coronary artery calcium from contrast-enhanced feasible by showing a high correlation coefficient ($r = 0.954$, $p < 0.001$) of calcium quantification in contrast-enhanced CTA in 100 patients [37]. 98% of patients without coronary artery calcium were correctly identified by the calcium quantification in contrast-enhanced CTA. More than 95% of the patients were correctly grouped into same risk category by using their method.

More recently, Otton et al. quantified calcium from contrast-enhanced CTA by using a threshold of 320 HU [17]. For the quantification, first a segmentation of lumen from artery wall was done by using a commercial software tool (SurePlaque, Vitrea FX 3.1, Toshiba

Medical Systems) followed by manual adjustments of incorrect segmentations. The threshold of 320 HU was then applied to the segmented artery wall to calculate calcium volume. The calcium volume derived from the contrast enhanced CTA was converted to Agatston score by multiplying with an empirical conversion factor. The conversion factor was derived by using regression analysis between the calcium volume derived from the contrast-enhanced CTA and the Agatston score derived from non-contrast-enhanced scan in 90 patients who had both contrast-enhanced and non-contrast enhanced scans done. A linear relation was found from the regression analysis with a conversion factor of 3.13. The accuracy of calcium score estimation was validated in contrast-enhanced and non-contrast enhanced CT scan pairs from a set of 120 patients different from the original 90 patients used for determining the conversion factor. Correlation coefficient of 0.99 was observed between the actual Agatston score calculated from non-contrast-enhanced CT scan and the contrast-enhanced CTA derived score by applying the empirical conversion factor.

The accuracy of the method is highly dependent on the cutoff threshold of 320 HU and the accuracy of artery wall segmentation. The excellent correlation of 0.99 might have been due to the manual correction of segmentation. The requirement of manual segmentation for each CT scan reduces the repeatability and increases the time taken. The single conversion factor of 3.13 may not be optimal as the Agatston score assigns different weights to voxels of different intensity range [38].

Since the contrast filled lumen has high intensity, many studies increased the threshold of detection of calcium from the conventional threshold of 130 HU in non-contrast-enhanced CT to 320 HU [17], 350 HU [21, 22] or 600 HU [23] in order to separate the lumen from calcium. However, these thresholds resulted either in underestimation [21, 23, 17] or overestimation [22] of calcium. A single threshold of 350 HU overestimated [22] and underestimated [21] the calcium quantification thus indicating the unreliability of a single threshold across different studies.

2.1.2 Adaptive cutoff thresholds for different arteries

An automatic calcium detection and quantification method in CTA has been described by Teßmann et al. [18, 19]. The algorithm proceeds with extraction of artery centerlines by using method described by in Gülsän and Tek [39] and full coronary artery tree from the 3D CTA data. A histogram based on intensity values along the centerlines of the segmented artery is generated and the last maxima of the histogram is used as the mean intensity of the lumen. The last maxima, i.e., the maxima corresponding to highest HU value was selected as the mean of the contrast material based on the assumption that HU value of calcium lie above the HU corresponding to the last maxima. The optimal cutoff threshold was chosen as the HU value at which the derivative of the histogram function exceeded an empirically derived threshold. The threshold was used to identify calcium from the segmented trees, and lesions were identified by connected component analysis. Calcium quantification was done according to three different measures : Agatston's score, calcium volume and calcium mass, each of which were found to have high correlation coefficients with the corresponding scores assigned manually on 46 CTA images. The study calculated individual cutoff HU threshold for different CTA data which is important since the contrast enhancement and hence its peak HU intensity level depends upon factors such as patient physiology, contrast injection rate, contrast concentration, time elapsed since contrast administration, image noise etc. [24]. Although, a fully automated approach, including HU estimation, and lesion segmentation was used to quantify calcium, the accuracy of this method largely depends upon the accuracy of vessel centerline extraction and segmentation. The accuracy of validation may not be reliable since the ground truth used for the validation is based on manual scores assigned by a single radiologist chosen by Teßmann et al. [18] and hence might suffer from inter-observer variability.

2.1.3 Quantification using both CTA and CAC

Saur et al. detected calcified plaque using both contrast-enhanced CTA and non-contrast-enhanced CT scan by using rigid registration of plaques identified from the scan

pair [20]. Plaques were identified in the CTA by first extracting vessel centerline using an algorithm described in [40] followed by lumen segmentation in the cross sections perpendicular to the detected centerline. The lumen segmentation was done by applying graph cut algorithm [41] which models voxels as graph nodes and finds an optimal partition to divide the set of nodes into two different sets. The segmentation was done with a circular shape prior [42] which restricts the resulting cross section to be circular in shape. Marching cubes algorithm [43] was then applied to extract calcified plaque. The marching cubes algorithm creates a three dimensional surface by interpolating voxels with similar values known as an iso-value. Iso-values of $\mu + 5\sigma$ was used, where μ is mean and σ is standard deviation of a $7 \times 7 \times 7$ voxels neighborhood selected from the aorta. In non-contrast CT plaque were identified by applying marching cube algorithm with an iso-surface value of 130 HU and removing connected components of large volumes corresponding to bones. Calcified plaques extracted from both are then matched by using rigid registration which finds out optimal rotation and translation parameters to match the source and target plaques. The final set of plaques consisted of all matched pair of plaques from the contrast-enhanced and non-contrast-enhanced CT and any plaques of higher intensity visible in CTA and not visible in non-contrast-enhanced scan. 85.5% of calcified plaques were correctly identified by using plaques identified manually by an assigned radiologist as ground truth data. The algorithm does not completely exploit the contrast-enhanced CTA and requires the patients to go through both the scans. Since no quantification of calcium was done from the plaques, the accuracy of calcium volume that can be detected is unknown. Furthermore, the validation based on quantification done by single radiologist may not be accurate as it may suffer from inter and intra-observer variability as was the case in the quantification by Teβmann et al. [18].

2.1.4 Artery wall segmentation for different plaque identification

Another approach attempts to segment inner and outer artery wall in order to isolate the calcium within the wall. Distinct threshold ranges are then used to classify different plaque

components from within the artery wall. Vukadinovic et al. describes a method to segment the outer wall [44] and use it for quantifying different plaque components from carotid artery in contrast-enhanced CTA dataset [45]. They first use the level set [46] approach to segment the carotid artery lumen and the calcium were extracted from around the lumen by using 320 HU cutoff threshold. Then a GentleBoost [47] classification was used to classify the calcium extracted initially as true calcium or not. Different features such as distance to the lumen, volume of the plaque, different intensity profiles radially and tangentially with respect to the lumen from images smoothed with Gaussian derivative filters on multiple scales etc were extracted from the training images with the contours of lumen and different plaque tissues manually drawn by an expert assigned by Vukadinovic et al. [45]. Similar classification was used to classify each voxel as lying inside or outside the artery. The result of the two classification steps along with an ellipse fit to the vessel delineated the outer wall. The area in between the outer wall and inner wall formed by the lumen edge was the actual artery wall where different plaque components were quantified according to fixed threshold range such as the voxels in the range -20 HU to 60 HU were identified as lipid, 60HU to 130HU were fibrous tissue. The conventional threshold of 130 HU was used to identify calcium from the artery wall. Although the approach reported high correlation with plaque components identified by radiologist, the actual difference in calcium quantity has not been reported. The method, although extracts calcium and other plaque components with least manual intervention, such as during level set segmentation, due to the fixed threshold approach suffers same disadvantages as other clinical methods.

Carotid wall segmentation has been described in various works such as by Bruijne et al. [48] by using active shape model [49], Olabarriaga et al. [50] by using a deformable-model [51] for lumen segmentation and a $k-$ nearest neighbor ($k-NN$) classifier for outer wall segmentation. Different plaque components can be identified once the wall has been delineated based on different intensity range. Since there is an overlap in intensity profiles of calcium and the contrast-filled lumen, the segmentation of lumen might include some of low density calcium objects. These methods, in general, do not make attempt to identify

any calcium falsely classified as lumen because of overlapped intensity profile of low density calcium and lumen and hence may not accurately quantify calcium.

Although the success of most of the methods are measured in terms of correlation with different ground truth, the correlation-coefficient only measures the strength and not the agreement [52]. In the measurement of CAC it is important to achieve lower difference range, in order to not to reassign the patients into new risk stratification level.

2.1.5 Detection of the presence of contrast in a CT scan

Criminisi et al. constructed a probability model to detect the presence of the contrast material in CT scans by using the intensity histogram as the feature to describe a local window containing an organ of interest such as heart, kidney etc [53]. The binary decision of whether a particular organ in a CT-scan has the intravenous contrast is done by first localizing a window [53] to an organ of interest and then by maximizing the posterior probability $p(c|\mathbf{S}, \mathbf{O})$, where c is either contrast-enhanced class (C), or non-contrast-enhanced class (N), $\mathbf{S} = \{s_1, s_2, ..., s_N\}$, where s_i represents the intensity histogram in HU for N different organs of interest, and $\mathbf{O} = \{o_1, o_2, ..., o_N\}$, where $o_i = 1$ is assigned by an observer if the organ is clearly visible otherwise it is assigned 0. The probability $p(s_i|o_i = 1, c)$ is modeled as a Gaussian for each organ and the parameters are learned from a trained set of images. Then $p(c|\mathbf{S}, \mathbf{O})$ is found as,

$$p(c|\mathbf{S}, \mathbf{O}) = \frac{1}{Z} p(c) \prod_{i}^{N} p(s_i|o_i, c) p(o_i). \tag{2.1}$$

The factor Z is same for both the classes C and N and is ignored for comparing the posterior probabilities for the two classes. Whether a certain organ received the contrast material is recorded manually in the metadata information of the CT volume file [53]. In this study, the contrast detection is done in order to correct any error introduced during manual entry of contrast in metadata. Although the method is useful in classifying the presence or absence of contrast in an organ, it is not directly applicable in distinguishing a calcium voxel from the contrast voxels as their intensity range overlap and the resolution of artery cross

section is not large enough for multi-scale feature detection.

2.1.6 Multiresolution feature based classification of calcium

Papadakis et al. used 3-D isotropic multiresolution representation [54] to classify texture corresponding to different tissue components such as lumen, calcium deposits, lipids, fibrous tissues, muscle cells, etc. from CT data [55]. Voxels corresponding to different tissue types selected manually were used to construct a training set. The training set was then used to classify unknown tissues throughout the CT volume data by matching statistics.

Bruijne combines a $k-NN$ (nearest neighbor) pixel classifier with a spatially varying calcium prior to detect calcium in X-ray radiography images of aorta in abdomen [56]. The pixel classifier assigns a pixel into one of the two classes, calcium or background by using $k-NN$ algorithm. The feature vectors required for training and classification are obtained from the outputs of applying the image to a set of Gaussian derivative filters at multiple scales. Classification obtained from the pixel classifier are combined to a spatially varying calcium prior to localize the detection of calcium in the aorta. The calcium prior probability model is constructed, first by averaging calcium distributions across cross sections and along the length of a number of training set of aortas. Bruijne then used a point distribution model (PDM) [49] to estimate the shape and pose of aorta given a spine shape since the position of two are correlated. A PDM represents shape by using Principal Component Analysis (PCA) of a set of training shapes represented in a $2n$ dimensional $(2n-D)$ space, where n is the number of points (in 2-D (x, y) pair) used to represent each shape. A new shape variation can be derived from linear combination of the mean along with the principle axes obtained from the PCA of the shapes in the $2n-D$ space. An average of different random variations in aorta shape was combined with the longitudinal and cross-sectional calcium profiles to construct the calcium prior probability model.

2.2 Summary

Different studies have been done to quantify calcium from the contrast-enhanced computed tomography angiography (CTA). Several works have increased the cutoff threshold to account for the increase in the lumen intensity due to contrast administration [17, 18, 19, 20, 21, 22, 23]. Since the cutoff threshold is proportional to the peak contrast intensity, a single cutoff threshold does not provide an accurate quantification for different CT scans and for a selected artery. The work by Teßman et al. [18, 19] remove some of the inaccuracies by considering an adaptive threshold for each artery. However these works do not address the contrast intensity variation along the length of the artery as will be shown in chapter 5. Furthermore, none of the reviewed methods consider the quantification of low-density calcium by separating them from the contrast voxels in the range of intensity overlap. In chapter 5 we develop algorithms to find the probability of low-density calcium voxels in the overlapped intensity range, and an adaptive cutoff threshold which varies along the length of an artery to separate the high-density calcium lengthwise.

Other studies such as by Saur et al. [20] requires both the contrast-enhanced and non-contrast-enhanced CT scans for the quantification. In larger arteries such as the carotid artery and the arota, the quantification is facilitated by first segmenting the artery wall and then applying a fixed range of thresholds to classify different plaques [45, 48, 50]. The wall segmentation is not applicable to relatively smaller coronary arteries. Classification approaches for detecting contrast or calcified voxels in vessels and organs larger than coronary arteries by multiresolution features detection [56, 53] are not directly applicable in distinguishing a calcium voxel from the contrast voxels as their intensity range overlap and the resolution of the coronary artery cross section is not large enough for multiresolution feature detection.

CHAPTER 3

CALCIUM QUANTIFICATION IN NON-CONTRAST-ENHANCED COMPUTED TOMOGRAPHY: PRELIMINARY WORK

In this chapter we perform the preliminary work of quantifying calcium from non-contrast-enhanced computed tomography (CT) scan. We compare the CT volume quantified from 0.5 mm slice thickness reconstruction with the volume from 3.0 mm slice thickness reconstruction. We study the effect of different cutoff thresholds in the accuracy of calcium quantification and suggest an optimal cutoff thresholds for quantification in both the 3.0 mm and 0.5 mm slice thickness volumes. The results in this work can be clinically useful in deciding an appropriate threshold for calcium quantification. We have developed software tools and methods for manually extracting arteries from the CT volume, registering the extracted arteries with the intravascular ultrasound with virtual histology (IVUS-VH) images and validating the accuracy of calcium quantification. The manual vessel extraction and registration is necessary due to a very low or no contrast between the artery and the surrounding tissue in a non-contrast-enhanced CT scan. The manual artery extraction and the manual registration methods developed in this chapter are extended to automatic methods to quantify calcium from the contrast-enhanced computed tomography angiography (CTA) in chapters 4, and 5.

3.1 Introduction

Coronary Artery Calcium (CAC) quantification is done by using non-contrast-enhanced Computed Tomography (CT) images. State-of-the-art 320-detector row CT scanners have 320 x-ray detector elements each of which can acquire an image of a section 0.5 mm thick, thus covering 16 cm of an anatomy in one rotation. The images acquired from 320-detector can be reconstructed with 0.5 mm slice thickness or a larger slice thickness of 3.0 mm is

also available. Conventionally, CAC quantification is done by using 3.0 mm slice thickness reconstruction where any voxel greater than or equal to 130 Hounsfield Unit (HU) is identified as a calcium. 0.5 mm slice thickness reconstruction achieves higher spatial resolution than the 3.0 mm slice thickness reconstruction. It has isotropic voxel size, i.e., the size of voxel is almost equal in all three dimensions and hence it is easy to reconstruct coronary structures in arbitrary plane. However, the accuracy of calcium quantification using 0.5 mm isotropic resolution and the effect of different HU cutoff thresholds on the accuracy of quantification have not been studied.

In this chapter we study the accuracy of calcium quantification on 0.5 mm isotropic CT scan. We also study the effect of different attenuation cutoff threshold on the validity of calcium quantification and compare the 0.5 mm and 3.0 mm CAC quantification by validating against spatially registered IVUS-VH on a very detailed slice-by-slice basis. The calcium volume obtained from a population of 23 patients using different HU thresholds were analyzed by correlation as well as sensitivity, specificity, positive predictive value (PPV), and negative predictive value (NPV) to find an optimal threshold. For the 3.0 mm CAC quantification, we found the 120 HU and for the 0.5 mm CAC 226 HU provide optimal quantification. The calcium quantification done by using 0.5 mm slice thickness reconstruction in the optimal range yielded higher sensitivity, specificity, NPV and PPV, and lower mean difference range than the conventional 3.0 mm CAC in its optimal range.

3.2 Methods

A total of 23 patients were studied, 14 of whom had coronary artery disease and remaining 9 had normal arteries. Non-contrast-enhanced CAC quantification, and contrast-enhanced-CTA was done in both diseased and normal patients. The 14 diseased patients also underwent IVUS-VH in the selected artery. The investigation was approved by the institutional review board of Piedmont Hospital. The demographic information of the patients is listed in Table 3.1.

Table 3.1 Patient Demographics

	CAD	Normal
Patient Number	14	9
Age	61.5 ± 7.9	50.4 ± 8.8
Sex	10M, 4F	5M, 4F

CAC images were taken on a multi-detector CT with conventional imaging protocol with no increase in radiation dose, in a prospective volumetric mode with a tube voltage of 120 kV, tube current of 110 - 550 mA, 0.5 mm detector width and reconstructed with 0.5 mm and 3.0 mm slice thickness. In order to compare the CT images with IVUS-VH, we need to extract the desired coronary artery from the CT images. Since it is difficult to extract a coronary artery automatically from the non-contrast-enhanced CT scans, we have developed a software (fig. 3.1) to manually extract the vessel centerline from the CT images, and transform the vessel to a straight-vessel view. We also developed a software tool to align and register the CAC images with the IVUS-VH, so that the calcium quantification in CAC and IVUS-VH can be compared on a very detailed slice-by-slice basis in each of the cross-sectional slice that is perpendicular to the vessel centerline.

3.2.1 Centerline Extraction in CAC Images

Our software allowed the users to browse through the 3D image set and manually annotate the center-points of the vessel of interest. Figure 3.1 shows the snapshot of the software. The manual annotation gave a set of 3D coordinates representing the actual path of the vessel. The set of 3D points were then interpolated and made smooth by using the snake deformable model [57].

The snake is a smooth curve which is pulled toward image features such as edges, lines, etc. and hence typically used for segmenting desired object in an image by aligning it to the object contour. The snake is initialized as a set of points and the pulling of these points toward the image features is done iteratively by minimizing the external forces exerted by

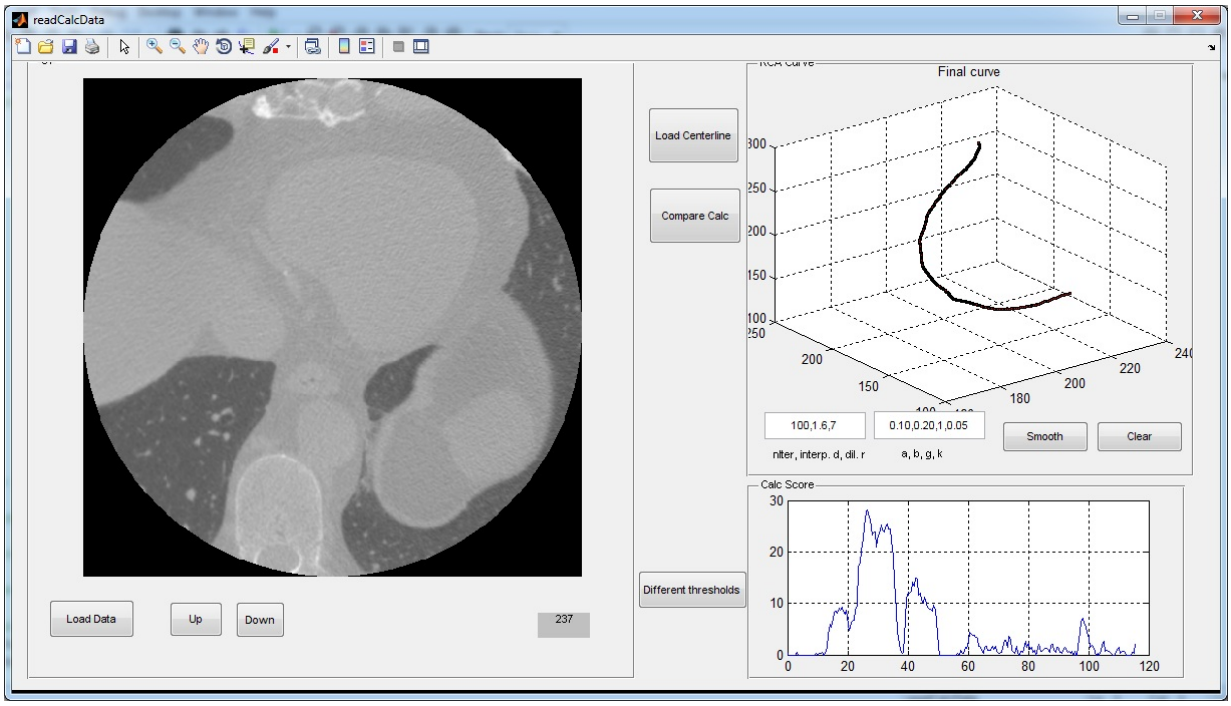

Figure 3.1 Software tool to browse through the CT slices and annotate the desired artery to extract the centerline.

the image features at each step. During each iteration, a set of internal forces keeps the snake smooth. The snake can be represented as $u(s) = (x(s), y(s))$, where s is the normalized arc length along the curve $u(s)$, $x(s)$ and $y(s)$ are the x and y coordinates of the points in $u(s)$. The energy associated with the snake is given by,

$$E(u(s)) = \int_0^1 E_{int}(u(s)) + E_{ext}(u(s))\,\mathrm{d}s. \tag{3.1}$$

To converge at its final shape and position, the snake minimizes its total energy $E(u(s))$ which is composed of the internal energy $E_{int}(u(s))$ and the external energy $E_{ext}(u(s))$. The internal energy can be expressed as,

$$E_{int}(u(s)) = \int_0^1 \alpha(s)|u'(s)|^2 + \beta(s)|u''(s)|^2\mathrm{d}s, \tag{3.2}$$

where u' and u'' are the first-order and second-order derivatives of the snake function $u(s)$; $\alpha(s)$, and $\beta(s)$ are the corresponding weighting functions. The first-order term is known as

"membrane" which avoids tear or breaking of the snake, and the second-order term is known as "thin-plate"which avoids sharp corners in the curve. The external energy or the image potential can be expressed as the sum of energy due to different features such as edge, line and terminals. In many practical applications external energy due to edge may be sufficient, which can be expressed as the gradient of the image as follows,

$$E_{edge} = -| \bigtriangledown \Phi(x, y)|^2, \tag{3.3}$$

where $\Phi(x, y)$ is the image. The total energy functional $E(u(s))$ can be minimized by solving the Euler-Lagrange equation and the snake at iteration t can be obtained from its previous iteration as follows [57].

$$u(s_t) = (A + \gamma I)^{-1}(u(s_{t-1}) + \mathbf{f}_{ext}(u(s_{t-1}))) \tag{3.4}$$

where I is the identity matrix and A is a pentadiagonal matrix formed by the weighting parameters α and β as follows,

$$A = \begin{pmatrix} c_1 & d_1 & e_1 & 0 & 0 & 0 & \cdots & 0 & 0 & 0 & 0 & a_1 & b_1 \\ b_1 & c_1 & d_1 & e_1 & 0 & 0 & \cdots & 0 & 0 & 0 & 0 & 0 & a_1 \\ a_1 & b_1 & c_1 & d_1 & e_1 & 0 & \cdots & 0 & 0 & 0 & 0 & 0 & 0 \\ \vdots & \vdots & \vdots & \vdots & \vdots & \vdots & \vdots & \vdots & \vdots & \vdots & \vdots & \vdots & \vdots \\ 0 & 0 & 0 & 0 & 0 & 0 & \cdots & 0 & a_{N-2} & b_{N-2} & c_{N-2} & d_{N-2} & e_{N-2} \\ e_{N-1} & 0 & 0 & 0 & 0 & 0 & \cdots & 0 & 0 & a_{N-1} & b_{N-1} & c_{N-1} & d_{N-1} \\ d_N & e_N & 0 & 0 & 0 & 0 & \cdots & 0 & 0 & 0 & a_N & b_N & c_N \end{pmatrix},$$

where

$a_i = \beta_{i-1}$,

$b_i = -2\beta_i - 2\beta_{i-1} - \alpha_i$,

$c_i = \beta_{i+1} + 4\beta_i + \beta_{i-1} + \alpha_{i+1} + \alpha_i$,

$d_i = -2\beta_{i+1} - 2\beta_i - \alpha_{i+1}$,

$e_i = \beta_{i+1}$.

In order to smooth the manually annotated set of points in 3D, we initialized the snake as a cubic interpolation of these points. The manually annotated points were used as the salient features in 3D space which pulled the curve toward them in each iteration bringing the initial snake close to the points and meanwhile smoothing it to approximate a vessel centerline. Equation 3.4 can be decoupled with respect to x, y and z spatial parameters, and the new positions for the discrete points $(x_i(u), y_i(u), z_i(u)), i = 1, ..., N$ along the length of the snake can be obtained as,

$$x_t = (A + \gamma I)^{-1}(x_{t-1} + f_x), \tag{3.5}$$

$$y_t = (A + \gamma I)^{-1}(y_{t-1} + f_y), \tag{3.6}$$

$$z_t = (A + \gamma I)^{-1}(z_{t-1} + f_z), \tag{3.7}$$

The external force was obtained as a force proportional to the distance vector from the snake to the manually annotated points with the force components given by,

$$f_x = \kappa(x_{manual} - x_{snake}), \tag{3.8}$$

$$f_y = \kappa(y_{manual} - y_{snake}), \tag{3.9}$$

$$f_z = \kappa(z_{manual} - z_{snake}), \tag{3.10}$$

where κ scales the force magnitude. In our experiments we set the value $\alpha = 0.10, \beta = 0.20$, and $\kappa = 0.05$ which produced smooth approximations of the centerline in a low number of iterations.

Figure 3.2 shows an example of a snake interpolation at different iterations. The snake was initialized as a line joining two extreme manually annotated points. At each iteration,

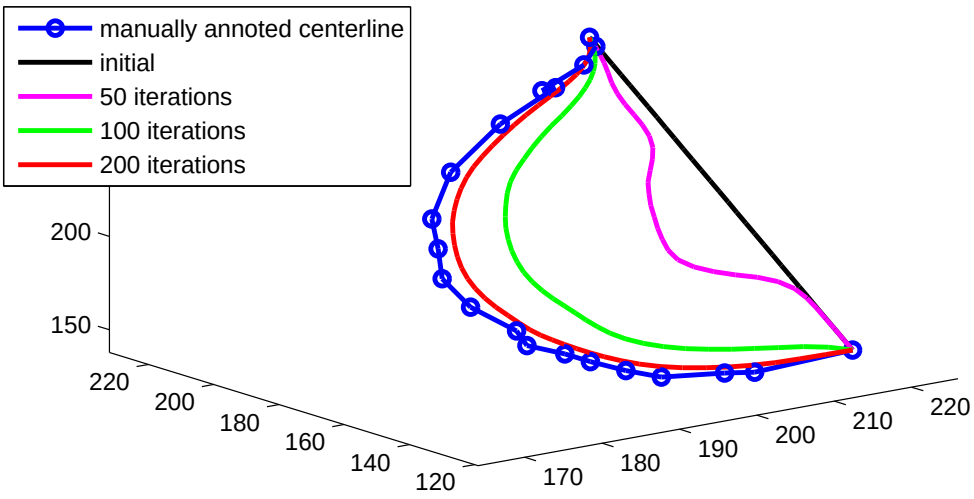

Figure 3.2 Snake positions in different iterations.

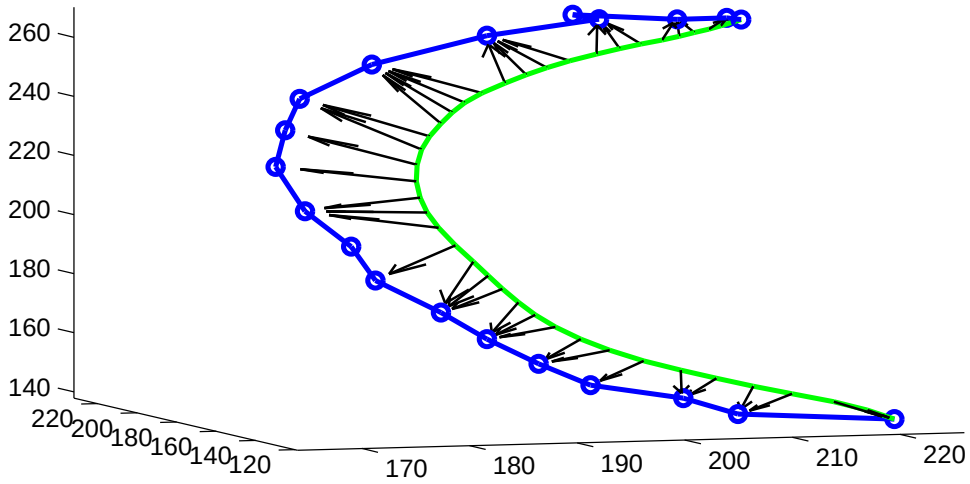

Figure 3.3 External force acting on the snake. The external force shown as black arrows pull the snake (red curve) toward the annotated points shown as circles.

the snake is attracted toward the annotated points and the magnitude of the external force gets smaller as the snake approaches the annotated points. The force pulling the snake at an iteration step is shown in figure 3.3. The arrows show the direction in which each point in the snake is attracted toward one of the manually clicked points.

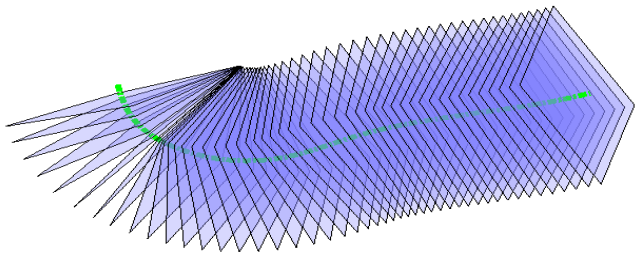

Figure 3.4 2D cross-sectional slices sampled along the artery centerline in the CT image.

In order to compare the CAC volume with the set of 2D IVUS-VH images, appropriate images from the 3D CAC data had to be extracted and lined up as in IVUS-VH image set. As shown in Fig. 3.4, we extracted the images perpendicular to the centerline and equally spaced from each other in order to emulate the images taken by IVUS catheter inside the artery. In order to achieve more reliable registration and to facilitate comparison of 0.5 mm and 3.0 mm reconstructions, we set the slice-to-slice spacing to be 3.0 mm, which resulted in a total of 432 slices in both the modalities.

3.2.2 IVUS Image Acquisition and Analysis

IVUS-VH images were acquired in a IVUS-VH console with a catheter (Eagle Eye, Volcano Corporation). A medication called Nitroglycerin was injected to enlarge the blood vessels so as to facilitate the movement of the catheter. The catheter was advanced beyond the target lesion and automated pullback with IVUS image acquisition was performed at a rate of 0.5 mm/sec. A medical doctor was asked to manually delineate the lumen contour and the outer boundary of the arterial wall on the image. Then, the IVUS-VH console automatically classified the plaque area in between the two contours into 4 plaque compositions, by analyzing the reflected ultrasound signals using a principal component analysis

(PCA)-based algorithm [7]. Fig. 2 shows the longitudinal view of a coronary artery created by stacking 2D IVUS-VH images. White, red, light green, and dark green represent dense calcium, necrotic core, fibrofatty, and fibrous tissue, respectively.

3.2.3 Calcium Quantification in CAC Images

The smoothed vessel centerline in CAC images was densely re-sampled and dilated in 3D using the morphological dilation operation [58] with a spherical structural element of radius of 7 voxels. The choice of 7 voxels was determined experimentally which was enough to cover all the possible calcified voxels in the selected vessels without including any non-arterial calcification. All the voxels in the dilated vessel were then perpendicularly projected into the vessel centerline to derive their distance values to the vessel centerline. Initially, we implemented the conventional calcium attenuation cutoff threshold of 130 HU to derive the calcified volume in the CAC image, i.e., if the Hounsfield unit (HU) of a voxel was equal to or greater than 130 HU, it was reported as a unit of calcium.

A voxel in the dilated CAC vessel was assigned to the 2D slice closest to the voxel's projection in the centerline. The calcium volume in each cross-sectional slice along the centerline in the CAC images was calculated by multiplying the volume of a voxel with the total number of voxels whose attenuation values are equal to or greater than 130 HU, and belongs to that slice. Figure 3.6(a), and 3.6(b) show the calcium volume quantified along a vessel centerline in the 0.5 mm CT and 3.0 mm CT image set respectively. The initial threshold of 130 HU was used only for the registration of CT CAC with IVUS-VH.

3.2.4 Non-contrast-enhanced CT and IVUS-VH Registration

Previous studies in Computed Tomography Angiography (CTA) and IVUS registration were done by using contrast agent which is generally iodine based liquid injected intravenously to enhance the contrast of the vessel in the CT scan. Leber et al. for example, registered CT vessel with IVUS by visual comparison by looking at landmarks such as side branches in order to study the accuracy of 64-slice CT in classifying and quantifying plaque

volume [59]. Marquering et al. matched IVUS and CTA data manually along the longitudinal views, and semi-automatically registering segmented vessel contours in 2D cross-sectional views [60]. More recently, Qian et al. registered CTA images obtained from 64-slice CT with IVUS-VH by simulating the CTA image from IVUS-VH, and by using mutual information based registration algorithm [61]. All of these works used contrast enhanced CTA images. Different from the previous works, we use the 320-detector-row CT without any contrast agent. Since it is difficult to segment the non-contrast-enhanced CT automatically, we chose to manually register it by using the software tools we developed.

Vessel straight view of the IVUS-VH was reconstructed by stacking the 2D IVUS-VH slices together and forming a longitudinal view. The registration between the straight views of IVUS-VH and CAC was done by manually selecting a set of landmark points in the straight views of both IVUS-VH and CAC by looking at different salient features, such as vessel branches and calcium deposits, at different regions along the vessel. Fig. 3.5(a) and (b) show the vessel straight views of aligned CT and IVUS-VH respectively. The green dotted lines were the manually selected landmarks.

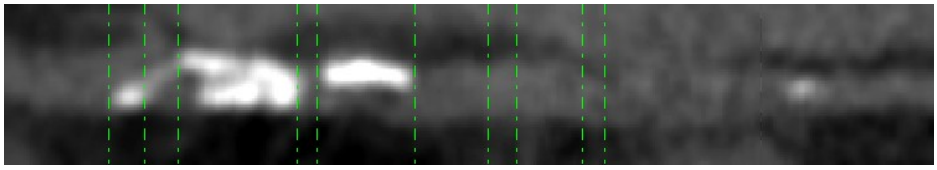

(a) CT

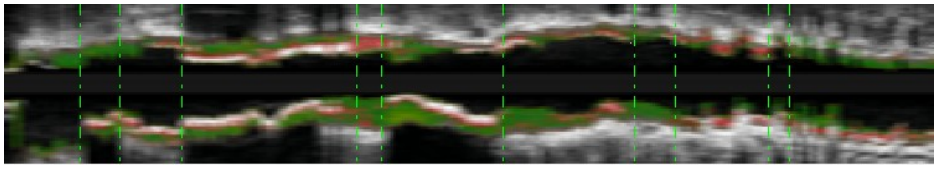

(b) IVUS-VH

Figure 3.5 Manual alignment of the (a) CT and (b) IVUS-VH images by visually comparing the vessel straight views. Salient image features, such as vessel branches and calcium deposits, were utilized in the manual alignment. Calcium deposits can be seen as white patches in CT and as white linings within the color-encoded vessel wall in IVUS-VH.

Visual alignment of the straight views gave a rough registration between IVUS-VH

and CAC. However, it was not accurate enough for a slice-by-slice comparison. In order to fine-tune the registration, we introduced a calcium volume curve alignment step by manually panning and scaling the curves sideways in the calcium curves obtained from both the modalities. Fig. 3.6 shows the registration of the calcium curves obtained from CAC and IVUS-VH. The calcium volume obtained from IVUS-VH (shown in red) can be panned and scaled sideways over the calcium volume curve obtained from the CAC to obtain an accurate registration.

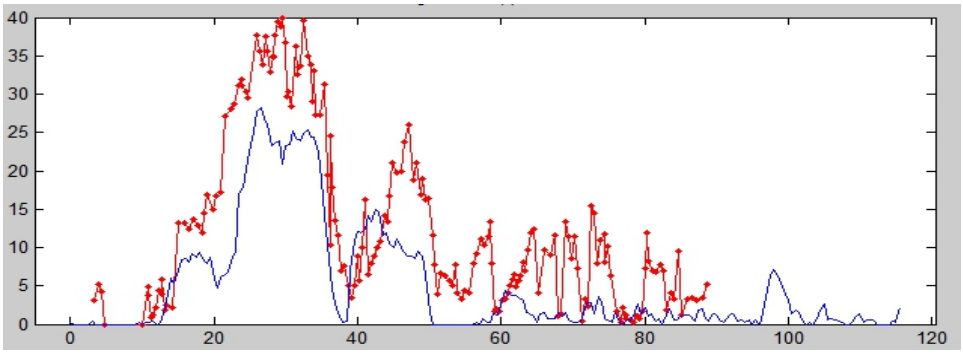

Figure 3.6 Manual registration by panning calcium curve obtained from the CT over the IVUS-VH calcium curve. The blue curve is calcium obtained from CT which is aligned to the red curve obtained from IVUS-VH by manually panning and stretching horizontally.

The calcium volume along the centerline of the IVUS-VH scan was then interpolated and calculated using the same sampling intervals as in the CAC calcium curve. Fig. 3.7 shows an example of the aligned calcium curves obtained from the (a) CAC 0.5 mm, (b) CAC 3.0 mm, and c) IVUS-VH.

3.2.5 Calcium Quantification in CAC images using different cut-off threshold

For the 3.0 mm conventional CAC and 0.5 mm isotropic CAC scoring it is unknown if the 130 HU threshold is optimal for calcium quantification. Therefore, we quantified the CAC volumes by using different cutoff thresholds starting from 50 HU to 400 HU and obtained a group of calcium volume quantification values corresponding to each threshold. The group of calcium volume values were then compared to IVUS-VH calcium values on a slice-by-slice basis by using the registration coordinates obtained from the previous mentioned alignment

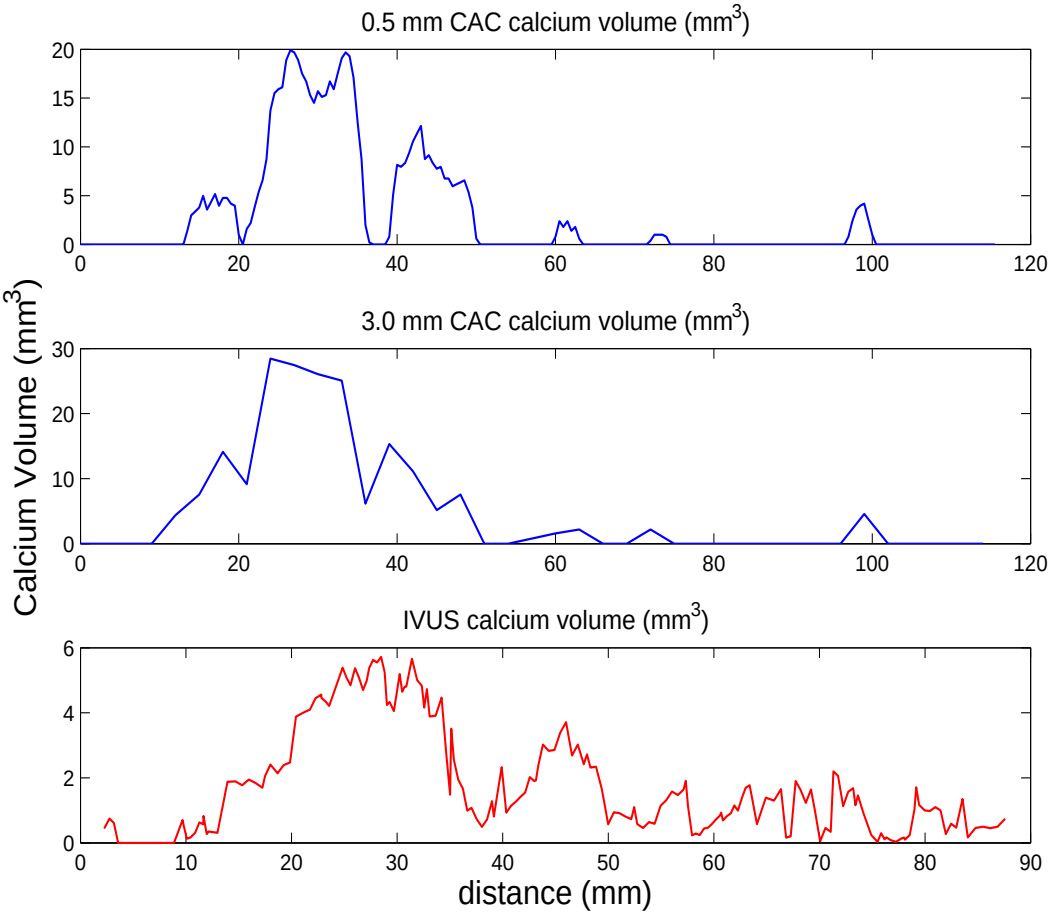

Figure 3.7 Calcium volume curves derived from (a) 0.5 mm CT, (b) 3.0 mm CT, and the (c) IVUS-VH.

of IVUS-VH with the CAC curves. The CAC volumes obtained form 3.0 mm slice thickness and 0.5 mm slice thickness reconstruction were also compared with each other.

3.2.6 Statistical analysis

We calculated the correlation coefficient of the slice-by-slice calcium volumes in IVUS-VH with CAC obtained with different thresholds. Sensitivity, specificity, positive predictive value (PPV) and negative predictive value (NPV) assessment were done to find the optimal attenuation threshold for the population of patients studied. In our case, the true positive (tp) is the total number of slices having calcium in both CT and IVUS-VH images, the true negative (tn) is the total number of slices without calcium lesions in both the modalities, false positive (fp) is the total number of slices having calcium in the CAC images but not in the IVUS-VH images, and false negative (fn) is the total number of slices having calcium in IVUS-VH images but not in CAC images. Then, the statistical measures are defined as,

$$Sensitivity = \frac{tp}{tp + fn}, \tag{3.11}$$

$$Specificity = \frac{tn}{tn + fp}, \tag{3.12}$$

$$PPV = \frac{tp}{tp + fp}, \tag{3.13}$$

$$NPV = \frac{tn}{tn + fn}. \tag{3.14}$$

As the correlation coefficient only finds the relation between data and scaling one of the data by a constant term does not have any effect on the correlation. Data that have high correlation can have poor agreement [62]. Therefore we also used Bland-Altman analysis [52] to find the difference in the calcium volume reported by CT and IVUS-VH. The Bland-Altman analysis is the plot of the difference of two observations against their average and is used to measure the agreement between the two observation. Low limit of agreement (low difference) is desired in calcium quantified in the CT and the IVUS-VH since the actual amount of calcium in a patient should be reported same by both the imaging modalities.

Based on the presence or absence of calcium on each slice we conducted the receiver operating characteristic (ROC) [63, 64] analysis to compare the 0.5 mm and 3.0 mm reconstructions with respect to the IVUS-VH volume. The ROC curve plots the true positive rate against the false positive rates at all the thresholds considered. The true positive rate which is the fraction of true positives out of all positives is same as the *sensitivity*, and the false positive rate which is the fraction of false positives out of all negatives is same as *1 - specificity*. The area under a ROC curve represents the accuracy of the classifier with a higher area indicating lower number of false positives and false negatives.

3.3 Experiments

A total of 23 patients were studied, 14 of which had intermediate to severe coronary artery disease. The 14 patients with coronary artery disease had undergone both CAC and IVUS-VH imaging while the 9 normal patients had only CAC taken. Since, the conventional CAC score has been established to have high accuracy of detecting calcium, we assumed the calcium volume per slice in the normal patient to be 0 as no calcium was detected in the normal patients in the non-contrast CT scan. The isotropic CAC and IVUS-VH were co-registered using the aforementioned registration methods, and the calcium quantification corresponding to different thresholds in CAC were compared with the registered IVUS-VH. The 3.0 mm slice thickness and 0.5 mm slice thickness reconstructions were compared in terms of different statistical measures mentioned above and also with respect to the calcium volume over-estimation in comparison to the IVUS-VH derived calcium volume.

3.4 Results

As shown in figure 3.8, the slice-by-slice CAC quantification in two different reconstructions with 0.5 mm and 3.0 mm slice thickness using 130 HU threshold have the correlation coefficients of 0.79 ($p < 0.0001$) and 0.75 ($p < 0.0001$) respectively with the IVUS-VH derived calcium volume. Figure 3.9 shows the limits of agreements for CAC 0.5 mm vs IVUS-VH and 3.0 mm vs IVUS-VH using the 130 HU threshold. Table 3.2 summarizes these results along

with sensitivity, specificity, PPV, NPV, and the over-estimation of calcium quantification using the 130 HU threshold. The table shows the specificity of 0.5 mm CAC is lower than that of 3.0 mm CAC indicating that the 130 HU is not an optimal threshold for calcium quantification in 0.5 mm slice thickness.

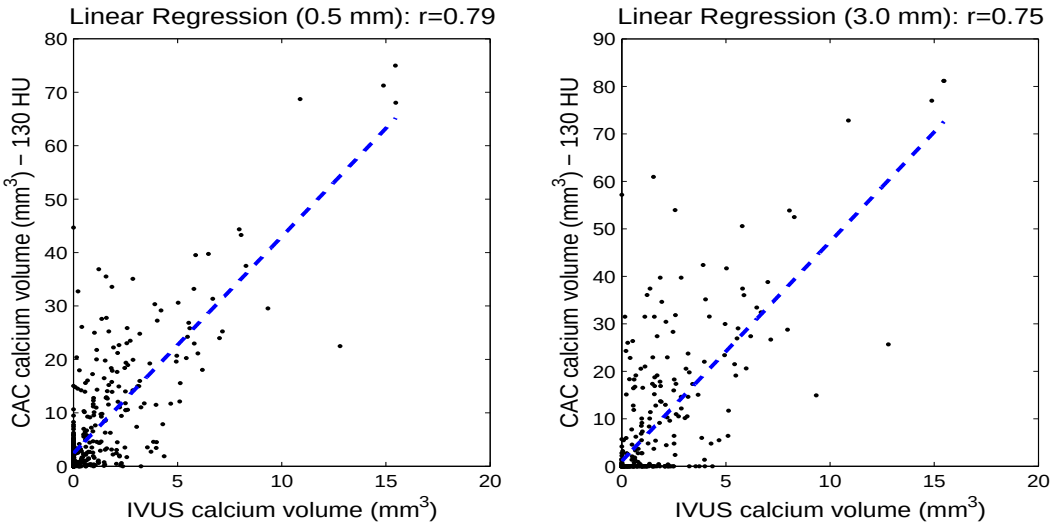

Figure 3.8 Linear regression of 0.5 mm with IVUS-VH, (a) and 3.0 mm with IVUS-VH calcium volumes using the threshold of 130 HU.

Table 3.2 Comparison of the calcium quantifications in the 0.5 mm, and the 3.0 mm reconstructions at the threshold of 130 HU by validating against the IVUS-VH calcium volume. The correlation coefficient, sensitivity, specificity, PPV, NPV, overestimation, and the limits of agreement are shown for each reconstruction using the 130 HU thresholds.

Slice(mm)	corr.	Sens.	Spec.	PPV	NPV	overest.	diff(HU)
0.50	r = 0.79, p < 0.0001	0.95	0.24	0.57	0.82	4.06	-5.83 ± 18.30
3.00	r = 0.75, p < 0.0001	0.56	0.91	0.89	0.62	4.62	-5.11 ± 22.81

As shown in figure 3.10 the CAC quantification in 2 different reconstructions with 0.5 mm and 3.0 mm slice thickness are significantly correlated with each other (r = 0.92, p < 0.0001) and have low difference range using the threshold of 130 HU.

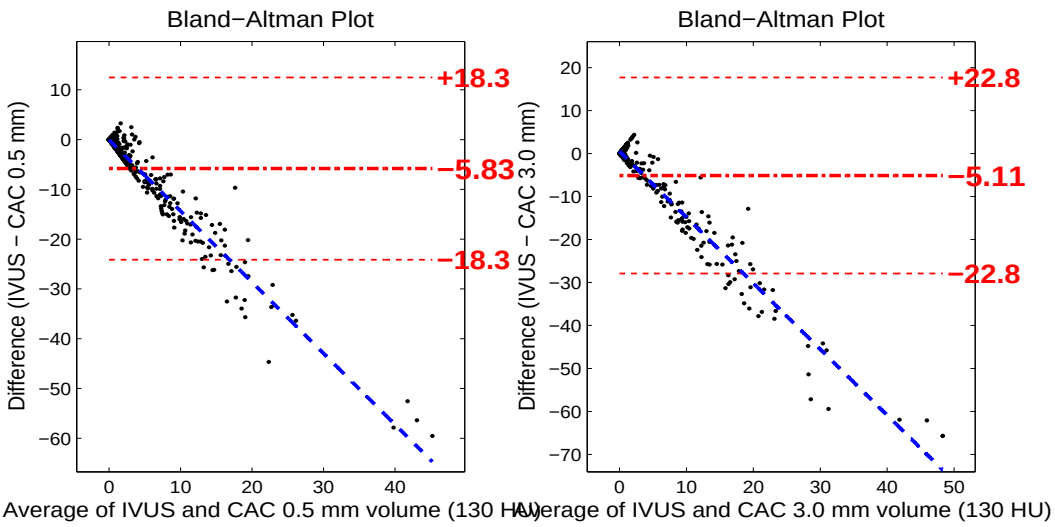

Figure 3.9 Bland-Altman analysis of (a) CAC 0.5 mm with IVUS-VH, and (b) CAC 3.0 mm with IVUS-VH using the threshold of 130 HU.

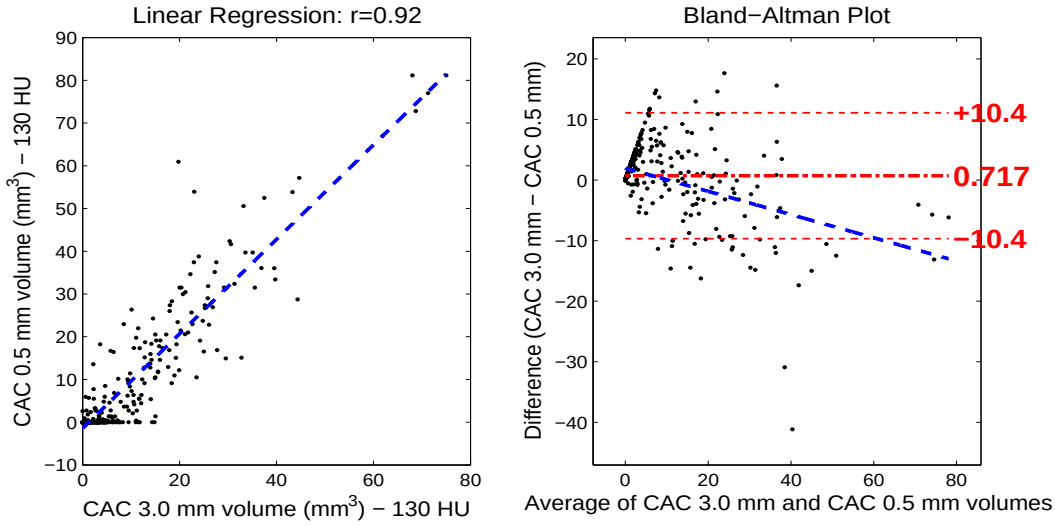

Figure 3.10 Linear regression and limit of agreement between the 0.5 mm CAC and 3.0 mm CAC using the cutoff of 130 HU.

Figure 3.11 shows that the sensitivity, specificity, PPV and NPV curves for 0.5 mm CAC converge at higher thresholds than 3.0 mm CAC thus suggesting optimal values of these parameters at higher cutoff threshold for 0.5 mm CAC. To find and optimal threshold in both 0.5 mm and 3.0 mm reconstructions we choose the closest top-left point [63, 65] on the corresponding ROC curves. The cutoff threshold corresponding to the closest top-left point as shown in figure 3.14 (b) minimizes the $(1 - sensitivity)^2 + (1 - specificity)^2$.

The two reconstructions were then compared with respect to different parameters as shown in Table 3.3 at their corresponding optimal thresholds.

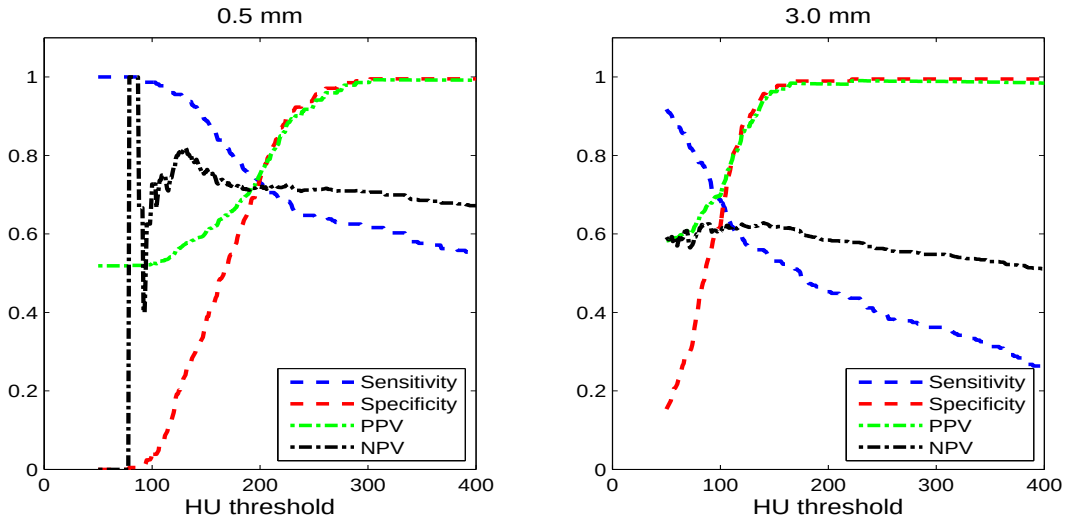

Figure 3.11 Sensitivity, Specificity, NPV, and PPV of 0.5 and 3.0 mm CT calcium volume in comparison to the IVUS-VH calcium volume.

Figure 3.12 shows the regression analysis and the limits of agreement between 0.5 mm CAC and 3.0 mm CAC at the optimal thresholds of 226 HU and 130 HU respectively. As shown in figure 3.13,the correlation coefficient of 0.5 mm CAC and 3.0 mm CAC with IVUS-VH using the corresponding optimal thresholds are both around 0.75. However, figure 3.14 (a) shows that 0.5 mm reconstruction has higher correlation than 3.0 mm reconstruction with IVUS-VH at all cutoff thresholds. The area under the ROC curve is higher in the 0.5 mm reconstruction than the 3.0 mm reconstruction as shown in figure 3.14(b). The higher

Table 3.3 Comparison of the calcium quantifications in the 0.5 mm, and the 3.0 mm reconstructions at the corresponding optimal thresholds by validating against the IVUS-VH calcium volume. The correlation coefficient, sensitivity, specificity, PPV, NPV, overestimation, and the limits of agreement are shown for each reconstruction at the corresponding optimal thresholds.

Slice(mm)	Thresh. (HU)	r	Sens.	Spec.	PPV	NPV	overest	diff(HU)
0.50	226	r = 0.76, p < 0.0001	0.68	0.90	0.88	0.73	2.78	-2.43 ± 12.36
3.00	120	r = 0.75, p < 0.0001	0.59	0.87	0.86	0.63	2.22	-5.64 ± 24.11

area in the ROC of 0.5 mm suggests that calcium can be more accurately detected in a 0.5 mm reconstruction than a 3.0 mm reconstruction. This is also confirmed by the lower limit of agreement for 0.5 mm CAC quantification than the 3.0 mm CAC using the corresponding optimal thresholds as shown in figure 3.15.

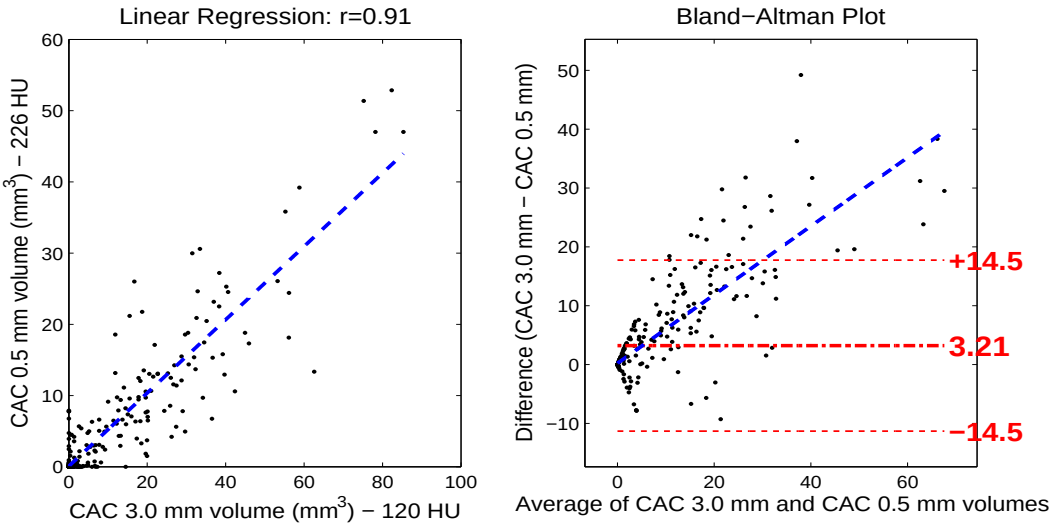

Figure 3.12 Linear regression and limit of agreement between the 0.5 mm CAC and 3.0 mm CAC using the cutoff thresholds of 226 HU and 120 HU respectively.

We also used the closest top-left method to find out optimal cutoff threshold in the CT scan of individual patients. Table 3.4 shows the optimal threshold of an individual patient and the corresponding noise level in the CT scan. Both the optimal thresholds and the noise

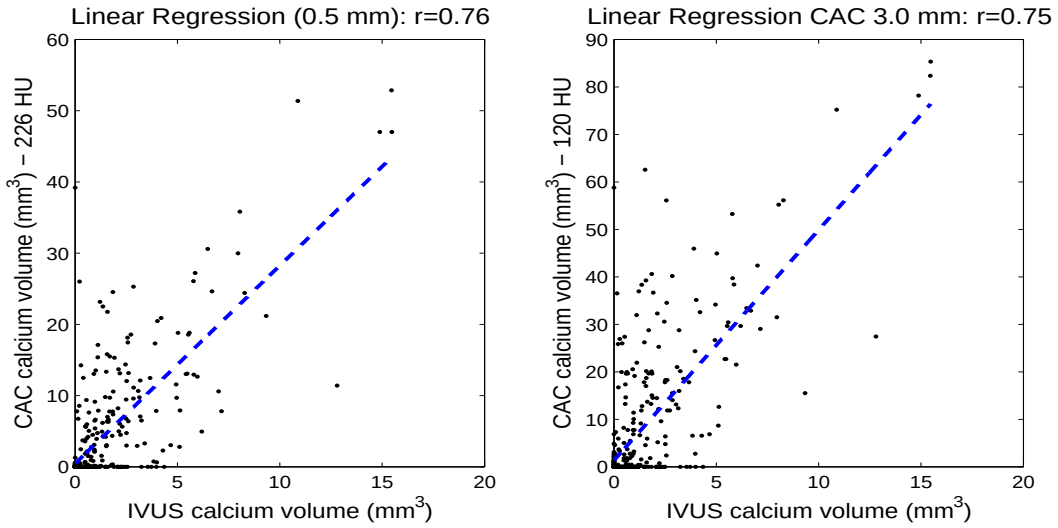

Figure 3.13 Linear regression of 0.5 mm with IVUS-VH, (a) and 3.0 mm with IVUS-VH calcium volumes at the optimal cutoff thresholds of 226 HU and 120 HU respectively.

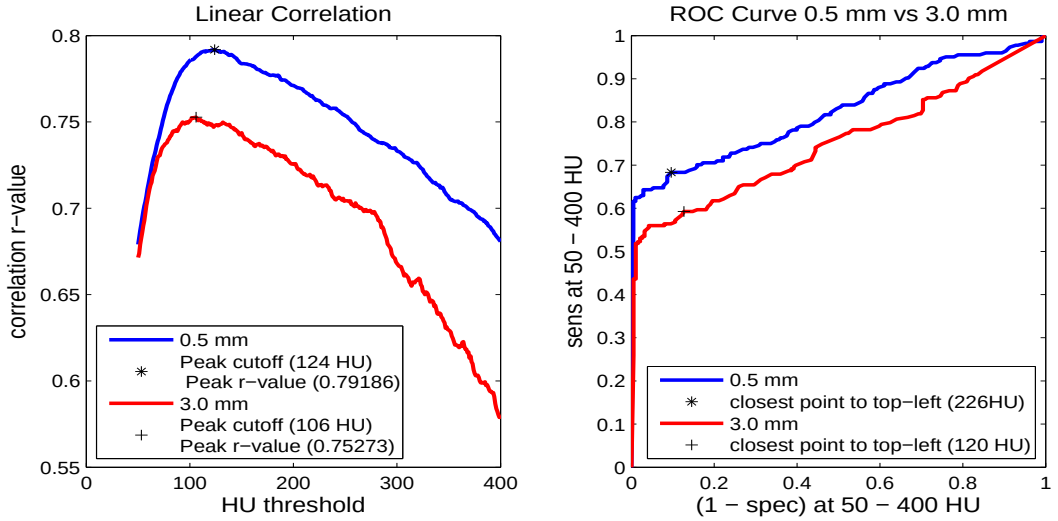

Figure 3.14 Correlation coefficients and the ROC curve of the 0.5 mm and 3.0 mm reconstructions with the IVUS-VH. (a) Correlation coefficient of 0.5 mm and 3.0 mm reconstructions at different thresholds with the IVUS-VH calcium volume. (b) ROC curve for 0.5 mm and 3.0 mm reconstructions in the range of 50 - 400 HU. The closest top-left points for each curve is marked.

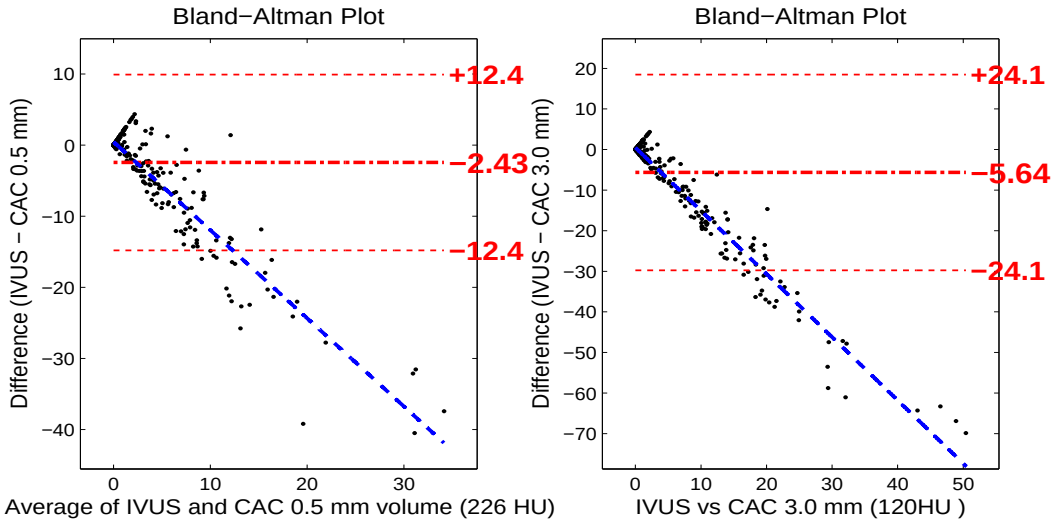

Figure 3.15 Bland-Altman analysis of (a) CAC 0.5 mm with IVUS-VH, and (b) CAC 3.0 mm with IVUS-VH using the optimal cutoff thresholds of 226 HU and 120 HU respectively.

level in 0.5 mm CAC are higher than those in 3.0 mm CAC for individual patients. The noise level of a CT volume was measured as the standard deviation of a small area in the aorta. We found the optimal cutoff threshold was related to the noise level linearly with the correlation coefficient of 0.72 ($p < 0.0001$) as shown in figure 3.16. This indicates the possibility of estimation of optimal cutoff threshold from the statistics of voxel intensity in aorta which we plan to investigate further in the dissertation.

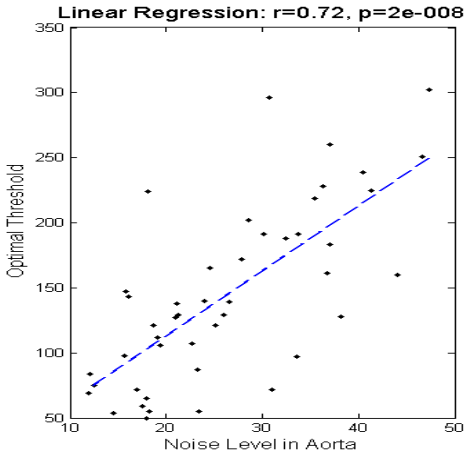

Figure 3.16 Linear regressions analysis of the optimal cutoff thresholds and the noise levels.

Table 3.4 Optimal cutoff thresholds and the corresponding noise levels in the aorta.

Optimal cutoff (HU) 3.0 mm	Noise level (HU)	Optimal cutoff (HU) 0.5 mm	Noise level (HU)
75	12.49	121	25.12
59	17.55	128	38.23
69	11.96	127	20.95
84	12.02	129	21.19
54	14.47	129	26.00
87	23.20	225	41.31
121	18.67	260	36.99
55	18.18	161	36.74
143	16.07	296	30.75
50	17.95	183	36.96
224	18.17	228	36.28
72	16.99	72	30.98
55	23.45	160	44.07
65	17.99	97	33.60
147	15.87	202	28.57
98	15.73	172	27.92
165	24.62	302	47.33
107	22.66	191	33.70
140	24.05	239	40.49
139	26.56	251	46.62
138	21.15	219	35.46
106	19.41	188	32.45
112	19.08	191	30.12

3.5 Discussion and Conclusion

In this study we compared the coronary artery calcium (CAC) quantified by conventional CT with 3.0 mm slice-thickness reconstruction and the 0.5 mm isotropic reconstruction at different cutoff thresholds by performing statistical analysis with the IVUS-VH derived calcium volume. We developed a software to manually extract a desired coronary artery from the CT volume images and manually registered them to the corresponding vessel in IVUS-VH by visually comparing the landmarks and by panning the calcium volume curves obtained from both the modalities.

We used the closest top-left point [63, 65] from the ROC curve in order to find an optimal threshold. We found the 120 HU to be optimal for calcium quantification in the 3.0 mm slice thickness reconstruction. The optimal cutoff threshold found is close to the conventional cutoff threshold of 130 HU. However, for 0.5 mm reconstruction we found that in order to achieve better calcium quantification, the threshold should be increased to 226 HU. The CAC quantification done in 0.5 mm CAC using optimal threshold has higher sensitivity, specificity, NPV, PPV, and lower difference range to the IVUS-VH derived calcium volume as compared to the quantification in 3.0 mm CAC with the corresponding optimal threshold.

Statistical analysis by using the linear correlation (r-value) only quantifies the linear relationship of the calcium quantified by CAC with that of IVUS-VH, but does not consider the accuracy of detecting calcified slices. The sensitivity analysis gives the probability of accurately detecting actual calcified slices in a CAC image; and specificity analysis gives the ability to correctly identify the absence of calcified slices. The PPV finds the true proportion of positive values among all positives classified by the CAC and the NVP identifies the true proportion of negative values. We maximized specificity, PPV and correlation coefficient in order to achieve the optimal cutoff threshold. In our case of slice-by-slice calcium volume quantification specificity and PPV were relatively more important than sensitivity and NPV because we wanted to minimize the total false positives by CAC quantification, in order for the CAC to be clinically reliable since the presence of false positives may indicate falsely

identifying a healthy tissue as calcium. The high numbers of false negatives that gave rise to relatively low sensitivity and NPV, on the other hand, may be decreased by considering total number of lesions rather than the presence or absence of calcium on a slice-by-slice basis.

We observed over-estimation in both the 0.5 mm and 3.0 mm reconstructions. The over-estimation may be explained by partial volume effect which is caused by classifying a voxel with partial volume of calcium completely as calcium, thus giving rise to blooming artifact which gives an enlarged appearance to densely calcified plaques. The probability of finding high proportion of calcium in a voxel has been noted to be different for different HU thresholds [66].

We use IVUS-VH as "gold standard" to validate the CT calcium quantification because it has high predictive accuracy for detecting calcium, high spatial resolution and a high sensitivity of detecting small volume of calcium. However, IVUS-VH produces acoustic shadow behind the lining of dense calcium which may result in an inaccurate quantification of calcium. The IVUS-VH uses sound wave reflected from different tissue to construct their image. The sound wave emitted from the IVUS-VH catheter may not penetrate the calcium lining in the arterial wall and the tissue underneath the calcium lining appears as a dark area in the IVUS-VH image known as the acoustic shadow. The possible under-estimation of calcium volume due to the shadow might be another factor contributing to the apparent over-estimation by CT quantification of calcium. Other limitations of the study may be due to the manual extraction of vessels and manual registration using visual alignment and curve panning. The manual steps might alter the accuracy of calcium quantification and registration.

In this work we found that the 0.5 mm slice-thickness reconstruction is better than 3.0 mm slice-thickness reconstruction for detecting calcium with higher sensitivity, specificity, PPV, NPV, and lower mean difference range and over-estimation levels. Hence the use of 0.5 mm slice-thickness instead of the conventional 3.0 mm reconstruction improves the calcium quantification accuracy. However, the calcium cutoff threshold for 0.5 mm slice-thickness

reconstruction should be adjusted by increasing it more than the conventional 130 HU in order to achieve the better performance.

Different parameters that affect the calcium volume over-estimation and the reduction of over-estimation between CT and IVUS-VH quantification may be explored in the dissertation work. In this study we also found that the cutoff threshold is linearly related to the noise level in aorta. Hence, the optimal cutoff threshold may be formulated as a function of the noise in the CT scan. In the dissertation we also plan to study various noise measurement techniques and their relation to the optimal cutoff thresholds. Calcium blooming artifact reduction for better accuracy of quantification may also be explored.

CHAPTER 4

AUTOMATIC CORONARY ARTERY RECONSTRUCTION

4.1 Introduction

Coronary artery reconstruction is segmentation of the arteries from the background and its geometric representation. The artery reconstruction is useful for visualization, different anomaly detection, and their quantification. Segmentation or the extraction of the arteries from the 3D volume of a CT scan can be done by using an active contour models such as the snake deformable model [57] or a level-set method [46, 67]. In an active contour model, an initial curve or a surface in 3D is iteratively evolved in shape and location under the constraint of different forces such as the gradient of image, or the elasticity of the surface, to fit to the desired object to be segmented. While these methods are robust and popular for extracting different anatomical objects in medical images, it is difficult to adapt them to narrow anatomical surfaces such as the arteries.

The contrast material has a certain intensity range in the CT and hence the anatomical structures such as ventricle, aorta, arteries, etc., through which the contrast material is flowing at the time of acquisition can be segmented by selecting voxels in the particular intensity range. Other anatomical structures such as myocardial tissue or the heart muscle do not get the contrast material and hence appear with lower intensity range. The heart can be visualized with distinct anatomical structures based on the difference in the intensity range between different structures. Figure 4.1 shows visualization of a heart using ray casting [68] method. The visualization was done by using the visualization toolkit which is an open-source C++ class library for 3D computer graphics, image processing and visualization [69].

The left ventricle, aorta and coronary arteries that receive the contrast have higher HU values and appear with high opacity. The right ventricle and the myocardial layers have lower HU value ranges and appear semi-transparent to transparent.

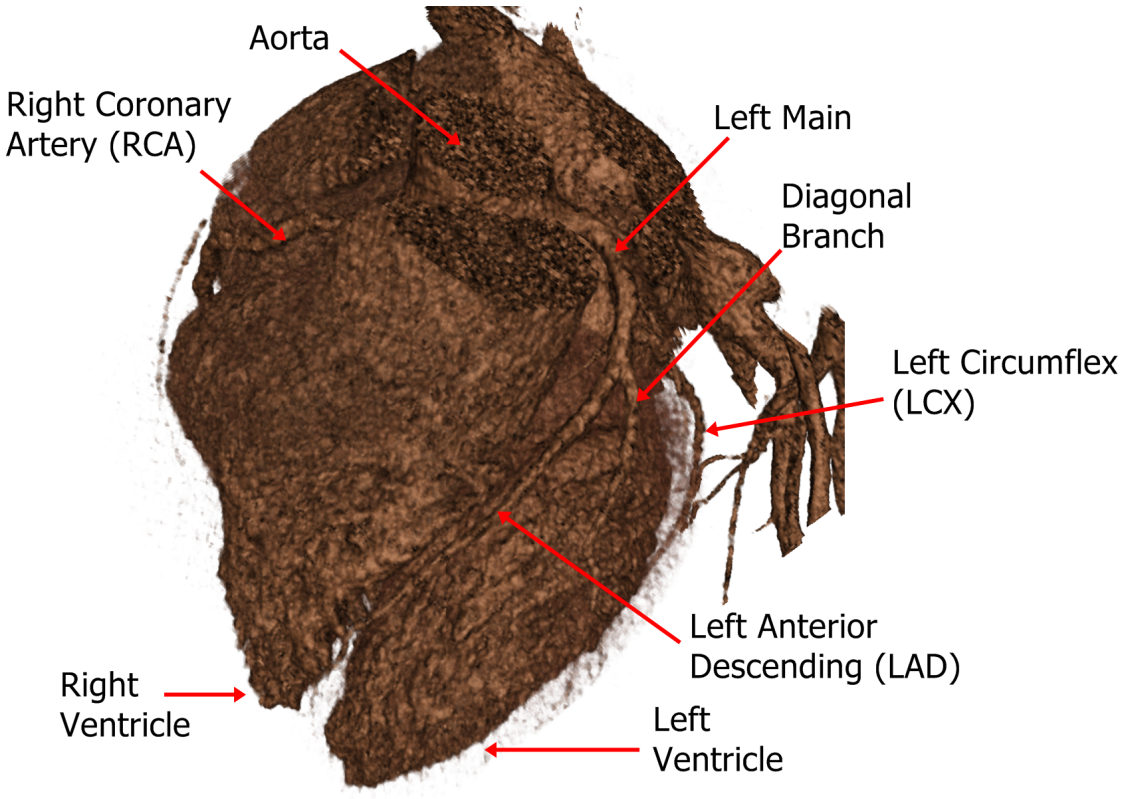

Figure 4.1 CT volume visualized by using ray casting method showing the heart and different coronary arteries. The voxels with higher intensity range (aorta, arteries, and ventricles) were assigned higher opacity and those with lower intensity range (myocardial wall) were assigned lower opacity.

Utilizing the higher intensity range of the contrast material simpler intensity based approaches such as isosurface extraction, can be used for segmentation. An isosurface is a 3D surface formed by points with a constant value known as isovalue. A range of thresholds in HU can be used as an isovalue, such that the isosurface is formed by selecting the voxels in the range. The isosurface can then be visualized by using methods such as the marching cube algorithm [70, 71] which generate triangular meshes from the given data points in a grid.

41	70	239	413	410	397	390	365	284	161	33	-50
57	117	287	383	370	364	391	344	241	131	19	-41
85	79	182	341	362	346	385	385	257	173	75	-19
-4	61	205	305	349	310	344	396	319	213	95	-19
16	139	305	374	389	373	411	387	312	159	23	-29
54	101	239	288	363	455	459	374	288	150	9	-61
30	98	263	282	361	408	395	329	295	175	54	-66
-17	72	289	386	416	435	433	343	263	185	79	-101
14	31	120	286	408	490	413	270	207	146	70	-131
-1	-81	-130	130	316	383	337	272	233	185	153	-8
-62	-148	-165	121	237	227	230	177	163	178	119	10
-98	-86	-30	78	105	156	162	70	38	54	2	-18
-100	-26	55	77	52	70	64	44	31	11	-41	-32

(a)

0	0	0	1	1	1	1	1	1	0	0	0
0	0	1	1	1	1	1	1	0	0	0	0
0	0	0	1	1	1	1	1	0	0	0	0
0	0	0	1	1	1	1	1	1	0	0	0
0	0	1	1	1	1	1	1	1	0	0	0
0	0	0	1	1	0	0	1	1	0	0	0
0	0	0	1	1	1	1	1	1	0	0	0
0	0	1	1	1	0	0	1	0	0	0	0
0	0	0	1	1	0	1	0	0	0	0	0
0	0	0	0	1	1	1	0	0	0	0	0
0	0	0	0	0	0	0	0	0	0	0	0
0	0	0	0	0	0	0	0	0	0	0	0
0	0	0	0	0	0	0	0	0	0	0	0

(b)

Figure 4.2 Connected component analysis in a section of a CTA slice. (a) A section of CTA slice. (b) The section thresholded and within the range of 300 ± 25 HU and the connected component in shaded area.

A region growing algorithm [58] is a similar approach which requires the voxels in an intensity range to be geometrically connected as well. In this method, the segmentation starts with one or more seed voxels and seeks connected components to which the seed voxels belong. A connected component is a set of voxels in which there is a path from a voxel to any other voxels in the set. A path exists between two voxels if they are adjacent to each other or a voxel can be reached from another by tracing through a set of adjacent voxels. Different definitions of adjacency can be used; for instance, in a 2D image, two pixels are 4-adjacent if one lies to left, right, up or down to another and both the pixels are in a specified intensity range. With 8-adjacency, the diagonal pixels are also considered adjacent. Similarly, in 3D 6-, 18-, and 26-adjacency can be used for defining adjacent voxels.

Figure 4.2 shows a connected component formed by selecting pixels in the range $\mu \pm k\sigma$, where $\mu = 350\ HU$, $\sigma = 25\ HU$, and $k = 3$. Figure 4.2 (a) show a section of a CTA slice before thresholding, 4.2 (b) shows the connected component after thresholding the image, so that the HU values in the range 350 ± 75 HU are made 1 and all others 0. The shaded regions of 1's correspond to the connected component or the desired object to be segmented. The value of μ and σ are somewhat arbitrary here, but they may be replaced by more accurate estimate of the mean and standard deviation of the contrast material in the artery. Extension to 3D can be done similarly. Figure 4.3 shows a volume that includes ventricle, portion of the aorta and the right coronary artery (RCA). The volume was extracted by using the region growing approach with a threshold of 190 HU, such that any adjacent voxels of 190 HU or more are selected in the connected component. The desired coronary artery can be split from the large connected component with some manual interactions, for example, by using a plane passing through a point identified by a user at the base of the coronary artery.

Figure 4.3 Volume extracted by selecting pixels with intensity >= 190HU, smoothing, and selecting the largest connected component.

The range of intensity for the contrast material can vary across different CTA volumes depending upon the amount of contrast concentration, patient physiology, contrast injection rate, time elapsed since contrast administration, image noise etc. [24]. Furthermore, in smaller arteries such as the RCA, the contrast concentration is not uniform across its length and the narrow distal ends may by noisy. Usually a high threshold fails to include the distal end with low contrast concentration and may even lead to fragmentation of different branches. A low threshold, on the other hand can include myocardial tissue making it difficult to separate the artery by using connected component analysis. Therefore a thresholding step is not sufficient for accurate segmentation of vessels. Figure 4.4 (a) shows thresholding and connected component extraction in a different patient than the one shown in figure 4.3. Due to a lower contrast concentration, the threshold of 190 HU was high enough to exclude the narrower distal ends. Figure 4.4 (b) shows the fragmented ends of the right coronary artery. Meanwhile, the right ventricle was also included with the threshold. Increasing the threshold to 300 HU was sufficient to separate the arteries from background but this led to exclusion of larger portion of the distal end of the RCA as shown in figure 4.4 (c). Larger portion of arteries were included by decreasing the threshold to 120 HU at the cost of including a portion of myocardial wall fused with the arteries as shown in figure 4.4 (d). Therefore it is difficult to find a good threshold for accurate segmentation of the arteries. Furthermore, it is difficult to isolate the smaller arteries from the aorta and the ventricles. Therefore, we enhance the arteries by using a geometry based filter as discussed in the section below.

4.2 Automatic vessel extraction

We enhance the vessels based on their local geometry analysis by using eigenvalues of the second order derivative matrix at a point, also known as the Hessian matrix. With the assumption that the volume function I is second order continuous in a neighborhood $\delta\mathbf{x}$ of a point $\mathbf{x}_0$, the local intensity variation in the neighborhood of $\mathbf{x}_0$ can be approximated by Taylor series expansion as,

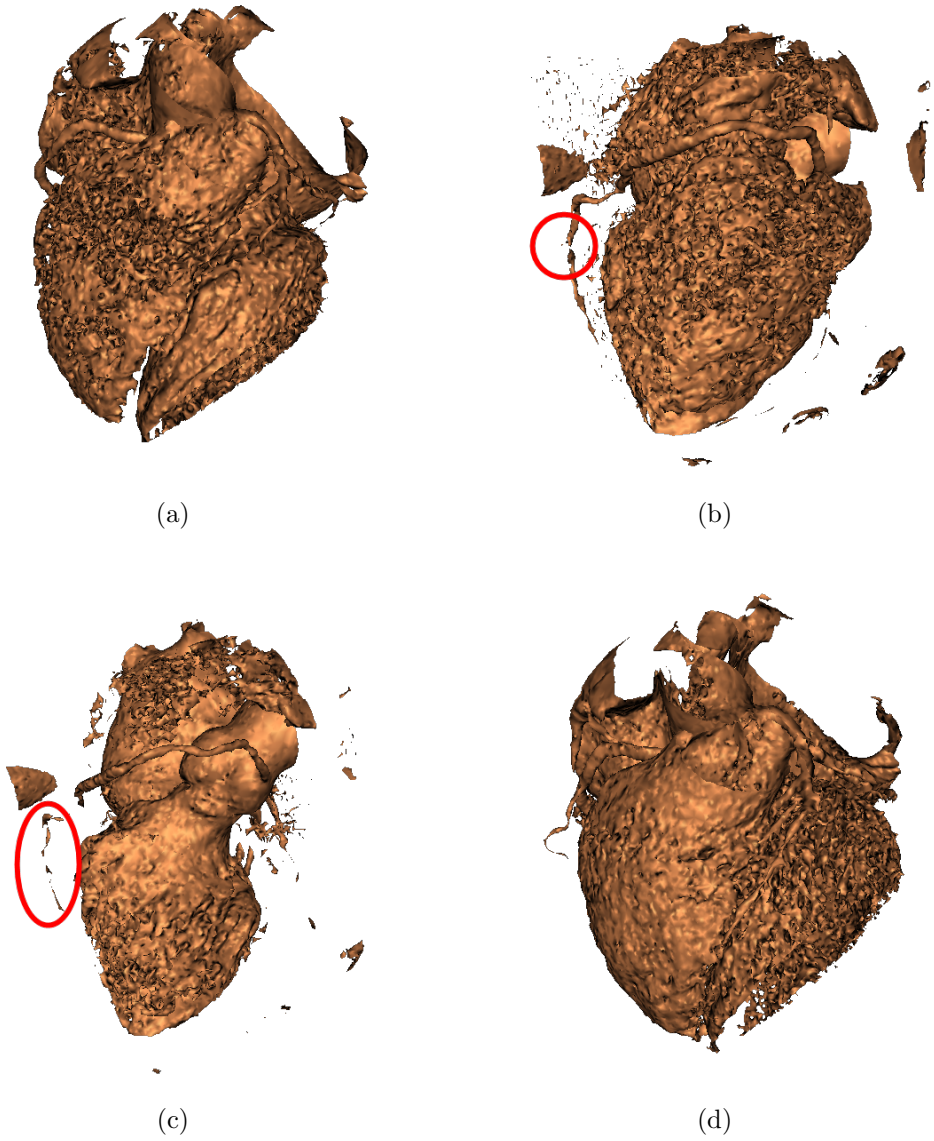

(a) (b)

(c) (d)

Figure 4.4 Inaccurate artery segmentation by using absolute intensity based cutoff thresholds. (a) Volume extracted with a threshold of 190HU, smoothing, and selecting the largest connected component. (b) Same volume with all the connected components showing a distal end of RCA not connected to the main part (circle shows the discontinuity). (c) Volume selected with a cutoff of 300 HU with a large fragment of RCA not connected (circle shows the disconnected fragment). (d) Volume selected with a cutoff of 120 HU with the branches of left coronary artery connected to a portion of myocardial wall.

$$I(\mathbf{x}_0 + \delta\mathbf{x}) \approx I(\mathbf{x}_0) + \delta\mathbf{x}^T \nabla I(\mathbf{x}_0) + \delta\mathbf{x}^T \mathbf{F}(I(x_0))\delta\mathbf{x}, \tag{4.1}$$

where $\mathbf{x} = [x, y, z]^T$ is a column vector representing a point in 3 dimension, $\nabla I(\mathbf{x}_0)$ is the gradient and $\mathbf{F}(I(\mathbf{x}_0))$ is the Hessian at point $\mathbf{x}_0$. The gradient is a 2×1 column vector for a 2-dimensional image, and 3×1 column vector for a 3-dimensional image written as,

$$\nabla I(\mathbf{x}_0) = \begin{pmatrix} \dfrac{\partial I(\mathbf{x}_0)}{\partial x} \\ \dfrac{\partial I(\mathbf{x}_0)}{\partial y} \\ \dfrac{\partial I(\mathbf{x}_0)}{\partial z} \end{pmatrix}, \tag{4.2}$$

and represents the first order local structure or the rate of intensity variation along each dimension. The Hessian is a square matrix of the second order partial derivatives of the image at the point and is a $2x2$ matrix for a 2-dimensional image, and a $3x3$ matrix for a 3-dimensional image. For a 3-dimensional image I the Hessian $\mathbf{F}$ at a point is composed as,

$$\mathbf{F}(I(\mathbf{x}_0)) = \begin{pmatrix} \dfrac{\partial^2 I(\mathbf{x}_0)}{\partial x^2} & \dfrac{\partial^2 I(\mathbf{x}_0)}{\partial y \partial x} & \dfrac{\partial^2 I(\mathbf{x}_0)}{\partial z \partial x} \\ \dfrac{\partial^2 I(\mathbf{x}_0)}{\partial x \partial y} & \dfrac{\partial^2 I(\mathbf{x}_0)}{\partial y^2} & \dfrac{\partial^2 I(\mathbf{x}_0)}{\partial z \partial y} \\ \dfrac{\partial^2 I(\mathbf{x}_0)}{\partial x \partial z} & \dfrac{\partial^2 I(\mathbf{x}_0)}{\partial y \partial z} & \dfrac{\partial^2 I(\mathbf{x}_0)}{\partial z^2} \end{pmatrix} \tag{4.3}$$

In digital images with fixed resolution, the derivatives are calculated using finite difference approximations. Assuming the voxel is unit size in all three dimension, one of the ways to represent the partial derivatives is, [58],

$$\frac{\partial I(\mathbf{x})}{\partial x} = I(x+1,y,z) - I(x,y,z) \tag{4.4}$$

$$\frac{\partial^2 I(\mathbf{x})}{\partial x^2} = I(x+1,y,z) + I(x-1,y,z) - 2I(x,y,z) \tag{4.5}$$

$$\frac{\partial^2 I(\mathbf{x})}{\partial x \partial y} = I(x+1,y+1,z) + I(x-1,y-1,z) - I(x+1,y-1,z), -I(x-1,y+1,z). \tag{4.6}$$

The partial derivatives $\frac{\partial^2 I(\mathbf{x})}{\partial^2 y}, \frac{\partial^2 I(\mathbf{x})}{\partial^2 z}, \frac{\partial^2 I(\mathbf{x})}{\partial x \partial z}$ can be defined similarly. For a second order continuous function, the Hessian matrix is symmetric, thus $\frac{\partial^2 I(\mathbf{x})}{\partial y \partial x} = \frac{\partial^2 I(\mathbf{x})}{\partial x \partial y}$, and $\frac{\partial^2 I(\mathbf{x})}{\partial x \partial z} = \frac{\partial^2 I(\mathbf{x})}{\partial z \partial x}$.

The second order derivative gives the curvature or a sharp variation in intensity. Therefore, it is commonly used for identifying different image structures such as point, line, edge etc [58]. For example, figure 4.5 shows a Gaussian profile $P = e^{\frac{-x^2}{2\sigma_p^2}}$ and its second derivative $\frac{d^2P}{dx^2}$. The second derivative is largest at the peak corresponding to the point of largest curvature of the profile $P(x;\sigma)$. It is to be noted that for a profile higher than its surrounding, the response is negative or a minima and the opposite is true for a profile lower than its surrounding. In case of three dimensions, a bright local structure in dark background has a negative definite Hessian matrix, i.e., all three eigenvalues are negative. This is also known as the second order sufficient condition for a point to be a local maxima [72]. Conversely, a local minima or a dark structure in a bright background has a positive definite Hessian matrix.

The second order derivative is very sensitive to noise. Therefore, smoothing the image, for example, by convolving with Gaussian is an important preprocessing-processing step in second order structure analysis. The popular Laplacian of Gaussian (LoG) filter [73] used for edge detection is based on finding the zero-crossing of an imaginary line that connects two extreme positive and negative values of the second derivative. The Gaussian component of the filter reduces the effect of noise and the Laplacian

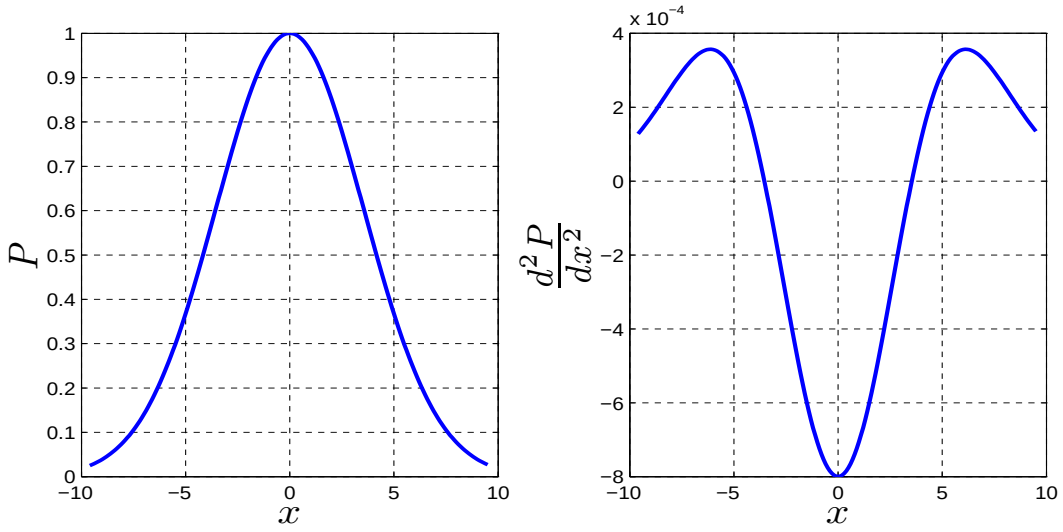

Figure 4.5 Gaussian Profile $P = e^{\frac{-x^2}{2\sigma_p^2}}$ (left) and its second derivative (right).

$$L = \frac{\partial^2 I(\mathbf{x})}{\partial^2 x} + \frac{\partial^2 I(\mathbf{x})}{\partial^2 y}, \tag{4.7}$$

finds the maxima and minima required to extract the zero-crossing. The LoG filter uses only the Laplacian or the sum of diagonal entries of the Hessian. Eigenvector and eigenvalue analysis of the full Hessian matrix provide important geometric information about the local structure. Such information are used to construct filters that enhance a tube like structures [74, 75, 76] and can be a useful preprocessing step in the segmentation of blood vessels in CTA and MRA images. Once the Hessian matrix is computed, the second derivative in any particular direction $\mathbf{d}$ is given by,

$$\frac{\partial^2 I}{\partial \mathbf{d}^2} = \mathbf{d}^T \mathbf{F} \mathbf{d}. \tag{4.8}$$

If $\lambda_1, \lambda_2, \lambda_3$ are the eigenvalues of the Hessian $\mathbf{F}$ with $|\lambda_1| \geq |\lambda_2| \geq |\lambda_3|$, and $\mathbf{v}_1, \mathbf{v}_2, \mathbf{v}_3$ are the corresponding eigenvectors, then the largest second derivative is given by the eigenvalue with highest magnitude, λ_1 which is in the direction $\mathbf{v}_1$. The eigenvectors are orthogonal to each other and hence gives a new basis for representation of the image in the order of decreasing second derivative. Using equation 4.8, the eigenvalues may also be represented

as,

$$\lambda_k = \mathbf{v}_k^T \mathbf{F} \mathbf{v}_k, \tag{4.9}$$

where $k = 1, 2, 3$ for a three dimensional image.

For a tubular structure in three dimensions, the second derivative has highest magnitude in the direction perpendicular to the length of the tube and a very small positive or negative second derivatives in the direction along the length of the tube. This is because of the high intensity variation across the cross section of the tube and a very low intensity variation along the length of the tube. A Hessian matrix at a point in the tube will have two eigenvalues of large magnitude and one of small magnitude. Figure 4.6 (a) shows an ideal tube like structure where the higher magnitude eigenvalues λ_1 and λ_2 are along the orthogonal directions $\mathbf{v}_1$ and $\mathbf{v}_2$ both of which are perpendicular to $\mathbf{v}_3$ with λ_3 along the length of the vessel. The signs of λ_1 and λ_2 are negative for a bright tube in dark background and λ_3 is either positive or negative depending on whether the intensity is increasing or decreasing along the length of the vessel. Ideally, for a tubular structure, $|\lambda_3| \approx 0, |\lambda_1|, |\lambda_2| \gg |\lambda_3|$, and $\lambda_1 \approx \lambda_2$ as shown in figure 4.6 (a).

Based on the ratio of the eigenvalue magnitude, and sign several other shapes can be identified. For example, Frangi et al. identified tube-like, plate-like, and blob-like structures in a dark or bright background [76] based on the magnitude and sign of the eigenvalues as shown in the table 4.1.

Eigenvalues of small magnitude in all three directions indicate a noisy structure, whereas eigenvalues of high magnitude in all three directions is either a dark or bright blob depending on their sign. The plate-like structure is shown in figure 4.6 (b), where as indicated in table 4.1, it has a large eigenvalue across the plane and two small eigenvalues in the plane. Similarly, a blob-like structure as shown in figure 4.6 (c), has all three eigenvalues large.

As with the LoG filter, the first preprocessing step before the calculation of Hessian is the convolution of the image with a Gaussian. Since the second derivative is a linear operation, the Hessian of Gaussian smoothed image is the same as the Hessian of the Gaussian convolved

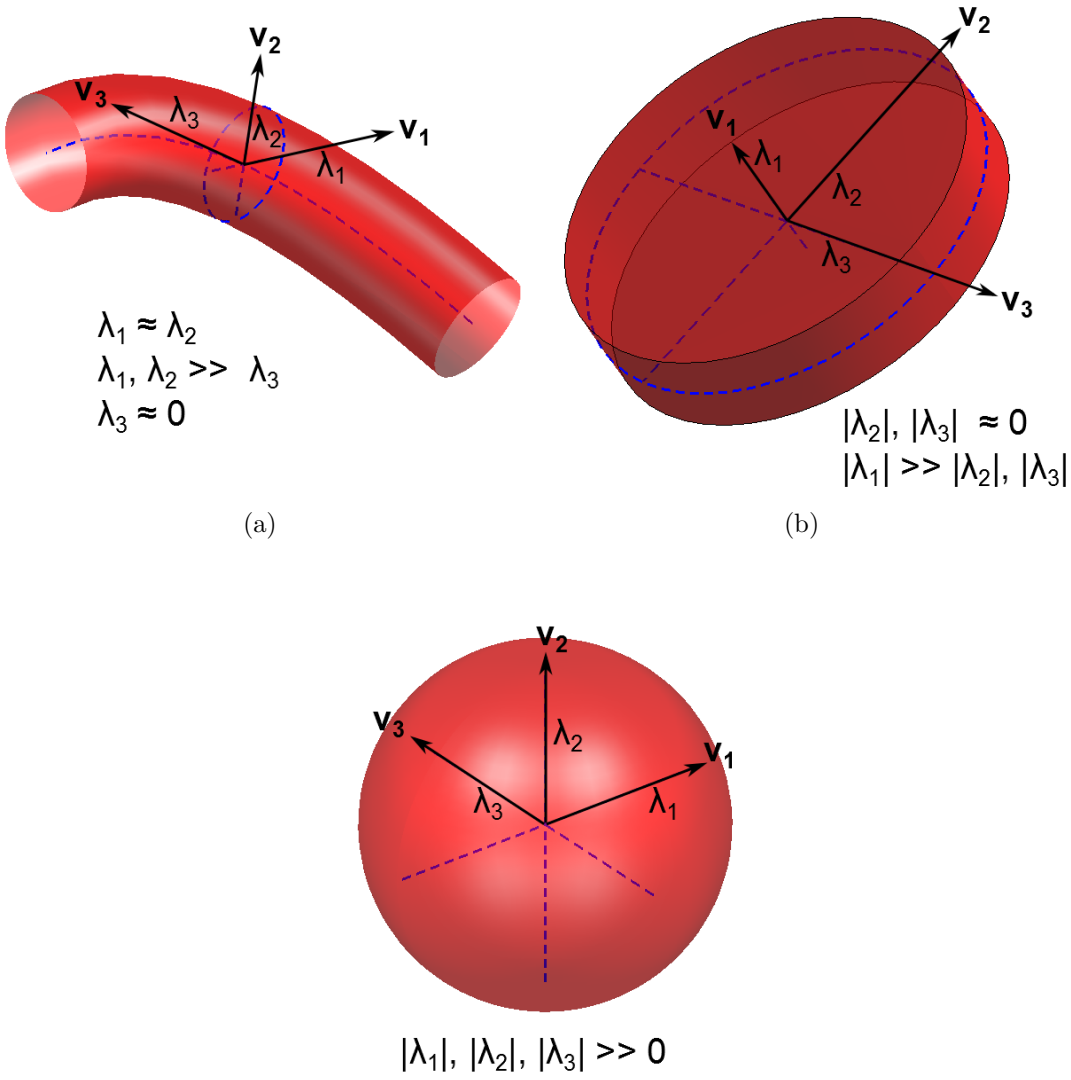

(a) (b)

(c)

Figure 4.6 (a) A Tube-like, (b)a plate-like, and (c) a blob-like second order structures. The black arrows represent the direction of eigenvectors

Table 4.1 Eigenvalues criteria for different of 3-D local structures [76].

Eigenvalues	Possible structure
small $\|\lambda_1\|, \|\lambda_2\|, \|\lambda_3\|$	Noisy
large λ_1, λ_2 $\lambda_1, \lambda_2 < 0$ small $\|\lambda_3\|$	Bright tube
large λ_1 $\lambda_1 < 0$ small $\|\lambda_2\|, \|\lambda_3\|$	Bright plate
large $\lambda_1, \lambda_2, \lambda_3$ $\lambda_1, \lambda_2, \lambda_3 < 0$	Bright blob
large λ_1, λ_2 $\lambda_1, \lambda_2 > 0$ small $\|\lambda_3\|$	Dark tube
large λ_1 $\lambda_1 > 0$ small $\|\lambda_2\|, \|\lambda_3\|$	Dark plate
large $\lambda_1, \lambda_2, \lambda_3$ $\lambda_1, \lambda_2, \lambda_3 > 0$	Dark blob

with the image [58], the partial derivatives of the smoothed image can be written as,

$$\mathbf{F} = \sigma_s^{\gamma} \frac{\partial^2 G(\mathbf{x}; \sigma_s)}{\partial x^2} * I(\mathbf{x}) \tag{4.10}$$

where $G(\mathbf{x}; \sigma_s)$ is the 3-dimensional Gaussian. If it is assumed to be isotropic, i.e., same standard deviation σ_s in all three dimensions, then the Gaussian is given by,

$$G(\mathbf{x}; \sigma_s) = \frac{1}{(2\pi\sigma_s^2)^{\frac{3}{2}}} e^{-\frac{x^2+y^2+z^2}{2\sigma_s^2}}, \tag{4.11}$$

The Hessian matrix can be constructed by finding all the partial derivatives of the image convolved with the Gaussian. In addition to filtering noise, the convolution with Gaussian is useful for tuning the detection of second order structures of different size. For this, different Hessian matrices ($\mathbf{F}_s$) are calculated by changing σ_s. The eigenvalues $\lambda_1(s), \lambda_2(s), \lambda_3(s)$ of these Hessians are tuned to a second order structure of a specific size. In an analogous 1-dimensional case, the response of second order derivative filter given by,

$$R_P(x;\sigma_p,\sigma_s) = \frac{d^2G(x;\sigma_s)}{dx^2} * P(x;\sigma_p), \tag{4.12}$$

for a Gaussian profile $P = e^{\frac{-x^2}{2\sigma_p^2}}$, shown in figure 4.5 is largest and considered to be tuned to profile P when $\sigma_p = \frac{\sigma_s}{\sqrt{2}}$ [75]. The parameter σ_s^γ in equation 4.10 is a normalization parameter and is needed for integration of the response for different standard deviation or different scales σ_s in terms of scale space theory [77].

Based on the ratio of the eigenvalues at each scale, Frangi constructed the following vesselness measure for detecting bright vessels in dark background, [76]

$$V(s) = \begin{cases} 0 & \text{if } \lambda_1 > 0 \text{ or } \lambda_2 > 0, \\ \left(1 - e^{-\frac{A^2}{2a^2}}\right)\left(e^{-\frac{B^2}{2b^2}}\right)\left(1 - e^{-\frac{C^2}{2c^2}}\right) & \text{otherwise ,} \end{cases} \tag{4.13}$$

where

$$A = \frac{|\lambda_2|}{|\lambda_1|}, \tag{4.14}$$

$$B = \frac{|\lambda_3|}{\sqrt{|\lambda_1||\lambda_2|}}, \text{ and} \tag{4.15}$$

$$C = \sqrt{\lambda_1^2 + \lambda_2^2 + \lambda_3^2}. \tag{4.16}$$

The ratio A is high for a tube-like structure and low for a plate-like structure, the ratio B is high for a blob-like structure, and C is high if there is a presence of any second-order structure and is low for a plain background. Hence, the first factor $\left(1 - e^{-\frac{A^2}{2\alpha^2}}\right)$ in equation 4.13 distinguishes between a tube-like and a plate-like structures by assigning 0 for an ideal plate-like structure. Similarly, the second factor $\left(e^{-\frac{B^2}{2\beta^2}}\right)$ measures the deviation from a blob-like structure and is low for an ideal blob-like structure, and the third factor $\left(1 - e^{-\frac{C^2}{2c^2}}\right)$ is 0 for a plain background without any second order structure. A high product (ideally 1) of these three factors are desired for a tube-like structure. The parameters a, b,

and c are used to control the sensitivity of the vesselness measure to each of the ratios. The integration across each scale is done by selecting the highest product for a point at different scales, so that the overall vesselness measure gives an image with high probabilities for voxels lying on vessels of different diameters.

Figure 4.7 shows different branches of the right coronary artery (RCA) and the left artery extracted by using the Frangi's vesselness filter. The probability image obtained by applying equation 4.13 was thresholded to select high probabilities and using a seed point in the RCA region growing was used to select the connected components. For extracting different arteries, we used $a, b = 0.5$ and the $c = m + s$, where m is the mean, and s is the standard deviation of matrix C in equation 4.13. The integration of vesselness was done across 4 different scales with standard deviations of 1.5, 2.5, 3.5, and 4.5 voxels to accommodate the non uniform diameter of blood vessels along their length. The constant and scale values were empirically found to be good for extracting different vessels from our dataset.

4.3 Centerline Extraction

Finding the centerlines of blood vessels is a useful preprocessing step in applications involving the extraction of information from the vessels. For instance, a rough segmentation of the vessel can be obtained by applying a morphological dilation operation on the centerline. Automatic detection and quantification of plaque in vessels can be aided by knowing the distance of suspected plaque tissue from the centerline. In our case, we extract centerline from the contrast-enhanced CTA and study a morphologically dilated volume of voxels around the centerline. We also register the centerline to non-contrast-enhanced CT to study the corresponding volume of voxels and compare the calcium quantification in both the CT scans.

Although a centerline is an imaginary line and has not been defined explicitly, it may be considered as the medial axis for a simple tubular structure without any branch. The medial axis of a solid in 2-dimensional Euclidean space is defined as the union of the centers of all

(a)

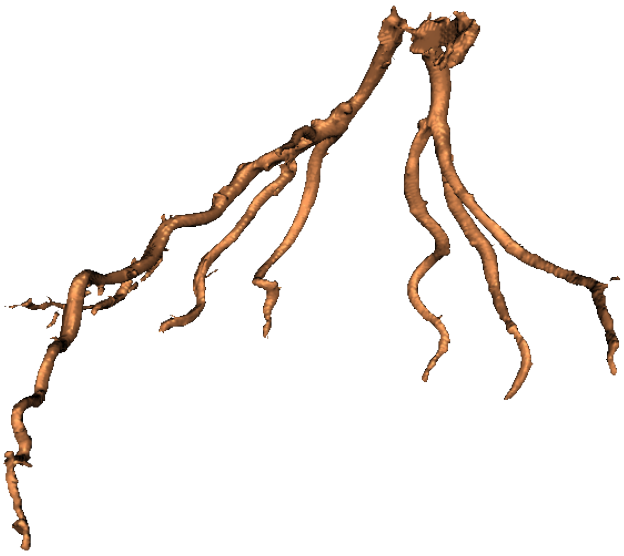

(b)

Figure 4.7 The right coronary artery (RCA) (a), and the left coronary artery (b) extracted by applying Frangi's vesselness filter, thresholding, selecting connected components, and smoothing.

maximal circles (spheres for 3-dimensional Euclidean space) inscribed by the solid [78, 79], where a circle is maximal if it is not contained in any other circle. In a tubular shaped structure with many branches or any other shape in general, the medial axis is also known as the skeleton of the shape . Hence, the centerline of a particular branch has to be isolated from the skeleton. Figure 4.8 shows the medial axis or the centerline of a simple tubular object plotted by connecting the centers of maximal circles inscribed by the vessel. For proper visualization, only a few circles are shown of actual numbers required to obtain a smooth centerline.

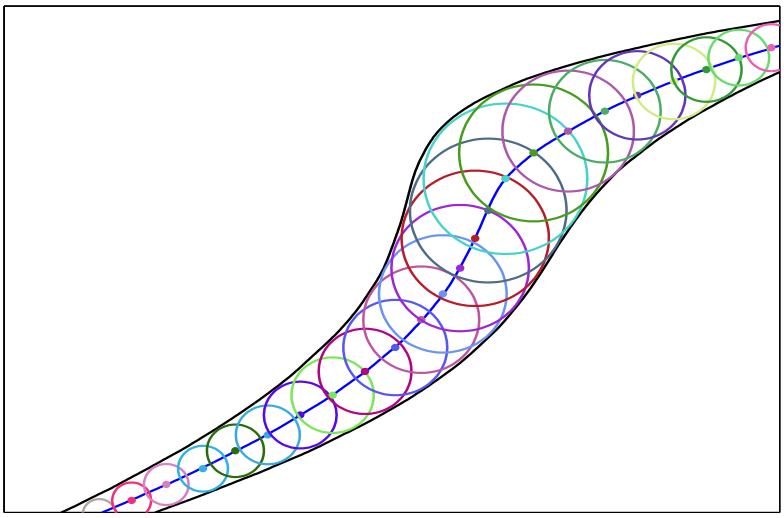

Figure 4.8 Centerline (blue) shown as a line formed by connecting a set of maximal circles inscribed by a 2D tubular structure (black). The centers of the circles are indicated with dots of the same color as the circles

Several approaches such as morphological thinning, distance transform, Voronoi tessellation etc. can be used for finding the medial axis of an object [80]. Among these, the distance transform is one of the popular and extensively studied methods. The distance transform of an image assigns each of its pixels the distance to the closest pixels in a given set. Different definitions of distance such as the Euclidean, L_1(Manhattan), L_∞(Chessboard), etc. [81] can be used . For the purpose of medial axis, Euclidean distance is considered and the distance transform of only the interior points from the boundary of the object is sufficient. Several computationally efficient algorithms exist for finding the distance transform. Jones et al.

have performed a comparative study of such algorithms in three dimensions based on their accuracy, ease of implementation, computational complexity and runtime performance [82]. Algorithms that used different distance functions such as the Chessboard, Euclidean etc. were considered for the comparison. A similar study by Fabri et al. compared 2-dimensional distance transform algorithms using the Euclidean distance function [83]. The algorithms by Meijster et al. [84] and Maurer et al. [85] are noteworthy as both of them are parallelizable, extensible to three dimensions and have a low computational complexity with small constants. The computation time for both of them are linear in terms of the total number of pixels, $O(N)$, where $N = i \times j$ for image with i rows and j columns, or $N = i \times j \times k$ for a three dimensional image with k slices. In parallel, both Meijster's and Maurer's algorithm have the complexity of $O(N/p)$, where p is the number of processors.

Figure 4.9 (a) shows a tubular object in two dimensions and 4.9 (b) is its distance transform calculated in its interior point. We used Maurers algorithm [85] for calculating the distance transform as it is fastest for the majority of images [83], and easily available as the MATLAB [86]routine `bwdist`. The distance transformed points are visualized as gray level image with the brighter pixels indicating higher distance from the boundary. As can be seen in the figure, the medial axis lies in the line of maximal distance from the boundaries of the object. A particular point on the medial axis lies at the highest curvature point in the intensity profile across the width of the vessel. This is shown in figure 4.9 (c) which is the intensity across the length of the red line shown in 4.9 (b).

As discussed in the previous section, second order derivative methods can be used to find the points of high curvature. Xia et al. have used the Laplacian and determinant of Hessian of distance transformed matrix to extract a point cloud which was then further localized to the medial axis by using morphological thinning algorithm [80]. Figure 4.9 (d) shows the Laplacian of the distance transform which localizes the centerline pretty well. Any pixel with intensity (c) such that $c < -\epsilon$ can then be used to isolate the centerline, where $-\epsilon$ is the threshold. The threshold in this case should be negative as the second order response is strong negative for a point of high positive curvature as shown in figure 4.5. The determinant

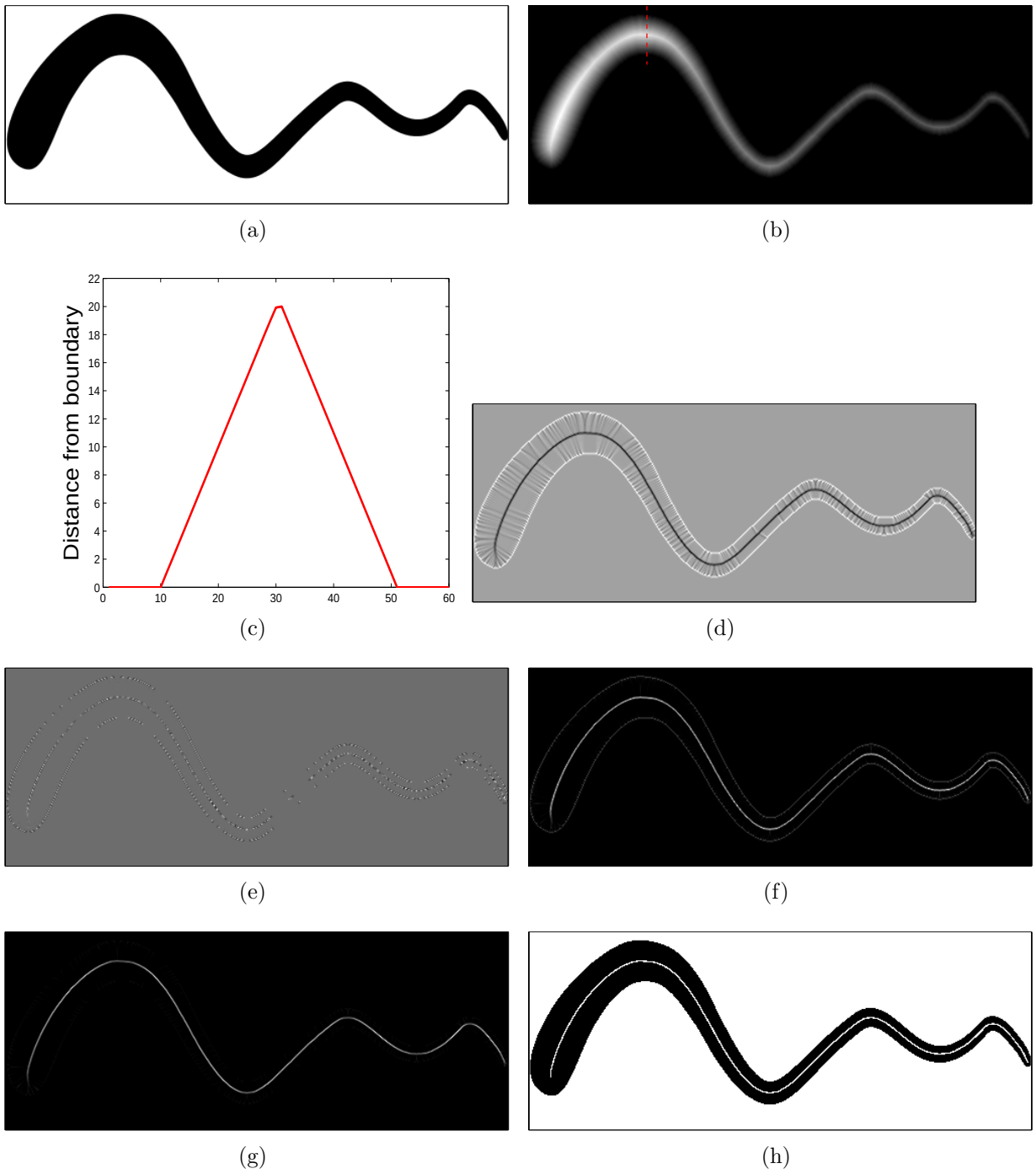

Figure 4.9 Distance transform of a 2D tubular object and different second order derivative based responses of the distance transform. (a) The 2D tubular object. (b) Distance transform in the interior of the object. (c) Profile of the Distance transform shown at the cross-section of the tube at the position indicated by the vertical red line in (b). (d) Laplacian of the distance transform. (e) Determinant of Hessian of distance transform. (f) Squared sum of the 2nd order partial derivatives. (g) Squared sum of the eigenvalues of the Hessian matrix. (h) Centerline extracted using a threshold of 0.5 and superimposed on the original image in (a).

of Hessian gives a sparse response to the centerline as shown in figure 4.9 (e). Figure, 4.9 (f) shows the response by using a different measure obtained by adding the squared sum the second order derivatives as follows,

$$S = \frac{\partial^2 I(\mathbf{x})}{\partial^2 x}^2 + \frac{\partial^2 I(\mathbf{x})}{\partial^2 y}^2, \tag{4.17}$$

where I is an image and $\frac{\partial}{\partial^2}$ is the second order partial differential operator. Equation 4.17 equation is similar to the equation 4.7, except for the fact that it uses the squared sum of the second order partial derivatives instead of simple sum in the calculation of Laplacian. Figure 4.9 (g) shows another measure by taking squared sum of eigenvalues of Hessian. It is clear from the picture that the squared sum of eigenvalues of Hessian gives better response to the centerline compared to all other second order based methods considered in this chapter. This is because the eigenvalues of Hessian directly gives the magnitude along the direction of highest second derivatives thus giving a stronger response to the highest curvature points than other points. The centerline can then be isolated by using a positive threshold. Figure 4.9 (h) shows the centerline extracted by using a threshold of 0.5 and superimposed upon the original image.

Applying threshold to the second order derivative responses may be sufficient for extracting centerline of a simple synthetic tubular structure as shown in figure 4.9. In a structure having multiple branches such as actual blood vessels such methods may be useful for finding the skeleton of the object. Since our objective is to study calcium in a particular branch, we need to isolate a desired branch from the skeleton. Ideally, the centerline algorithm should be able to isolate any particular branch from the skeleton. Preprocessing steps such as finding vessel like structures based on geometry or intensity as discussed in section 4.2 often results in broken vessels due to high noise or other anatomical conditions of the blood vessels such as stenosis. Therefore, extracting a connected centerline of a desired vessel requires further processing.

To select a particular branch, we need minimal user interaction such as selecting the start and end point of a desired branch. The centerline can then be found as the global minimum path from the start point to the end [87, 88, 89]. The minimal path may be found by using graph based algorithms in which the pixels are modeled as the graph nodes and some measure of similarity based on factors such as intensity, adjacency etc. can be used as the edge weight. The shortest path can then be solved by using technique such as Dijkstra's single-source shortest path algorithm [90]. The Dijkstra's algorithm updates the minimal cost of entering a node starting from the source node.

Another method that can be used for finding the global minimal path is based on propagating a wave front called the fast marching method [91]. Although the algorithm is similar to Dijkstra's algorithm, it considers the Euclidean distance from the source voxels and does not require the construction of graph from the image. The algorithm is derived by solving the equation of propagation of a wave front also know as Eikonal equation [91].

$$|\nabla T|F = 1, \tag{4.18}$$

where T is the time of arrival of the wave front and F is the speed function at different locations. The wave front propagates perpendicular to itself in the direction away from the source. The time of arrival of the front at each voxel location (x, y, z) is recorded to form the function $T(x, y, z)$. The front may propagate with different speed at different locations as indicated by the speed function $F(x, y, z)$. However, F should be positive in order for the wave to progress. Since the wave propagates from the source point, the time corresponding to the source point is zero. Hence, the minimal path can be found by tracing the shortest route from the end point to the source point. This can be achieved by using the optimization algorithm such as the gradient descent algorithm [72]. The gradient descent algorithm finds the global minimum of a function by stepping in gradient direction or the direction of maximum decrease of the function. Since the gradient direction is perpendicular

to the level set of a function, the traced path is perpendicular to the wave front at different time steps thus giving a shortest path to source point.

Since the fast-marching method depends on the speed function, it is important to have a speed function that will result in an accurate centerline. Figure 4.10 (a) shows a tube object with branches and figure 4.10 is the speed image constructed by setting a uniform speed all over the object. The speed is high in the interior of the object and close to zero outside the object. Figure 4.10 (c), (d) and (e) show the level set of the time function at different time instant. These are the wave front positions which originates from the end point of the desired centerline as indicated by the white circle. Since, the speed is high and uniform inside the object, the minimal or quickest path of the wave front corresponds to the shortest distance which is shown in figure 4.10 (f) with the source and end points shown by white circles. It is to be noted that the source point is the point from which the wave originates and the centerline is traced back from a desired point in the object back to the source point.

Therefore, the speed function should be higher toward the centerline and lower on the periphery so that the wave-front travels quickly through the centerline thus giving a centered response to the gradient descent algorithm. The distance transform of the object in its interior has the property that it is higher in center than toward the edges and can be used as a good speed function for the fast marching algorithm. Figure 4.11 (a) shows the distance transform of the branched tubular structure. Any zero values in the distance transform were replaced by a very low value (0.01 in this case) followed by normalization and squaring to increase contrast between higher and lower pixel values. The wave front position at increasing time instants are shown in figure 4.11 (b), (c), and (d). Figure 4.11 (e) shows the centerline traced through one of the branches and figure 4.11 (f) shows both the centerlines. For the second centerline, a new wave-front (which is not shown in the figures) was generated from the point indicated by the white circle in the lower branch.

The second order derivative response such as Laplacian, or the Hessian of the image can be used as a good speed function for the fast-marching method to extract the centerline

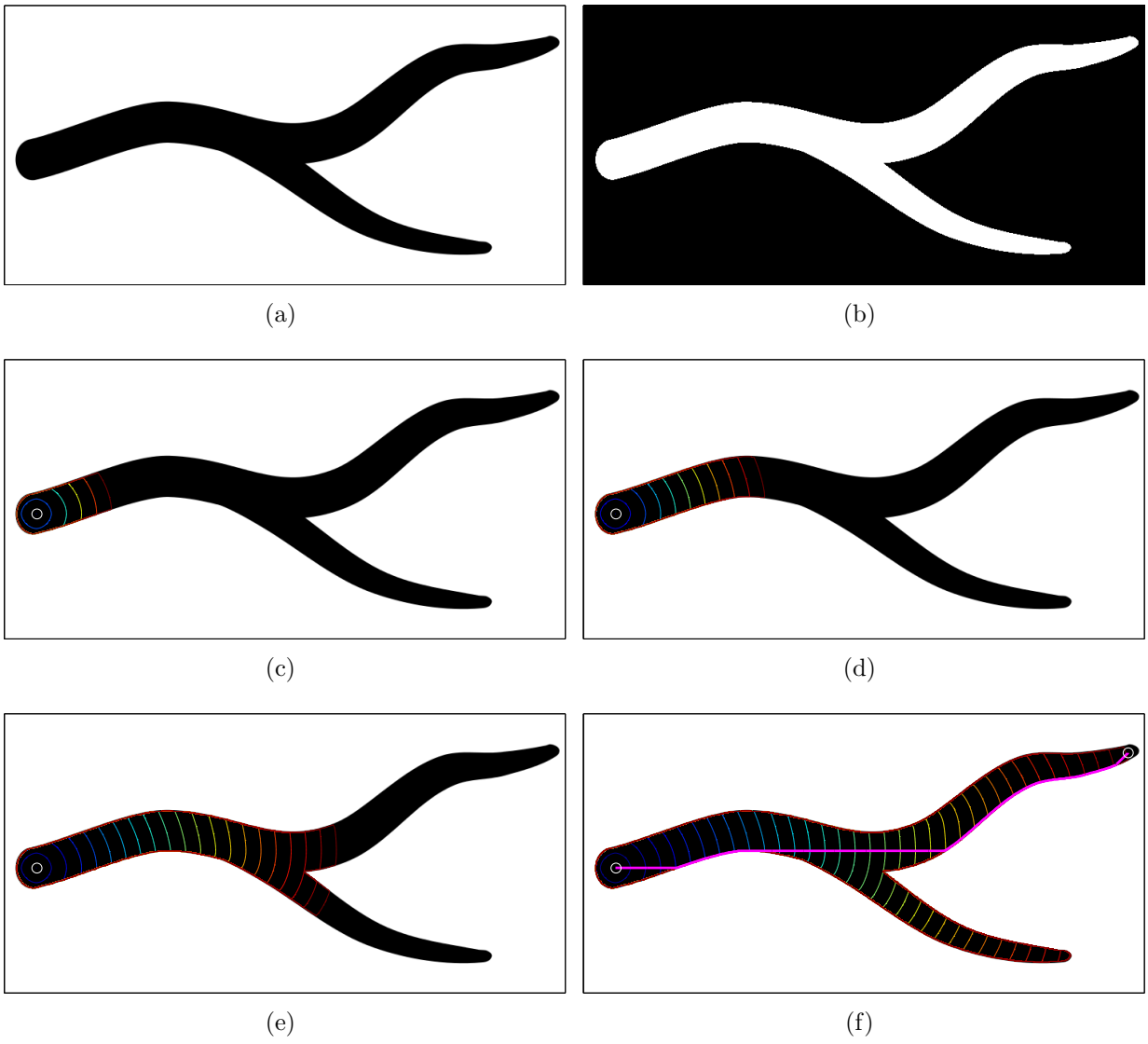

Figure 4.10 Propagation of a wave-front from a source point in a branched tubular object using a uniform speed function. (a) The tubular object with branches. (b) Speed image with uniform speed in the interior of the object. (c),(d),(e) Level set of the time of arrival of the wavefront at different time instant. The wave is propagated from the end point of the centerline of the desired branch as indicated by the white circle(f) The minimal path (pink line) for the uniform speed function which is not centered in the object.

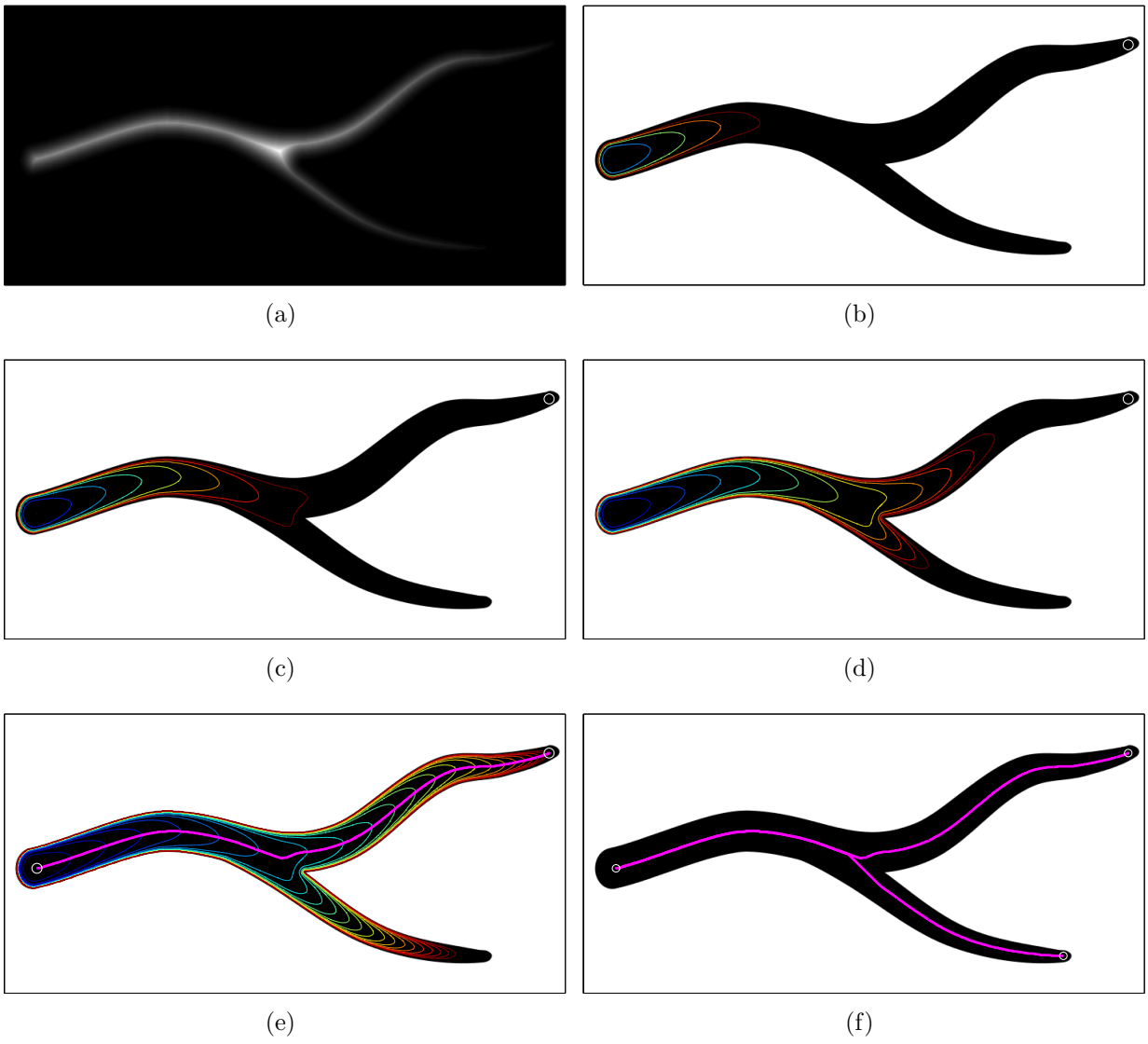

(a) (b)

(c) (d)

(e) (f)

Figure 4.11 Propagation of wave-front from a source point in a branched tubular object using a distance transform based speed function.(a) Speed function derived by normalization and squaring the distance transform of the object shown in figure 4.10 (a). (b),(c),(d) Level set of the time of arrival of the wavefront at different time instant. (e) Centered minimal path for the upper branch. (f) Centered minimal path for both the branches.

between the specified source and end points. In the next section, we compare different alternatives of the speed functions that can be used in the fast-marching algorithm.

The fast-marching method allows more flexibility compared to the Dijkstra's algorithm in a range of continuous problems such as robotic navigation [92]. The fast-marching method is also applicable to find the distance transform of an image by setting the object pixels in the image as source points and by using a uniform speed function, the arrival time of the front is proportional to the distance of the pixels from the source points. Both the fast-marching and Dijkstra's algorithm are popular choice for extracting the shortest path algorithm. Besides these minimal path extraction techniques, other approaches such as direct centerline tracking, model based extraction etc. have also been used. These methods may further be divided into automatic, semi-automatic, or interactive based on the level of interaction required to extract the complete centerline. Please refer to [93] for the review and [94] the evaluation of these methods.

4.3.1 Evaluation of speed functions for the fast marching method

As pointed out in the previous section, the fast marching method requires a speed function that has a higher values along the centerline as compared to the values toward the edges. In this section, we will see that highly localized speed functions such as the squared sum of eigenvalues of the Hessian produces accurate centerlines. Most of the speed functions we consider here are based on the second order derivatives of the distance transform as already discussed in the previous section.

Figure 4.12 shows the centerline of the two branches of the object for different speed functions. Figure 4.12 (a) uses the uniform speed in the interior of the object which does not produce a path centered to the object. Figure 4.12 (b) uses the distance transform, figure 4.12 (c) uses the Laplacian or the divergence of gradient of the distance transform, figure 4.12 (d) uses the squared sum of second order derivatives of the distance transform, figure 4.12 (e) uses the squared sum of the eigenvalues of the Hessian matrix of the distance transform, and figure 4.12 (f) uses the logarithm of inverse magnitude of the Gradient Vector

Flow (GVF) [95] as speed functions for calculating the centerline.

The gradient vector flow (GVF) algorithm was primarily developed as an external force field for image segmentation by using an active contour model. In such models an initial contour known as a snake [57] is iteratively guided toward the desired image features such as edges by an external force field and the contour itself is kept smooth by its internal force. The external force field is the gradient or the vector of the partial derivatives of the edge written as $\nabla G_\sigma * I$, where G_σ is the Gaussian kernel with a standard deviation of σ used for smoothing the image I. Edge found by using standard edge detector such as Canny may also be used in place of the image I for edge localization. The smoothing may be done at multiple scale spaces by choosing higher σ to extend the force field required to pull the snake toward the edges. However, the smoothing also blurs the edges and may even fuse small structures lying close [96].

The GVF algorithm [95] diffuses the edge gradient to homogeneous region by minimizing the following energy functional,

$$E = \int\int \mu\nabla^2\mathbf{v} + |\nabla\mathbf{f}|^2|\mathbf{v} - \nabla f|^2 dxdy, \tag{4.19}$$

where $\mathbf{v}(x, y) = [u(x, y), v(x, y)]$ is the gradient vector flow field, $\nabla\mathbf{f}$ is the gradient of the edge, ∇^2 is the Laplacian operator or $\frac{\partial^2}{\partial x^2}, \frac{\partial^2}{\partial y^2}$. The above equation can be solved iteratively as discussed in [95] to find the vector $\mathbf{v}$. The GVF of an object has also been used for finding centerline [96] by applying a vesselness filter [76] on the response. The vectors produced by GVF algorithm are directed toward the boundary of the object and have minimal response in the center. We used the magnitude of gradient of the image object to find the edge map as shown in figure 4.13 (a) and then applied the GVF algorithm. To maximize the response in center we inverted the normalized magnitude of the GVF response and took its logarithm. The speed function by using GVF is shown in figure 4.13 (b).

As seen in figure 4.12 (a) the uniform speed function is unacceptable for finding the centerline, and figure 4.12 (f) shows that the GVF based speed function produces a path that is not centered to the object. Speed functions based on distance transform and its

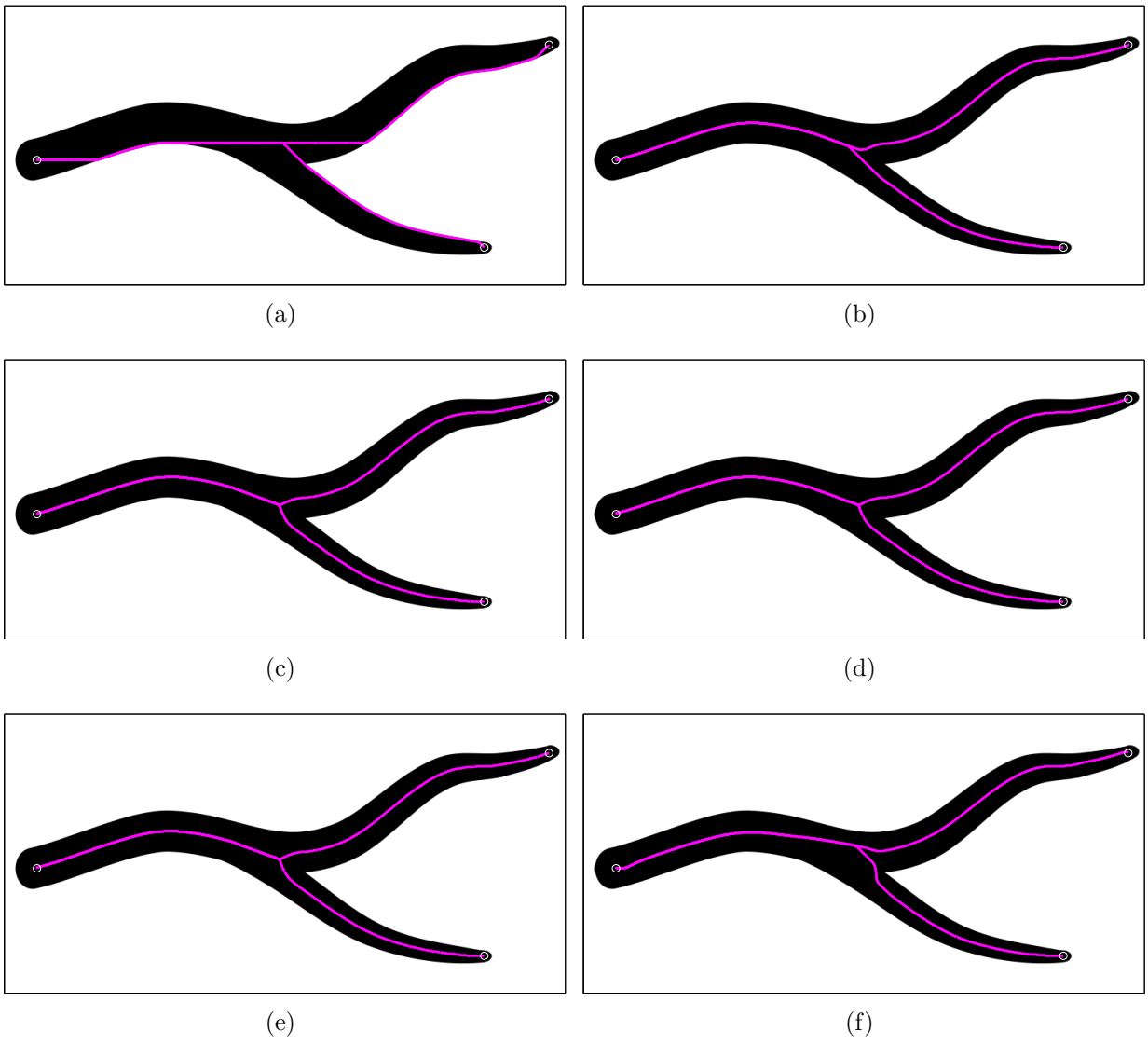

Figure 4.12 Centerline traced by using the fast-marching method with different speed functions. (a) Uniform, (b) distance transform,(c) Laplacian of the distance transform, (d) squared magnitude of the second order derivatives of the distance transform, (e) squared magnitude of eigenvalues of Hessian of the distance transform, and (f) gradient vector flow (GVF) of edge map speed functions.

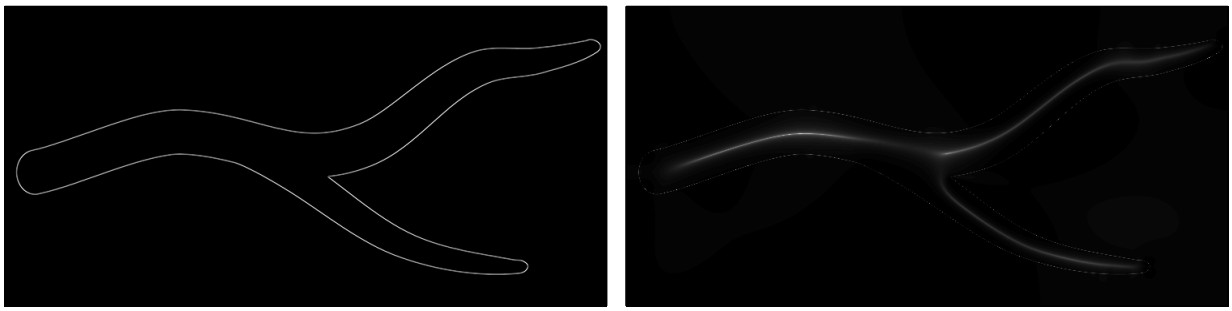

(a) (b)

Figure 4.13 Gradient vector flow based speed function. (a) Magnitude of the gradient vectors of the original image used as the edge map for calculating the gradient vector flow speed function. (b) Gradient vector flow derived from the edge map used as a speed function for the fast marching method.

second order derivatives produce centered path when used with the fast marching as shown in figure 4.12 (b),(c),(d), and (e).

We compared these further based on the consistency of response when the source point for generating wave front are changed. Figure 4.14 shows skeleton of an object created by combining centerlines of the object from one end point to the other. We used the fast marching method for generating the centerline, for which three points marked 1, 2 and 3 were used as sources separately. The red, green, and yellow lines are the skeleton generated by using points 1, 2, and 3 as source points respectively. Ideally all three skeletons should completely overlap with each other for producing localized and accurate centerlines. The distance transform speed function is not localized to the centerline and hence the skeleton are wide apart from each other as shown in figure 4.14 (a). Based on the overlap of the centerlines, the GVF based speed function shown in figure 4.14 (b) is better than the distance transform but still has wide separation in the center of the object. Figure 4.14 (c), (d), and (e) show the skeletons by using Laplacian of the distance transform, the squared sum of the second order derivative, and squared sum of eigenvalues of Hessian of the distance transform respectively. The latter three are all acceptable for tracing centerline with the last two slightly better than the Laplacian response. Although the squared sum of derivatives and the squared sum of eigenvalues of Hessian based skeletons are virtually indistinguishable, the

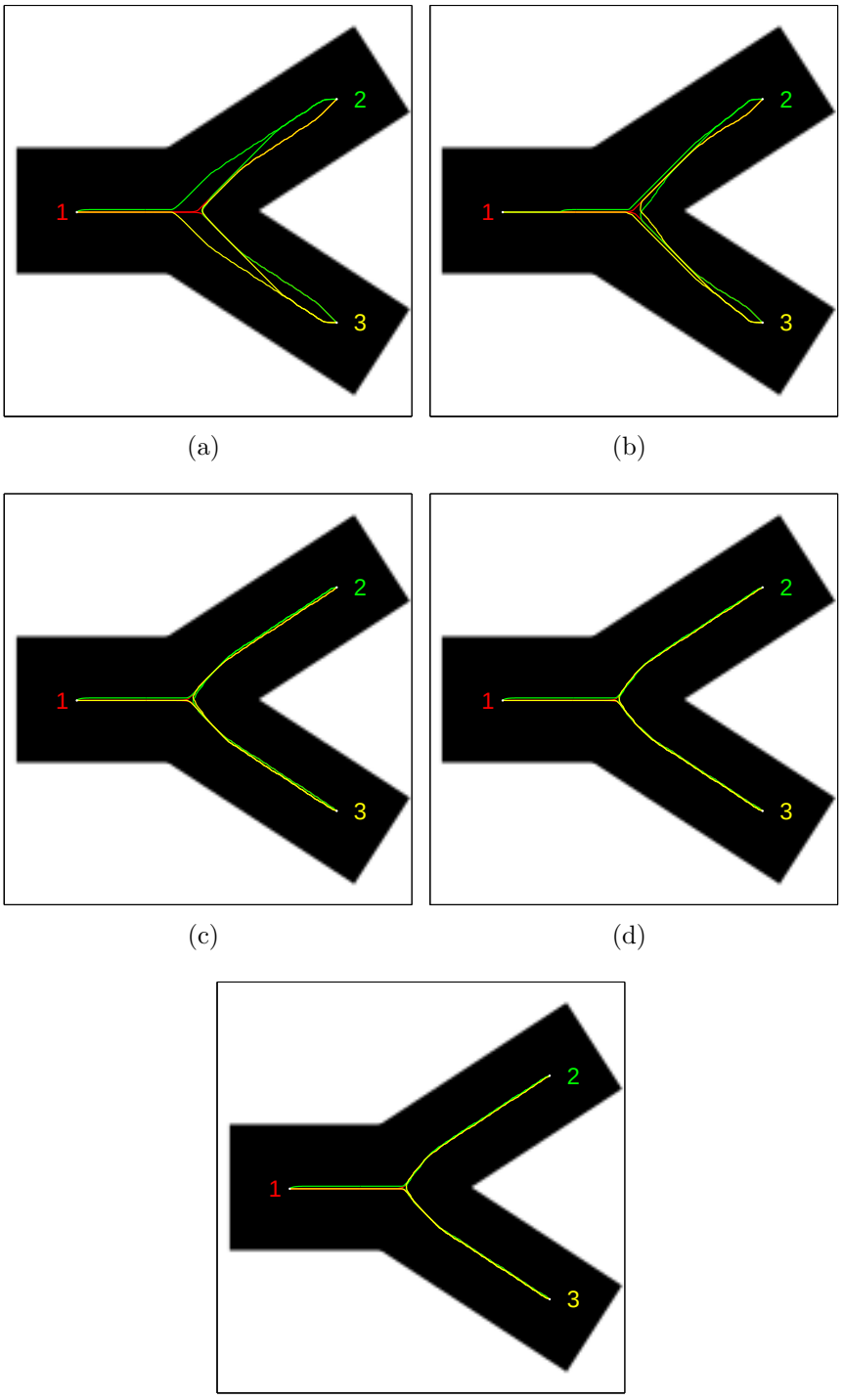

Figure 4.14 Consistency of skeletons of an object found by using the fast-marching method with different source points and speed functions. Three different points, 1, 2 and 3 are separately used as the source of the wavefront. Red skeleton corresponds to source point 1, green for source point 2 and yellow for source point 3. The skeletons found by using (a) distance transform, (b) gradient vector flow, (c) squared sum of second order derivatives of the distance transform, (d) Laplacian of the distance transform, and (e), squared sum of the eigenvalues of Hessian of the distance transform as speed functions.

Hessian based response is highly localized to centerline with minimal response to the edge as seen in figure 4.9(f) and (g). This is also shown in figure 4.15 where the squared sum of second derivatives has high response for edges as well as centerline so that an outline of the object can be traced whereas the Hessian based output has very low response for the edges.

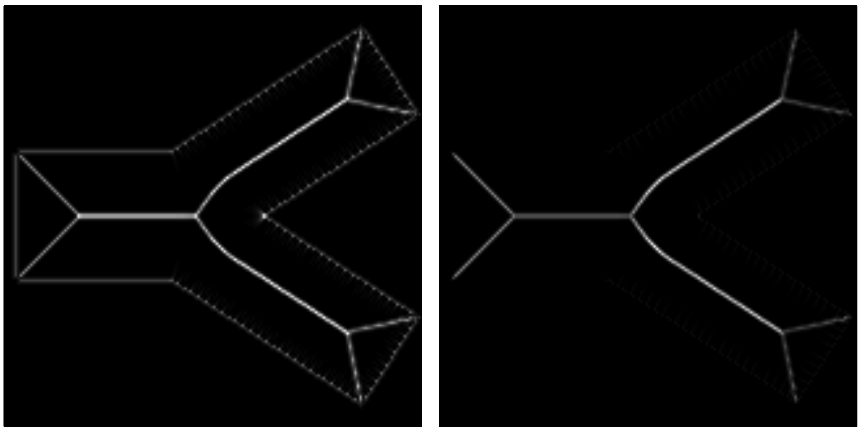

(a) (b)

Figure 4.15 Squared sum of second derivatives of the distance transform of a 2D object. (a) The squared sum of second derivatives in the x and y directions (b) Squared sum of the eigenvalues of the Hessian.

As already discussed in the previous section since the eigenvalues of the Hessian give the highest second order derivatives in directions orthogonal to each other, the square sum of these values gives highest response to high curvature points. As the distance transform of an object has the highest curvature points along the medial axis, the squared sum of eigenvalue of Hessian provides very localized response to the medial axis. Furthermore, it was also seen in this section that the edge response of the Hessian was lower than that for the squared sum of the second order directional derivatives in the x and y direction. Therefore the squared sum of eigenvalues of Hessian can directly be used to extract centerline by using a thresholding step. Therefore, for extracting centerline of a particular branch it is an excellent preprocessing step.

4.4 Summary of centerline algorithm

Our centerline algorithm begins first by extracting vessels from the 3D volume of CT image. For extracting the blood vessels we use eigenvalues of the Hessian matrix. The eigenvalues calculated from multiple scales are combined in a way suggested by Frangi et al. [76] to find blood vessels of different diameters. The vessel extraction process results in 3D binary volumes of different blood vessels. Centerline of a desired branch is found by using the fast marching method [91]. In this method, a wave-front is generated from a source and the centerline is traced by finding the path through which the wave travels fastest. A speed function which defines the speed of the wave at each location is required to propagate the wave front from its source. The speed function should be higher in a narrow localized region in the center so that the wave travels fastest there and the global minimum path with lowest time function from a point to the source of the wave is the centerline of the object. The distance transform and its second order derivative based responses of a binary object provide good speed functions. The squared sum of eigenvalues of Hessian of the distance transform in particular was found to provide a very localized response to the centerline. If extracting the skeleton of an image is the final goal, applying a threshold to the Hessian based response is enough. To extract a centerline, the Hessian based response can be used as a preprocessing step to calculate the speed function or cost function for other methods such as Dijkstra's shortest path method [90].

The automatic blood vessel and centerline extraction method can be summarized in the following steps.

`Step 1.` `Extract Tube like structures.`

`Step 2.` `Threshold and select connected components.`

`Step 3.` `Find a centered response of the binary volume resulting form step 2.`

`Step 4.` `Find the centerline.`

In `step 1`, a three dimensional subvolume of interest is extracted manually from the CTA volume and then the Hessian matrix is calculated for each voxel in the subvolume as

shown by equation 4.3. Eigenvalue decomposition of Hessian yields three eigenvalues for each voxel which are then used to find the probability that each voxel is part of a vessel by using the Frangi's vesselness measure or the equation 4.13. In `step 2`, the probability matrix obtained form step 1 is thresholded to select only the high probability voxels and a desired connected component is selected on the resulting binary volume by using a manually clicked seed point. Figure 4.7 shows the resulting blood vessels after the first 2 steps. In `step 3`, first we find the distance transform in the interior of the binary volume. The distance transform itself is a centered response with high values in the center (figure 4.9 (b)). However, it is difficult to isolate the skeleton of the object by thresholding the distance transform, and its use as a speed function does not provide optimal centerline (figure 4.14). Therefore, we calculate square sum of eigenvalues of the Hessian of the distance transform. Precise skeleton of the object can be isolated by using a single thresholding step to the Hessian and it can also be used as a very good speed function for finding the centerline (figure 4.14). Finally in `step 4`, we manually select the start and end points of the vessel of interest. Then using the centered response of `step 3` as the speed function, the fast marching method [91] is used to find the centerline segment between the manually selected points.

4.5 Conclusion

In this chapter we experimented with different methods to automatically reconstruct coronary arteries from the contrast-enhanced computed tomography angiography (CTA). The reconstruction process included automatic vessel segmentation and centerline extraction using minimal user interactions such as manually marking start and end points of the artery. We found that a threshold based segmentation was not sufficient for accurate segmentation of the arteries, so used geometry based segmentation by analyzing the eigenvalues of second order partial derivatives of the CTA volume. We also found that the squared sum of eigenvalues of Hessian of the distance transform gave a very localized response to the medial axis of an object and hence a simple thresholding step is sufficient for extracting the geometric skeleton of an object. The squared sum of second ordered partial derivatives

of the distance transform provided similar response as the Hessian based method and both proved to be good preprocessing steps for isolating a desired centerline path of an object by using methods such as fast marching method, Dijkstra's shortest path algorithm etc.

The geometry based segmentation used in this chapter cannot distinguish between the lumen and calcification in the vessels. Therefore, we used the centerline extracted in this chapter as a preprocessing step for more accurate segmentation and calcium quantification as discussed in the next chapter.

CHAPTER 5

METHODOLOGIES FOR CALCIUM QUANTIFICATION IN COMPUTED TOMOGRAPHY ANGIOGRAPHY (CTA)

5.1 Introduction

Calcification in arteries occur within the vessel wall which is in close proximity to the vessel lumen. The cutoff threshold of 130 HU used in conventional calcium quantification in non-contrast-enhanced CT scan may not be useful for calcium quantification in contrast-enhanced CTA since the contrast agent administered to a patient during CTA exceeds 130 HU. As a result the intensity profiles of contrast-filled lumen and the calcium largely overlap making it difficult to separate calcium by a fixed threshold. Many attempts have been made to identify the calcium by using higher thresholds such as 320 HU [17], 350 HU [21, 22] or even 600 HU [23], based on the assumption that by selecting a sufficiently large cutoff threshold, the high density calcium can be separated from the contrast filled lumen. Calcium quantification using fixed cutoff threshold may be inaccurate as there is a chance of inclusion of lumen resulting in overestimation of calcium or exclusion of low density calcium resulting in underestimation of calcium.

The overestimation or the underestimation of the calcium quantification can result in classification of a patient into different risk category which is known as restratification. Patients are classified into different risk categories based the coronary artery calcium (CAC) score. The screening for heart attack prevention and education task force recommends to classify a person to be in the low or moderate risk category if the CAC score is 0, moderately high risk category if $0 <$ CAC score < 100, and $< 75^{th}$ percentile of the particular age group and gender, high risk category if $100 \leq$ CAC score < 400 or $> 75^{th}$ percentile, very high risk category if CAC score > 100 and $> 90^{th}$ percentile, or if the CAC score ≥ 400 [97]. Different treatment plans are recommended according to the risk category of a patient; a patient in

higher risk group requires more aggressive lifestyle modifications than the one in lower risk group [97]. Therefore, the restratification of a patient due to error in calcium quantification is undesirable and can be hazardous.

To remove the drawbacks of a fixed threshold based calcium quantification in CTA, cutoff thresholds have been calculated adaptively based on the intensity profile of contrast-filled lumen [18, 19]. Although adaptive threshold calculation addresses the variation of cutoff threshold across different CTA dataset, these methods do not separate the voxels that are in the overlapped region of the intensity profile. If we were to consider the conventional cutoff threshold of 130 HU to identify calcium, then the voxels in the range 130 HU to the minimum attenuation of the contrast material in the lumen is the overlapped region, where the voxel can either be a calcium or a lumen. Since calcification occurs in the arterial wall, the location of the voxel with respect to the lumen may provide a clue to whether the voxel is calcium or not.

A number of methods have been developed to segment the arterial wall in order to quantify different plaque components within the wall. While it is easy to segment the lumen in CTA based on the intensity profile alone, segmenting the outer arterial wall is a difficult task because of the low contrast or even absence of contrast between the arterial wall and surrounding tissue. The segmentation of arterial wall has been performed in larger arteries such as carotid arteries [44, 48, 50]. Although a high correlation coefficient with manually quantified plaque components were reported, the correlation coefficient alone may not be sufficient for assessing the accuracy. Usually low difference range of the quantification is desired in order to avoid the reassignment of a patient to different risk stratification. There is a high chance of underestimation or overestimation of calcium quantified by these methods as the accuracy is highly dependent on the accurate segmentation. These methods may not be useful for smaller coronary arteries which have low resolution in the CTA and it is difficult to delineate the outer contour of the arterial wall.

In this chapter we describe the methods to accurately quantify calcium from the contrast-enhanced CTA. The novelty of our algorithm are the use of expectation maximiza-

tion algorithm to estimate the total amount of calcium in the overlapped intensity range, combining this information to the spatial feature based calcium classification in the mixed intensity range and estimating cutoff threshold to separate high density calcium from the calcium in overlapped intensity range.

5.2 Methodologies

Our method first extracts the blood vessels and the centerline. Then the centerline is morphologically dilated possibly including some of the myocardial tissue or part of the lungs. From the lengthwise plot of intensity, an adaptive cutoff threshold is developed to separate the high-density calcium. Based on the probability of the contrast in the non-calcified region, we then calculate the probability of contrast and hence the low-density calcium in the calcified regions. The dilated voxels are also used to obtain segmentation of the lumen and the surrounding tissues by using expectation maximization algorithm as will be explained in Chapter 7. The methodology to quantify calcium from the CTA are discussed in the following subsections.

5.2.1 Centerline extraction

The centerline extraction as discussed in chapter 4 begins with the geometric based automatic extraction of the arteries by using the eigenvalues of the second order derivative matrix, also known as the Hessian matrix. The output of this step is a probability volume which is then thresholded to select high-probability tubes followed by connected component analysis to select a desired artery such as the right or the left coronary artery. The result is a binary volume with connected tubular branches. To find the 3D centerline, first the distance transform of the binary tubular structure is obtained. Then, obtain the squared sum of the eigenvalues of the Hessian matrix of the distance transformed volume. This response so obtained can directly be used as the skeleton of tubular structure after a simple thresholding step. If a centerline of a particular branch is desired as in our case it can be isolated by using the eigenvalue based response of the distance transform as a speed or cost function for

methods such as fast marching method [91] or Dijkstra's shortest path algorithm [90] to find the shortest path between desired points in the artery.

5.2.2 Morphological dilation of the centerline

In this step we morphologically dilate [58] the isolated centerline to cover the entire arterial wall and possibly some surrounding tissue. The dilation can by done by using a 3 dimensional structural element such as a sphere or a cylinder. The radius can be decided empirically. For example, in chapter 3 we used a spherical structural element of radius 7 voxels to dilate the centerline. The dilation step is necessary to include the arterial wall since the outer wall of the artery is hard to detect in the CTA because of very low or no contrast with the surrounding tissue. This can be seen in the figure 5.1 (a) and (b) where the outer wall of the arteries can be seen only due to the calcium present on it otherwise the outer wall cannot be distinguished from the surrounding tissue.

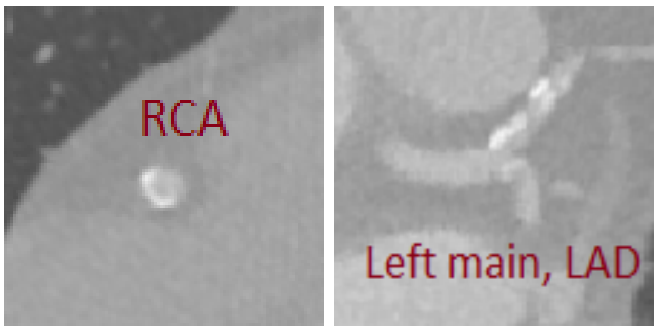

(a) RCA (b) LAD

Figure 5.1 A slice of contrast-enhanced CTA with (a) cross section of the right coronary artery (RCA) and (b) left main along with the left anterior descending (LAD) branch.

5.2.3 Probability density estimate of the voxels

We quantify the total calcium based on the absolute intensity cutoff as well as the probability of calcium in a range of intensities. The absolute cutoff threshold is the HU intensity above which the voxels are only calcium. There is a range of intensities below the cutoff where the voxels can either be contrast or calcium. The absolute cutoff as well as the

mixed range of intensities can be different for different patient as well as along the length of the individual arteries.

In order to find the absolute cutoff threshold, first we find the normalized intensity profile of the dilated artery as shown in figure 5.2 which is calculated by finding the frequency or the total number voxels of each observed HU intensity and dividing by the sum of the frequency. The horizontal axis show occurrence of different intensity level and the height of each vertical line is the normalized frequency of these levels. The total number of intensity levels in the horizontal axis was made sparse by subsampling for proper display in the figure. The artery was obtained by dilating the automatically extracted centerline as described in chapter 4. The normalized profile which sums to 1 as required by the next step is also known as the probability density function (PDF) of the data.

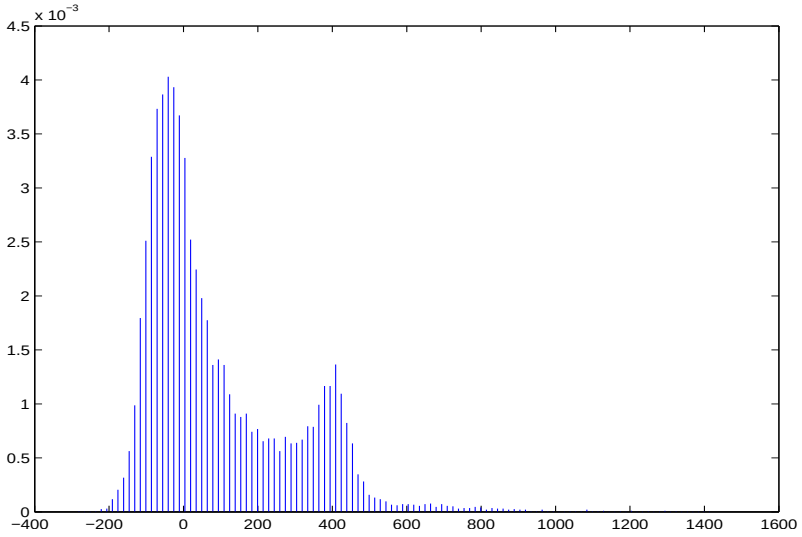

Figure 5.2 Normalized intensity profile of the segmented and dilated artery from the contrast-enhanced CTA of a diseased patient.

The voxels belonging to different tissue types such as contrast, arterial tissue, and calcium can be separated by resolving different PDFs corresponding to these tissues. The PDF of the dilated artery can be expressed as the mixture of different underlying components, one for each tissue type. Figure 5.3 shows a PDF generated (solid line) as the weighted sum of two Gaussian (broken lines) with weights 3 and 2. Resolving two components is the reverse

of idea expressed in figure 5.3 since we have to start with a given PDF and estimate two components and the corresponding weights. Chapter 7 explains the algorithm in details.

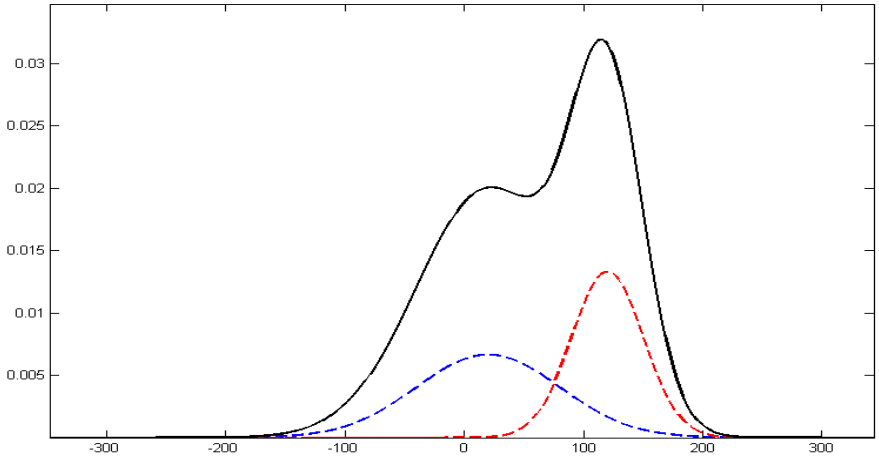

Figure 5.3 A probability density function (solid line) obtained as the weighted sum of two Gaussian (broken lines) with weights 3 and 2.

In this approach we need to make assumption on the number of tissue components and the model of the PDF of these components. Since the amount of calcium is variable and may be much less than the contrast material, the calcium component may not always be resolved with accuracy. Therefore we use non-parametric model to estimate the PDF of the dilated artery by using an approach called Parzen window [98] method. A non-parametric density estimate technique attempts to approximate a PDF from empirical or observed set of data without making any assumption on the model of the PDF or its underlying components. Therefore the resulting PDF can be arbitrarily shaped but approximates the empirical data.

The Parzen window approach is a data interpolation technique [99] that estimates a continuous probability density functions of the voxel intensities by a smoothed or average version of the intensity distribution. If $X = \{x_1, x_2, ..., x_N\}$ is a set of the observed HU arterial intensities in the CTA, then the Parzen window estimate of the shape of its PDF is given by,

$$p(x) = \frac{1}{nh} \sum_{i=1}^{N} K\left(\frac{x_i - x}{h}\right), \tag{5.1}$$

where, $p(x)$ is the probability estimated for each point $x \in X$. $K\left(\frac{x_i - x}{h}\right)$ is known as the window or kernel function which should satisfy the constraints that it is non negative and should integrate to 1 for the resulting function to be a density estimate [99]. Different window functions such as triangular, uniform, Laplacian, Gaussian, etc. can be used. Let us use a Gaussian kernel defined as,

$$K(x) = \frac{1}{\sqrt{2\pi}} e^{(-\frac{x^2}{2})}, \tag{5.2}$$

which is non-negative, centered at 0, has a unit standard deviation, and integrates to 1. A Gaussian kernel is centered at each data point, so that it acts as a probability density estimate of a single data point. Then the density estimate of the observed data is obtained by taking the average of all the kernels at each point. The bandwidth h of equation acts as the standard deviation σ of the Gaussian Kernel to control its width. Hence the density estimate for each data point $x \in X$ can be expressed as,

$$p(x) = \frac{1}{n\sigma\sqrt{2\pi}} \sum_{i=1}^{N} e\left(-\frac{x_i - x^2}{2\sigma^2}\right). \tag{5.3}$$

Equation 5.3 is applied for each data point to obtain the shape of the density estimate. Figure 5.4 (a) show the Parzen window density estimate by using the Gaussian kernels. The red vertical lines are the normalized observed data with taller lines representing higher frequency than the shorter ones, the dotted curves are the normalized Gaussian kernels centered at each data location, and the solid black line is the average of the kernels at each point or the final probability density estimate of the observed data.

The bandwidth or the standard deviation of the Gaussian kernel in this case is an important parameter, since it creates a trade-off between the resolution and variation of data. Selection of a high bandwidth leads to oversmoothing or low resolution while a low bandwidth

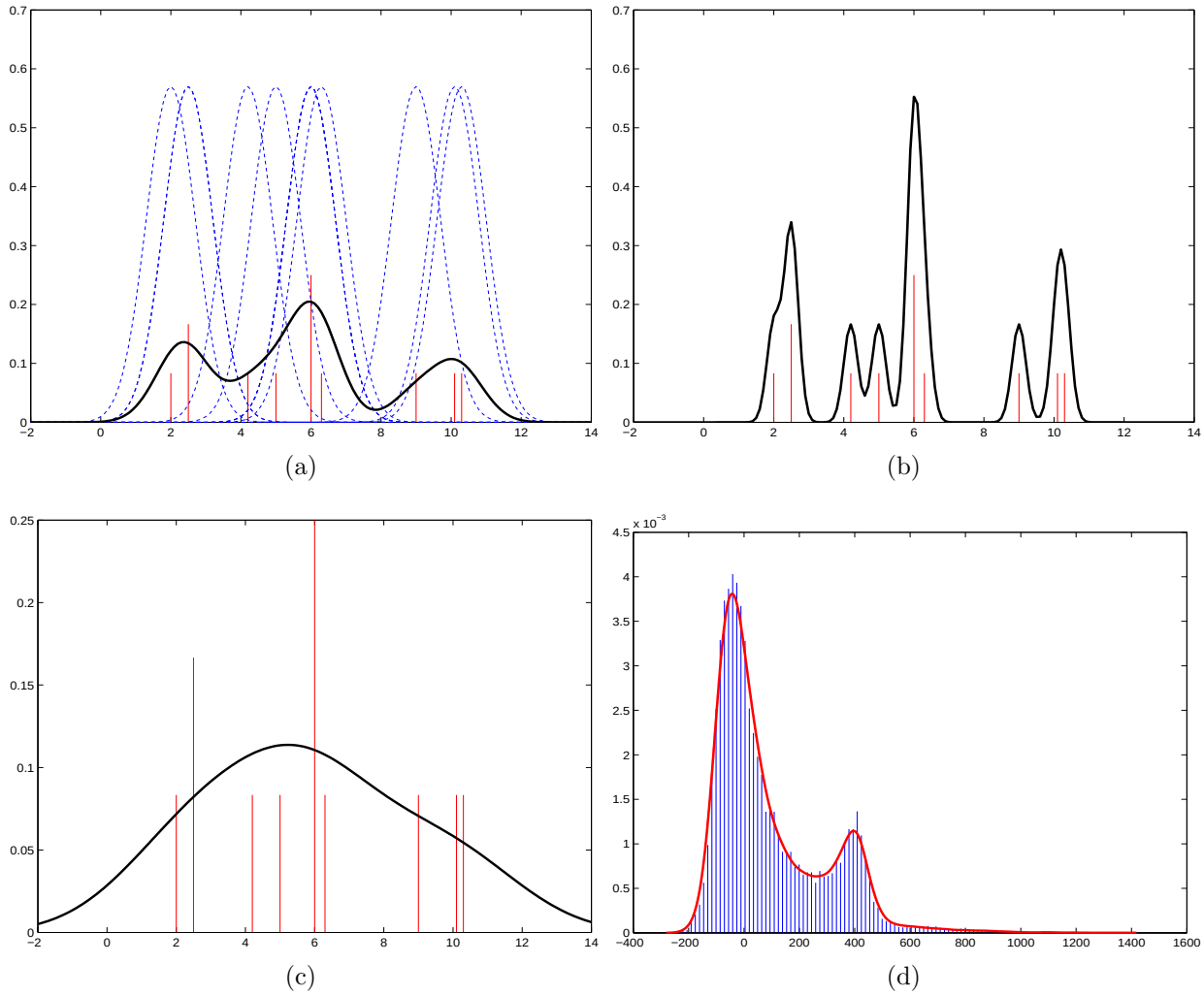

Figure 5.4 Probability density estimation using the Parzen window with Gaussian kernels of different bandwidths.(a) Gaussian kernel of 0.7 standard deviation (bandwidth) (b) Undersmoothing due to low bandwidth of 0.2, (c) Oversmoothing due to high bandwidth of 2.0. (d) Application of the Parzen window method with automatic bandwidth selection to estimate the probability density function (PDF) of the artery voxel intensities. The density estimate is shown in red curve and the vertical lines are the normalized intensity profile.

leads to undersmoothing or a high spatial variation of the density estimate. Figure 5.4 (b) shows the undersmoothing due to Gaussian kernel of 0.2 standard deviation and figure 5.4 (c) shows oversmoothing due to higher standard deviation of 2.0. Although figure 5.4 (a) with standard deviation seems to be optimal in this case, the optimal choice of parameter is specific to different data-sets. Different automatic methods have been developed for selecting the bandwidth [100, 101, 102] . A review of the automated methods are presented in a survey by Marron et al. [103] and a more recent one by Heidenreich et al. [104]. In our work we used an improved version of Sheater and Jones's method [100] of bandwidth selection and is based on observed data without the requirement of any assumption on the model of the data unlike the previous methods [102]. The kernel density estimate of the artery voxel intensities is shown in figure 5.4 (d), where the red curve is the density estimate of the normalized intensity profile shown by the vertical lines.

5.2.4 Finding a cutoff threshold for high-density calcium

Conventionally, a cutoff threshold of 130 HU is used to quantify calcium in non-contrast enhanced CT. In chapter 3 we showed a better quantification is possible by using a higher threshold in 0.5 mm slice thickness CT reconstruction. In a contrast-enhanced CTA volume, the contrast-filled lumen achieves higher intensity range which overlaps with the intensity profile of the calcium. To account for the increase of the intensity many studies have elevated the cutoff threshold to 320 HU [17], 350 HU [21, 22] and even 600 HU [23]. A single cutoff threshold, however is not optimal for different CT volumes as the intensity range for contrast depends on factors such as contrast concentration, patient physiology, contrast injection rate, time elapsed since contrast administration, image noise etc. [24]. Therefore, these studies either resulted in underestimation [21, 23, 17] or overestimation [22] of calcium.

To isolate the high-density calcium, we introduce an adaptive cutoff threshold which takes into account the variability of contrast range along the length of the arteries. Our algorithm first calculates the intensity profile and estimates a probability density function using Parzen window method as described in section 5.2.3. Figure 5.4 (d) shows the estimated

probability density function in an artery. The same PDF has been replicated in figure 5.5 (a) but without the vertical lines for the observed voxel intensities. The high density calcium have the highest intensity range in an artery and their frequency is less than that of contrast voxels. Therefore the calcium intensity appears as a long shallow tail toward the right of the PDF. The shallow tail of calcium can be separated by calculating the first derivative of the PDF to find the right-most point at which the PDF has required amount of flatness. In other words, we need to find the right-most point in the PDF where the squared magnitude of its derivative exceeds a small threshold $> \epsilon$. From the CTA dataset we empirically decided ϵ value of $0.2 \times P$, where P is the peak square magnitude of the first derivative provided a good cutoff threshold for estimating the high density calcium.

Figure 5.5 (b) shows the squared magnitude of the derivative scaled to a peak value of 100. The red circles are the points at which the magnitude exceeds the required ϵ value for flatness. Only few of these points are shown in the picture for clarity. Since we are interested in the right-most flat region, we select the right-most circle position as the cutoff threshold. The corresponding point is shown by an cross in figure 5.5 (a).

This phase of our algorithm used to find high-density calcium cutoff from the flat region on the right of histogram is similar to the algorithm described by Teßmann et al. [18]. Our algorithm differs in that it smooths the probability density function by using Parzen-window with Gaussian kernel and calculates the ϵ value relative to the peak magnitude of the derivative in each CTA volume. This provided for better probability density and cutoff estimation than the box-filter and fixed ϵ value used in [18]. Although, Teßmann et al. considered inter-patient variability in contrast intensity range, they did not take into account the variability in contrast range along the length of the artery which should be considered for an accurate quantification of calcium in a CTA volume.

We observed that the contrast range differs not only across different CTA but also along the length of a single artery thus posing more difficulty in accurate quantification of calcium. This could be due to the high absorption of the contrast material toward the distal ends of the artery so that the intensity range slightly narrows down toward the distal end of an artery.

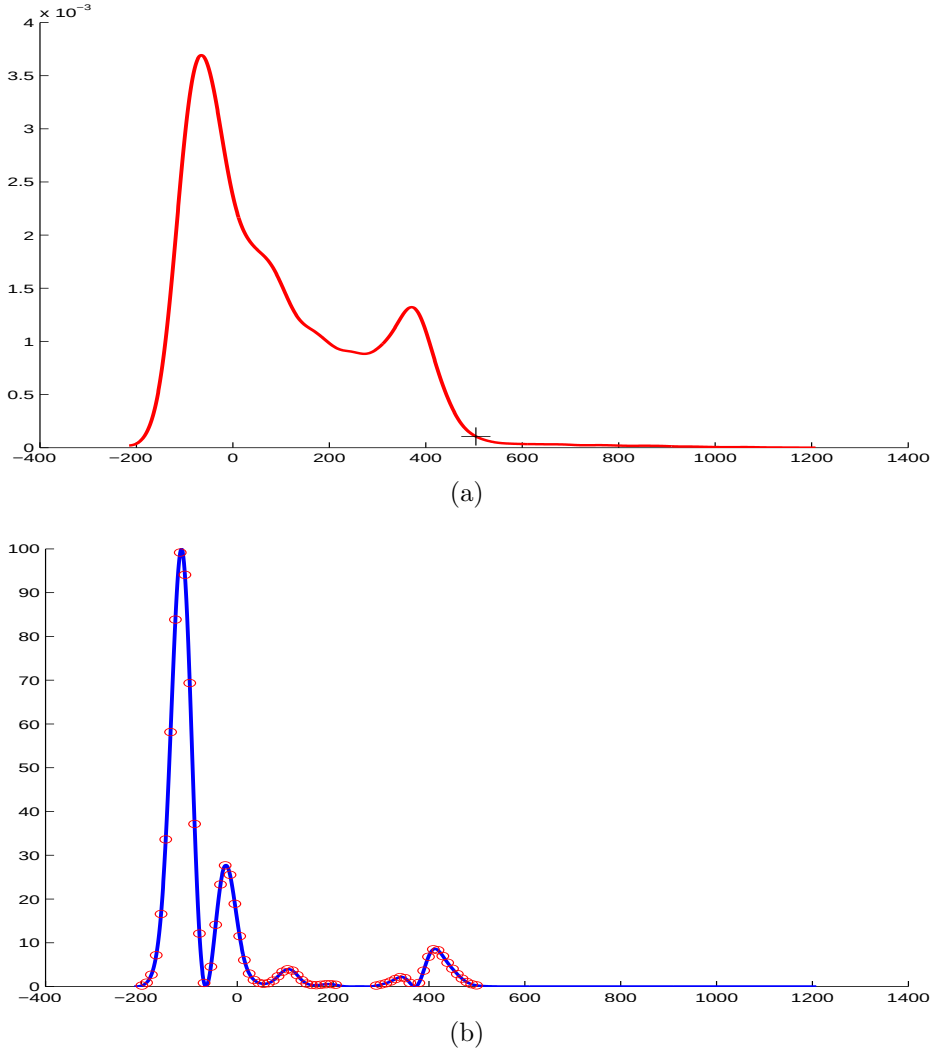

Figure 5.5 Cutoff selection from the probability density function estimated by using the Parzen window method. (a) The estimated PDF of an artery voxel intensities. Cross indicates the cutoff value selected by using the squared magnitude of its derivative (b) The squared magnitude of first derivative of the PDF. Circles mark the points where the squared magnitude of the derivative exceed ϵ.

Figure 5.6 shows the decrease in intensity along length for 4 different arteries. The x-axis is the length of the artery along the centerline and the y-axis is the intensity of the voxels. Each dot represents a voxel at a particular location along the length of the artery. In order to obtain a voxel's location in the artery, it is projected to the centerline to find the closest centerpoint. The location of the closest centerpoint is also the location of the voxel across the length of the artery. In the figure the projection is done at an interval of 0.5 mm along the centerline. The red line indicate the maximum intensity at each point and the voxels toward the higher intensity levels are high-density calcium which can be clearly separated from the contrast as indicated in figure 5.6 (a). At the base of each calcified region, there are some low density calcium the intensity range of which overlap with the contrast as indicated by the oval in the figure. The dashed black line is drawn at an arbitrary intensity level close to peak contrast intensity to indicate the decreasing intensity of contrast materials toward the distal end of the artery. The decreasing trend can be noticed very clearly in figure 5.6 which has no calcified voxels. It can also be noted from the position of black line that the intensity range of contrast is different for each figure. We observed that the contrast range differs not only across different CTA but also along the length of a single artery thus posing more difficulty in accurate quantification of calcium. This could be due to the high absorption of the contrast material toward the distal ends of the artery so that the intensity range slightly narrows down toward the distal end of an artery. Figure 5.6 shows the decrease in intensity along length for 3 different arteries. The x-axis is the length of the artery along the centerline and the y-axis is the intensity of the voxels. Each dot represents a voxel at a particular location along the length of the artery. In order to obtain a voxel's location in the artery, it is projected to the centerline to find the closest centerpoint. The location of the closest centerpoint is also the location of the voxel across the length of the artery. In the figure the projection is done at an interval of 0.5 mm along the centerline. The red line indicate the maximum intensity at each point and the voxels toward the higher intensity levels are high-density calcium which can be clearly separated from the contrast as indicated in figure 5.6 (a). At the base of each calcified region, there are some low density calcium the

intensity range of which overlap with the contrast as indicated by the oval in the figure. The dashed black line is drawn at an arbitrary intensity level close to peak contrast intensity to indicate the decreasing intensity of contrast materials toward the distal end of the artery. The decreasing trend can be noticed very clearly in figure 5.6 which has no calcified voxels. It can also be noted from the position of black line that the intensity range of contrast is different for each figure.

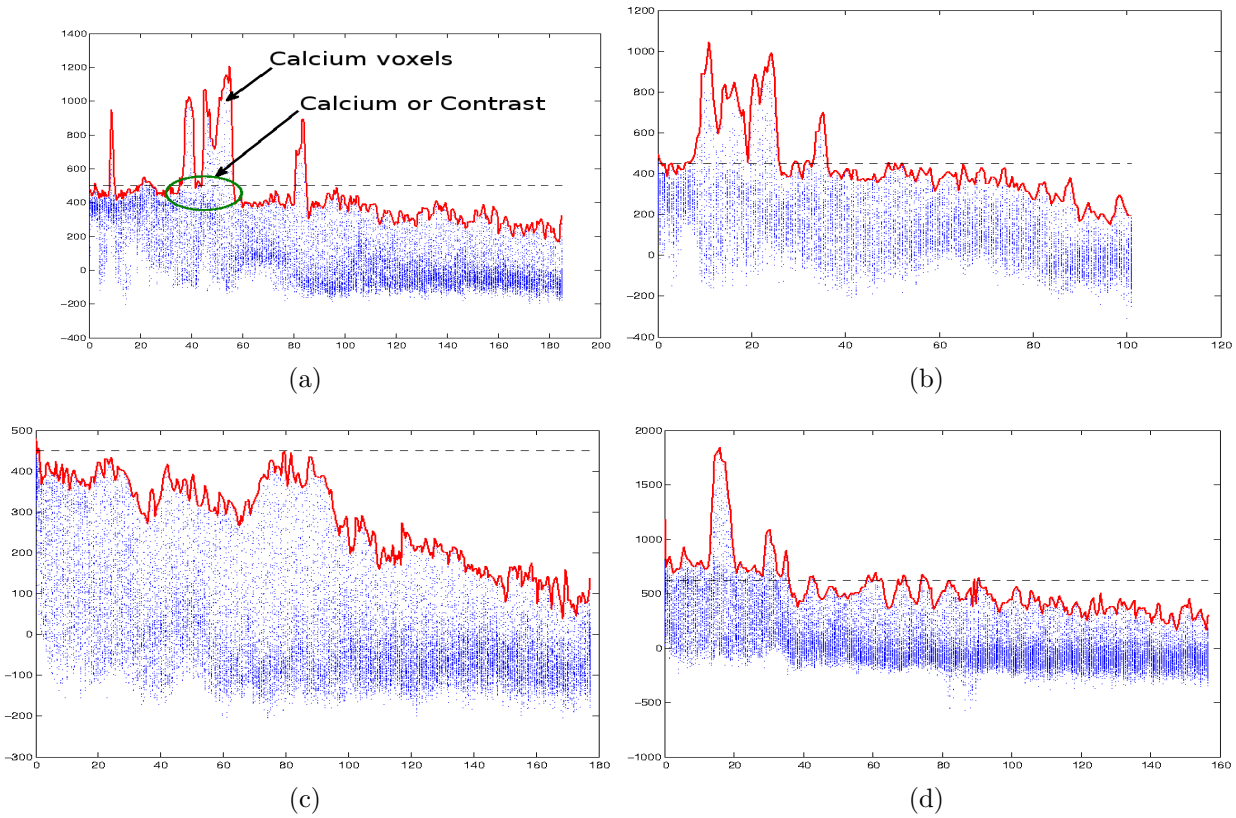

Figure 5.6 The voxel intensity along the length of arteries in different CTA volumes decrease toward the distal ends. The red line is the maximum voxel intensity along the length with regions of higher peaks having calcified voxels. The black dashed line is drawn to indicate the difference in the intensity level of contrast material along the length.

The cutoff threshold calculated from the histogram is used as a preprocessing step to calculate an adaptive threshold which depends on the peak contrast value along the length of the artery. The idea behind the adaptive cutoff threshold is to calculate approximate peak contrast values in the calcified region by smoothing and interpolating the peak contrast

values in the non-calcified regions. First, we select only the peak intensity value at a constant interval along the length of the artery. Figure 5.7 (a) shows a curve isolated from figure 5.6 (a) by joining only the peak intensity values at each x-axis location. In the second step we remove all the high-density calcium with intensities higher than the cutoff obtained from the PDF of the arterial intensities. As a result, we are left with contrast material and low density calcium as shown in figure 5.7 (b) where we do not know the peak contrast in the calcified regions around $40 - 60$ in x-axis. The peak contrast values are indicated by small circles in both figures 5.7 (a) and (b). Since the variation in contrast along the length is not regular, we developed an algorithm ("peak-fitting") to fit smooth line to the peak contrast intensities. The region of unknown peak contrast intensity are treated as missing contrast values and the "peak-fitting" algorithm automatically interpolates these missing values. The "peak-fitting" algorithm as listed in 1 is based on subsampling the known peak contrast intensities, interpolating the subsamples with cubic splines [105] and averaging the interpolated subsamples.

Algorithm 1 (peakFit) takes 5 different inputs. X is the array of input locations or the x-axis with known peak contrast values in figure 5.7. As shown by the red curve in figure 5.7 (b) Y is an array of peak contrast intensities in the location indicated by X. X_{all} is the array of the complete x-axis location including the calcified area where we want to interpolate the smoothed contrast peak values. The curve subsampled with the factor f, and dx is the distance between two consecutive x-axis points. The algorithm produces $Ymean$ as the output which is an approximation of peak contrast value in the calcified region obtained by smoothing and interpolating peak contrast values elsewhere in the plot in figure 5.7 (a).

Line 1 of the algorithm calculates the total number of points in X or th total number of known contrast peak values. Lines $2 - 3$ return if the subsampling factor is larger than the total number of points. Lines $4 - 5$ initialize empty array for padding the inputs X and Y. Padding is necessary to correct the end points after smoothing and interpolation. Lines $6 - 8$ pad the array X by extending the left-most point to $-f \cdot dx$ with f points in between. Similarly, the right-most point is extended to f points with dx interval. Lines $9 - 11$ pad

Input:
$X = [x_0, x_1, ...x_n]$: array of input location where intensity values are present,
$Y = [y_0, y_1, ...y_n]$: array of intensity values at X locations,
X_{all} : array of desired locations where the input intensities are to be fit and interpolated,
f : subsampling factor,
dx : the distance(increment) between two data locations.
Output:
$Ymean$: array of values representing the smoothed and interpolated input contrast intensities.

$N \leftarrow length(X)$;
if $f \geq N$ **then**
    return

$X_{pad}[1, N + 2 \cdot f] \leftarrow [0 \cdot 1, 0 \cdot 2, ..., 0 \cdot (N + 2 \cdot f)]$;
$Y_{pad}[1, N + 2 \cdot f] \leftarrow [0 \cdot 1, 0 \cdot 2, ..., 0 \cdot (N + 2 \cdot f)]$;

$X_{pad}[1, f] \leftarrow [-f \cdot dx, (-f + 1) \cdot dx, (-f + 2) \cdot dx...(-f + f - 1) \cdot dx]$;
$X_{pad}[f + 1, N + 1] \leftarrow X[1, N]$;
$X_{pad}[N+f+1, N+2 \cdot f] \leftarrow [X[N]+dx, X[N]+2 \cdot dx, X[N]+3 \cdot dx, ...X[N]+(f-1) \cdot dx]$;

$Y_{pad}[1, f] \leftarrow Y[1]$;
$Y_{pad}[f + 1, N + 1] \leftarrow Y[1, N]$;
$Y_{pad}[N + f + 1, N + 2 \cdot f] = Y[N]$;

$s_n \leftarrow ceil(N/f)$;
$Y_{sum} = [0 \cdot 1, 0 \cdot 2, ...0 \cdot N]$;

for $i \leftarrow 1$ **to** f **do**
    $Y_{sub}[1, s_n] \leftarrow Y_{pad}[i, i + f, i + 2 \cdot f, ..., i + sn \cdot f]$;
    $X_{sub}[1, s_n] \leftarrow X_{pad}[i, i + f, i + 2 \cdot f, ..., i + sn \cdot f]$;
    $Y_{interp}[1, N] \leftarrow splineInterp(X_{sub}, Y_{sub}, X_{all})$;
    $Y_{sum}[1, N] \leftarrow Y_{sum}[1, sn] + Y_{interp}[1, sn]$;
$Ymean[1, N] \leftarrow Y_{sum}[1, sn]/f$;

Algorithm 1: The "peak-fitting" contrast peak smoothing and interpolation algorithm (Algorithm *peakFit*).

the Y values by replicating the boundary values to the padded left and right portions. Line 12 calculates the total number points in the subsampled arrays and line 13 initializes an empty array for storing the sum of all interpolated subsamples. Lines 15 and 16 extract a subsample from the array Y, and a subsample from array X respectively with an interval of f, elements. Line 17 interpolates the subsampled function Y_{sub} to all the points in X_{all} by using cubic spline interpolation [105]. We assume the availability of the *splineInterp* cubic spline interpolation algorithm which takes function values Y_{sub} at given locations indexed by X_{sub} and interpolate them at required points X_{all}. We used the MATLAB® [86] routine `interp1` with `'spline'` parameter for the purpose. Lines $15 - 18$ are repeated for each alternating subsamples from 1 to f with line 18 taking sums of all the alternate interpolated subsamples. Line 19 takes the average of the sum of all interpolated subsamples which is the final smoothed line.

The subsampling factor f in the *peakFit* algorithm can be changed to obtain desired degree of smoothness of the peak contrast intensity. A larger value of f tend to generate smooth line with low variation while a smaller value generates curves with high variation. Figure 5.8 shows the smoothed line with different f values. We used a value of $f = 32$ as it provided an optimal cutoff value for our CTA dataset.

For a subsampling factor of f, lines $15 - 19$ are repeated f times obtaining a subsample in each iteration and interpolating each subsample with cubic spline. Thus the final smooth peak contrast line is an average of these interpolations. The individual subsample interpolation contributing to the final peak contrast smooth line are shown in figure 5.9. The thick black line is the average of the thinner spline-interpolated curves.

The final mean cutoff line $Ymean$ obtained by removing high-density calcium and using the "peak-fitting" algorithm is shown by the solid black line in figure 5.7 (b) and (c). Using the mean cutoff line directly results in the inclusion of contrast from non-calcified regions as well. Therefore, we calculated the standard deviation of the peak contrast values from the mean cutoff line and added multiple standard deviations to the mean cutoff line to obtain the absolute cutoff. We found 2.5 standard deviation from mean to provide a very good

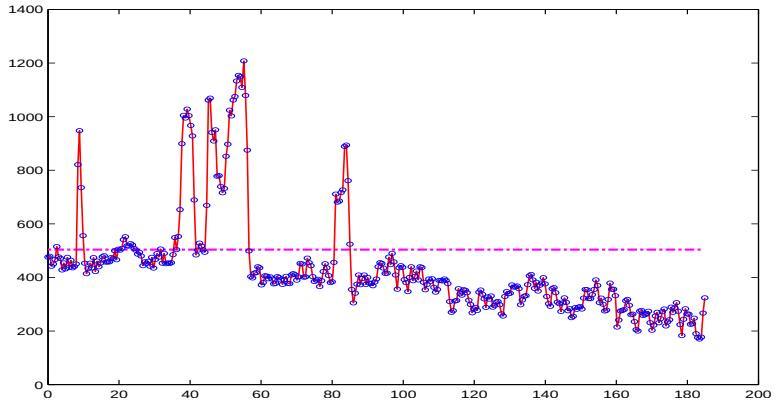

(a)

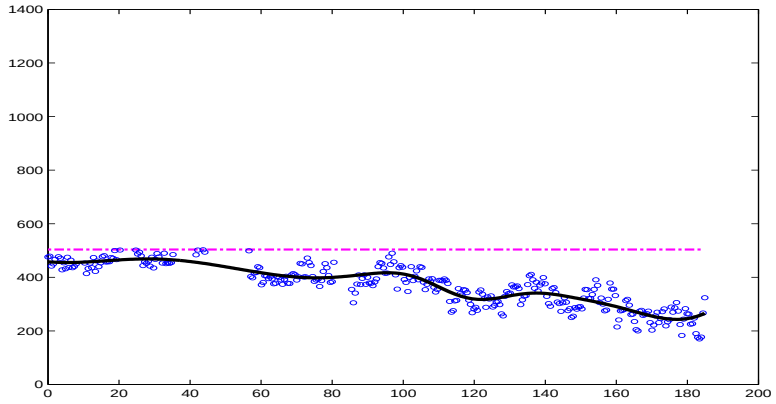

(b)

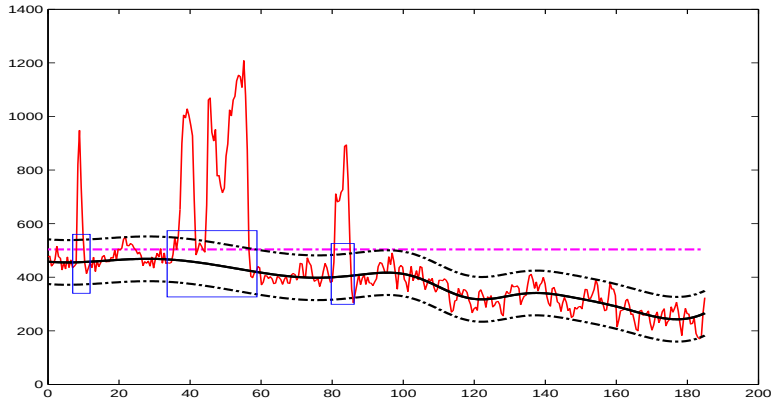

(c)

Figure 5.7 Peak intensity values, smooth adaptive cutoff threshold, and the location of high and low-density calcium. Peak intensity values along the length of the artery is shown by red curve in (a). Intensity values greater than cutoff obtained from figure 5.5 (a) are removed and smoothed by using the *peakFit* algorithm shown as solid black line in (b) and (c). The actual intensity values are indicated by small blue circles in both (a) and (b). The black dashed lines in (c) are 2.5 standard deviation apart from the mean contrast peak line. The pink dotted and dashed line shows the initial cutoff value obtained from the PDF of figure 5.5 (a). The blue rectangle in figure (c) indicates the mixed intensity range.

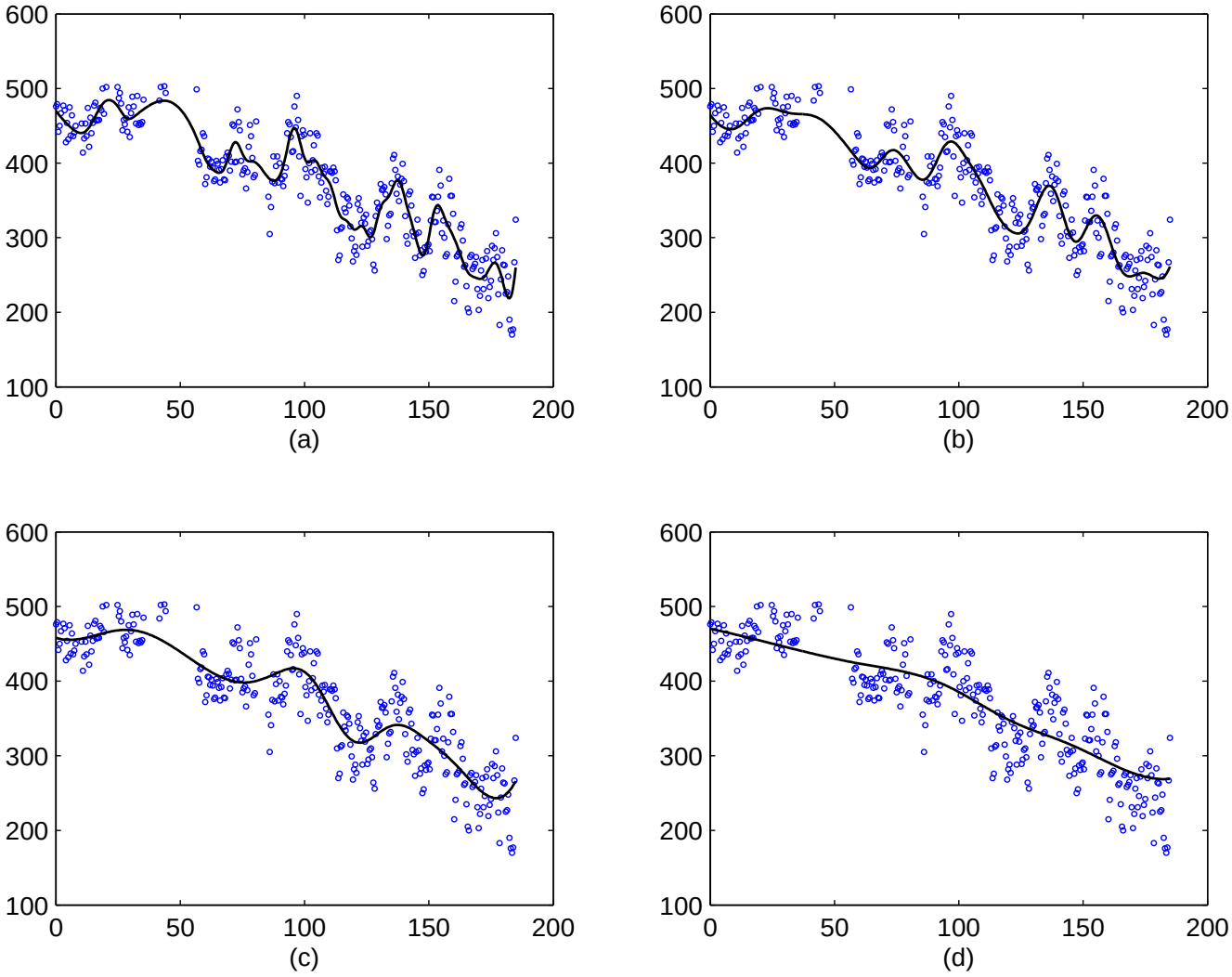

Figure 5.8 Smooth interpolation of peak contrast intensity by using the algorithm *peakFit* (algorithm 1). The algorithm run with different subsampling factor of $f = 8$ in (a), $f = 16$ in (b),$f = 32$ in (c), and $f = 64$ in (d) to smooth the peak intensity values indicated by the blue circles.

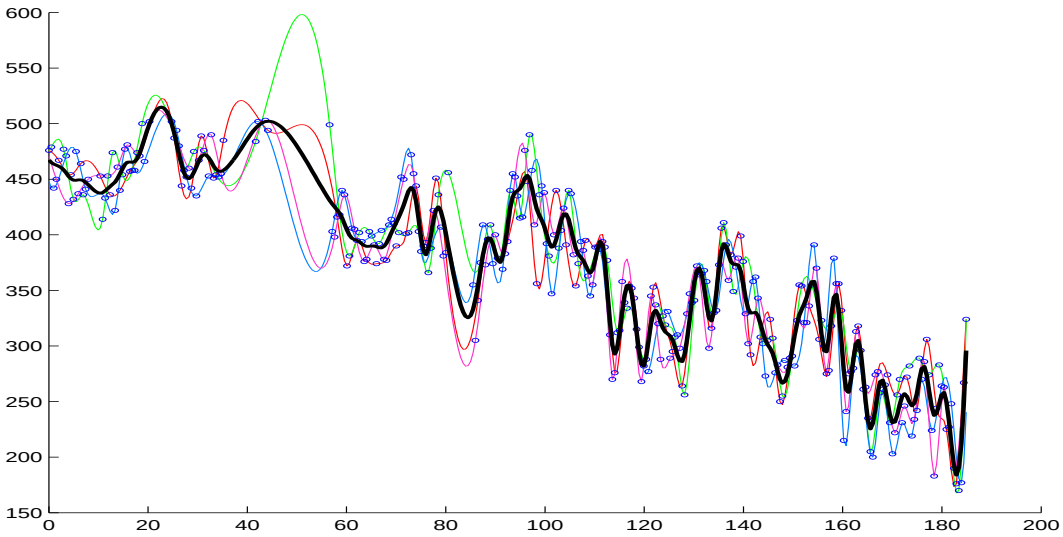

Figure 5.9 Different subsample interpolated with cubic spline in line numbers $15-18$ of Algorithm 1 ($peakFit$). The thick black line which is the final smooth peak contrast value is the average of the curves calculated by line number 19 in the algorithm.

cutoff value to exclude all the contrast and low density calcium from the experiments done in our CTA dataset. The dashed black lines in figure 5.7 (c) show the mean cutoff ± 2.5 standard deviation. Any calcified region in between these dashed line have their intensity range overlapped with that of contrast voxels. The pink dotted and dashed line in figure 5.7 (a), (b), and (c) shows the initial cutoff value obtained from the PDF of figure 5.5 (a). The blue rectangle in figure 5.5 (c) indicate the mixed intensity range of low density calcium and contrast voxels. We develop another algorithm to quantify the low density calcium in this region in the following section.

Using the peak contrast and the standard deviation, the high density calcium is calculated using the algorithm 2 ($calcHigh$). The inputs are the mean peak contrast intensity ($Ymean$) calculated by the algorithm $peakFit$, the standard deviation sd of peak contrast voxels from $Ymean$ in non-calcified regions, and $voxels$ which is a set of all voxels in the morphologically dilated artery. We assume that the voxels are organized in an appropriated data structure so that a set of all voxels at a particular location with index i can be obtained in a single operation as shown in line 3 of $calcHigh$. Since the cutoff is adaptive, it is calculated for each x-location in line 1. Line 3 counts the total number of voxels exceeding

the cutoff threshold at that location and stores it in an array. The output of the algorithm $nHigh$ is an array of the total number of high-density calcium voxels along the length.

Input:
$Ymean = [y_0, y_1, ..., y_n]$: An array of peak mean contrast value obtained by applying algorithm 1,
$voxels = v_0, v_1, ..., v_n$: set of all voxels in the dilation,
sd : standard deviation of peak contrast values from peak mean contrast value.
Output:
$nHigh$: An array of high-density calcium along the length of the artery.

```
1 nHigh ← [0 · 1, 0 · 2, ...0 · length(Ymean)];
2 for i ← 1 to length(Ymean) do
3 |   cutoff ← Ymean[i] + 2.5 · sd
4 |   nHigh[i] ← findSum(voxels[i] ≥ cutoff) ;
```

Algorithm 2: Algorithm used to find the High density calcium using the adaptive cutoff threshold ($calcHigh$).

5.2.5 Quantification of low-density calcium

Calcium appears with distinct intensity peaks and usually a plaque has a high-density center surrounded by relatively low-density calcium as observed in the CT-scan images. For an accurate calcium quantification it is important to consider all the calcified voxels. By including partially calcified and low-density calcified voxels, the accuracy of total quantified volume can be significantly improved. In this section we develop a probability based algorithm to quantify the low density calcium present in the vicinity of the high density calcium. As per our knowledge, none of the previous works has attempted to quantify the calcium in this mixed range.

Figure 5.10 (a) shows the height map or the surface plot of the intensity in a calcified region from a slice in a non-contrast CT scan. The height map is a three dimensional plot created by using the intensity level as the z-coordinates data from a CT slice. The corresponding surface plot of calcified region in the contrast-enhanced CTA is shown in

figure 5.10 (b). Both the surface plots are rotated to display the calcium peak properly. The major difference between these two surface plots is the intensity in the middle of the peaks. Since the calcification occurs only in the artery wall, these appear as peaks in the periphery of the arterial lumen which appear as valley in the middle in a surface plot. Due to the contrast enhancement in the CTA, the center portion is higher than the corresponding portion in non-contrast enhanced CT. It can be seen that in a non-contrast enhanced CT, much of the low density calcium are distinct from the lumen while in case of contrast-enhanced CTA, the low density calcium are largely occluded by the contrast material.

The voxels outlined by blue rectangles in the plot of figure 5.5 (c) are in the overlapped intensity range of low density calcium and contrast voxels. A magnified portion of the calcified region and the overlapped intensity range is shown in figure 5.11 (b). In the overlapped intensity range, we cannot tell precisely if a voxel is calcium or contrast just by looking at the intensity of the voxel. The algorithm we developed to quantify calcium in this region is similar to the *peakFit* algorithm, in that both the algorithms use information of contrast voxels in the non-calcified area to estimate the total probability of contrast voxels in in the calcified area.

Our algorithm first calculates the total number of contrast voxels in mean peak intensity value ± 2.5 standard deviation range. The mean peak intensity is shown by a thick black line and the 2.5 standard deviation from the mean are shown by the dashed black lines in the figure 5.11. All the peak contrast intensity variations shown by red curve in figure 5.11 (a) lie between these two standard deviation lines. Therefore, we calculate the total area occupied by contrast voxels in the non-calcified regions (labeled "N" in figure 5.11 (a)) bounded by the two lines. The total contrast area (bounded by the red curve and the lower standard deviation line) divided by the total area between the standard deviation lines in the non-calcified regions gives us an estimate of the fraction of contrast material in between the lines. We then apply this fraction to estimate the total amount of contrast in the calcified regions (labeled "M" in figure 5.11 (a)).

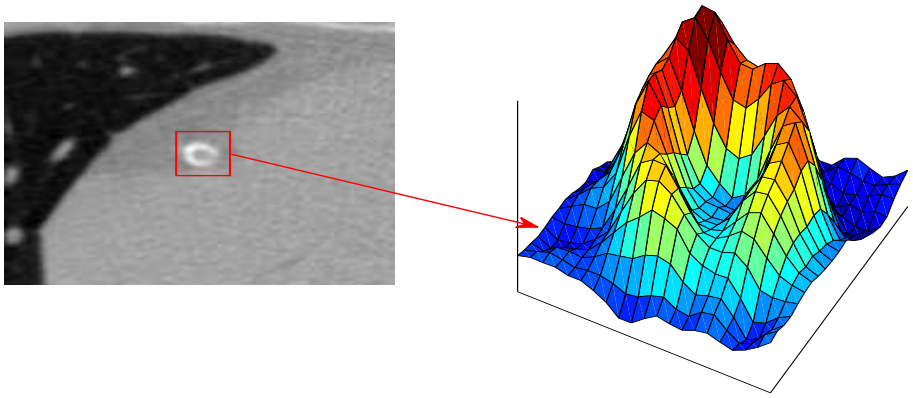

(a)

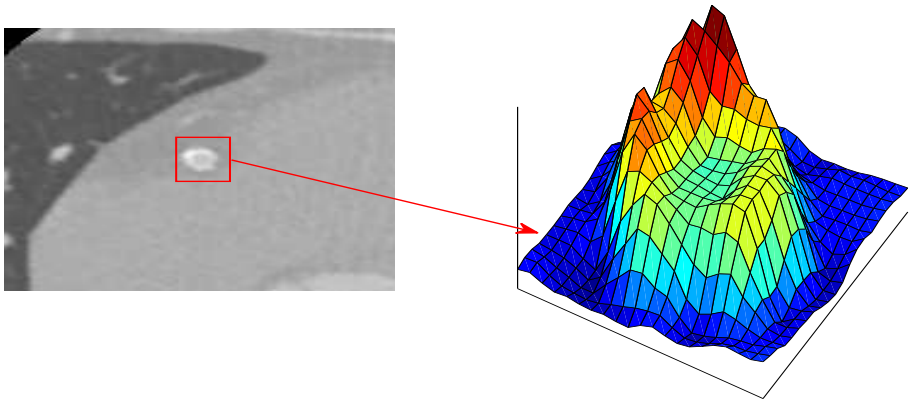

(b)

Figure 5.10 Surface plot of the intensity in a calcified region indicated by the red square in a (a) non-contrast-enhanced CT slice and the corresponding slice in (b) contrast-enhanced CTA.

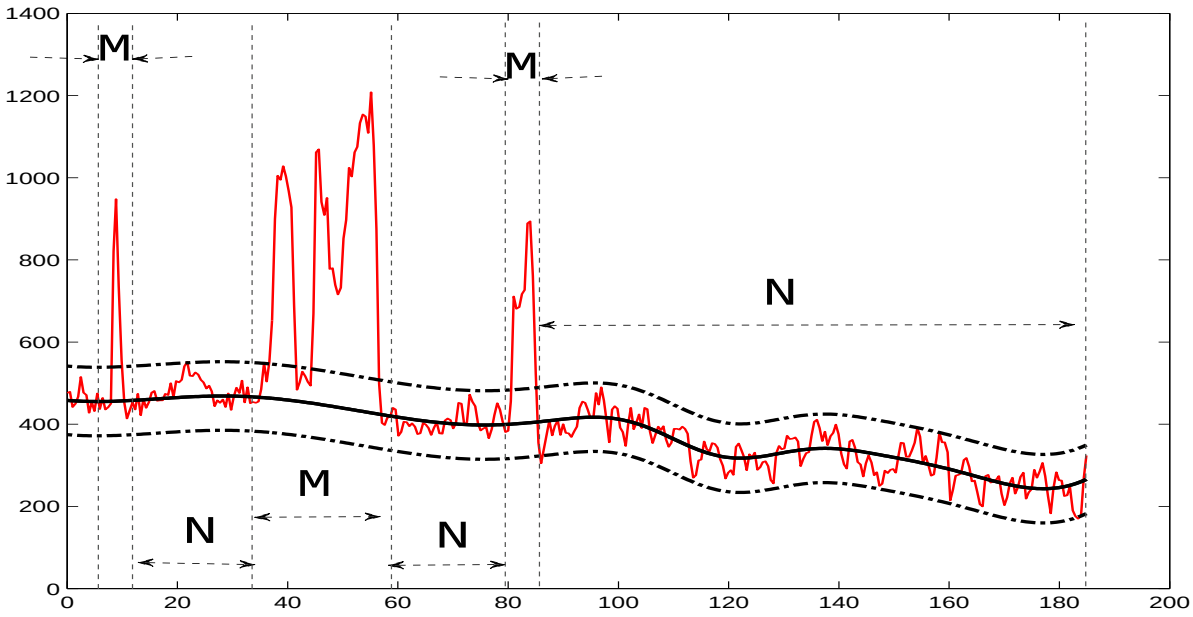

(a)

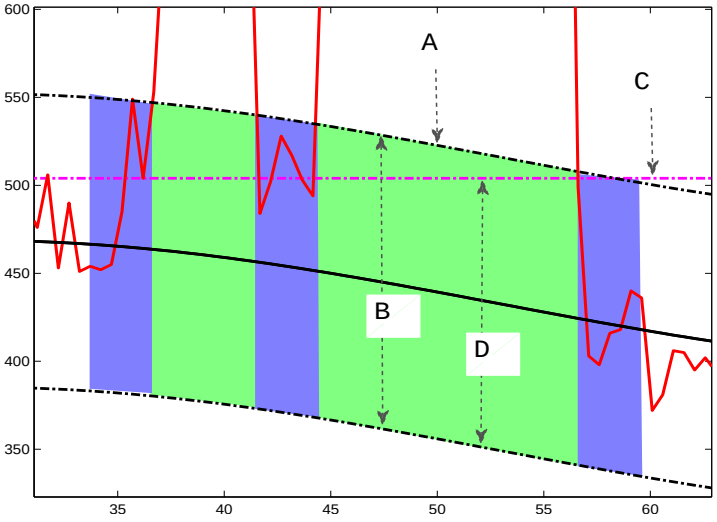

(b)

Figure 5.11 Calcified and non-calcified regions in the lengthwise intensity plot with the high-density, and the low-density calcium voxels locations. (a) Calcified regions are labeled "M" and the non-calcified regions are labeled "N". The total area bounded by the red curve and the lower standard deviation line indicated by dashed line divided by the area between the dashed line in region "N" gives us an estimate of a fraction of contrast material in region "M". (b) A magnified calcified region to show the discrepancy of a single cutoff threshold and adaptive cutoff threshold. "A" is the adaptive cutoff threshold, any voxel intensity above "A" is calcium. "C" is the fixed cutoff threshold which is uniform lengthwise, the range "B" has low-density calcified voxels as well as contrast and "D" is the range of intensities excluded by considering a single cutoff threshold only.

Input:
$Ymean = [y_0, y_1, ..., y_n]$: An array of peak mean contrast value obtained by applying algorithm 1,
$Imax = [i_0, i_1, ..., i_n]$: array of maximum intensity values along the length,
sd : standard deviation of peak contrast values from peak mean contrast value.
Output:
p : Probability of contrast material in the non-calcified area.

```
1  j ← 1 ;
2  for i ← 1 to length(Ymean) do
3      if (Imax[i] < Ymean[i] + 2.5 · sd)&(Imax[i] >= Ymean[i] − 2.5 · sd) then
4          a ← Ymean[i] + 2.5 · sd ;
5          b ← Ymean[i] − 2.5 · sd ;
6          P[j] ← (Imax[i] − b)/(a − b) ;
7          j + + ;
8  sum ← 0
9  for j ← 1 to length(P) do
10     sum ← P[j] ;
11 p ← sum/length(P) ;
```

Algorithm 3: Algorithm used to find the fraction of contrast material in the non-calcified region (*probContrast*).

The steps to calculate low density calcium lengthwise are listed in algorithms 3 (*probContrast*), and 4 (*calcLow*). First, the algorithm *probContrast* calculates the probability or the fraction of peak contrast material in non calcified region labeled as "N" in figure 5.11 (a). Then the algorithm *calcLow* calculates the probability or the fraction of calcium in the calcified area labeled "M" in figure 5.11 (a) by using the p value calculated by the *probContrast* algorithm.

The algorithm *probContrast* needs $Ymean$ which is an array of the mean peak contrast intensity calculated by the algorithm *peakFit*, $Imax$ an array of maximum intensity value along the length, sd the standard deviation of the peak contrast intensity from the mean

peak contrast intensity in the non-calcified regions, and p which is the fraction of contrast material in the non-calcified region "N" in figure 5.11 (a). The output is the fraction or the probability of contrast voxels in the non-calcified region between the two 2.5 standard deviation lines.

Lines $2-7$ are repeated for each x-axis position and if the peak contrast intensity at an x location is between the 2.5standard deviation lines is checked by line 3. Therefore lines $4-7$ are executed for the peak contrast intensity in the non-contrast regions only. Line 6 calculates the fraction of peak contrast intensity within the standard deviation range $a$and b at each x-axis location. Lines $8-11$ calculate the average of the peak contrast fraction p across all non-calcified locations. P in line 6 should be initialized with a dynamic array outside the loop which has not been shown in the algorithm.

Input:
$Ymean = [y_0, y_1, ..., y_n]$: An array of peak mean contrast value obtained by applying algorithm 1,
$Imax = [i_0, i_1, ..., i_n]$: array of maximum intensity values along the length,
$voxels = v_0, v_1, ..., v_n$: set of all voxels in the dilation,
sd : standard deviation of peak contrast values from peak mean contrast value,
p : The peak contrast probability calculated by using algorithm, 3.
Output:
$nLow$: An array of low density calcium along the length of the artery.

```
1 nLow ← [0 · 1, 0 · 2, ...0 · length(Ymean)];
2 for i ← 1 to length(Ymean) do
3     if Imax[i] > Ymean[i] + 2.5 · sd then
4         a ← Ymean[i] + 2.5 · sd ;
5         b ← Ymean[i] − 2.5 · sd ;
6         v[i] ← findSum(voxels[i] ≥ a&voxels[i] ≤ b) ;
7         nLow[i] = v[i] · (1 − p) ;
```

Algorithm 4: Algorithm used to find the fraction of contrast material in the calcified region (*calcLow*).

The algorithm *calcLow* needs similar inputs as the algorithm *probContrast* and in

addition it also needs its output p which is the fraction of contrast in the non-calcified region, *voxels* which is the set of all voxels in the morphologically dilated artery. We also assume that the voxels are organized in an appropriated data structure so that a set of all voxels at a particular location with index i can be obtained in a single operation as shown in line 5 of *calcLow*. The output *nLow* is an array with the fraction of total voxels with low-density calcification.

Since the low density calcium is present in the proximity of high-density calcium, line 2 checks for the presence of high density calcium by using the cutoff of $Ymean + 2.5 \cdot sd$ at the particular location. Thus, lines $3 - 6$ are calculated for the voxels in between the two standard deviations in the calcified regions. Line 5 calculates the total number of voxels lying between the standard deviations at an x location in a calcified region. The total number of voxels is multiplied by the probability of calcium, i.e. $(1 - p)$ to estimate the fraction of calcium at each location.

The area of low density calcium is shaded green in figure 5.11 (b). Although, figure 5.10 shows the distribution of calcium in 2-dimensional slice, a calcified-plaque appears contiguously across adjacent slices. The x-axis in figure 5.11 does not necessarily correspond to a slice in the CT volume but the low density calcified voxel may be projected to adjacent centerpoints. Therefore, we also calculated the low density calcium in the adjacent regions shaded blue in 5.11 (b). The calculation of calcium in adjacent centerpoints is not shown in algorithms 4 for simplicity. Similarly this adjacent region was treated as low-density calcium in algorithm 3 but not shown for simplicity. The label "A" points to the adaptive cutoff which is different for each x-location, label "C" points the fixed cutoff threshold calculated from the Parzen window PDF. Label "D" points the total low-density calcium voxels missed by considering the fixed cutoff threshold only.

5.2.6 Calcium quantification

We calculate the calcium volume along the length of an artery at a very detailed interval of 0.5 mm which is summarized as follows. As discussed in subsection 5.2.1, first we extract

the centerline of a desired artery automatically. The details of this method is described in chapter 4. The centerline is morphologically dilated to cover all the arterial voxels and possibly including the myocardial tissue as outlined in subsection 5.2.2. The intensity of these voxels are statistically analyzed to estimate a probability density function (PDF) of the intensity distribution as described in subsection 5.2.3. By excluding a shallow tail of calcium in the right side of the PDF, an initial high-density calcium cutoff intensity (cut_{PDF}) is calculated.

In subsection 5.2.4 we showed that the peak contrast intensity drops along the length of the artery and developed an algorithm to find the adaptive cutoff threshold ($cut_{adaptive}$) to extract the high density calcium voxels. An adaptive cutoff threshold is different along the length of the artery depending on the peak contrast intensity at the location. The initial cutoff cut_{PDF} and the peak contrast intensity along the length of artery are used to calculate an adaptive cutoff threshold as listed in the $peakFit$ algorithm (Algorithm 1).

Low-density calcium that are present in the vicinity of high-density calcium and are calculated by algorithms $probContrast$ and $caclLow$ (Algorithm 4). The $cut_{adaptive}$ threshold is used by both these algorithms to find the low-density calcium area. First, the $probContrast$ algorithm (Algorithm 3) finds the fraction of calcium in the low-density calcium area and the algorithm $calcLow$ calculates the total low density calcium lengthwise. The total number of calcium voxels along the length is the sum of high-density calcified voxels $nHigh$ and low-density calcified voxels $nLow$ calculated by the algorithms $calcHigh$ (Algorithm 2), and $calcLow$ respectively. The final calcium volume is obtained as follows,

$$calcVoxels = nHigh + nLow, \tag{5.4}$$

$$calcVol = calcVoxels \times voxelVolume, \tag{5.5}$$

where the sum is vector sum for the elements of $nHigh$ and $nLow$. $calcVoxels$ gives a total number of calcified voxels which when multiplied by the volume of a voxel ($voxelVolume$)

gives the calcium volume per increment (0.5 mm) along the artery.

5.3 Software Developed

In this section we describe the software tools and user interface (UI) developed for manual and automatic extraction of coronary arteries, selecting a desired artery to extract the centerline, and registration and transformation of non-contrast-enhanced and contrast-enhanced CT. All the software tools were developed using MATLAB^{TM} programmatically, and also interactively by using the MATLAB graphical user interface development environment (GUIDE) [106].

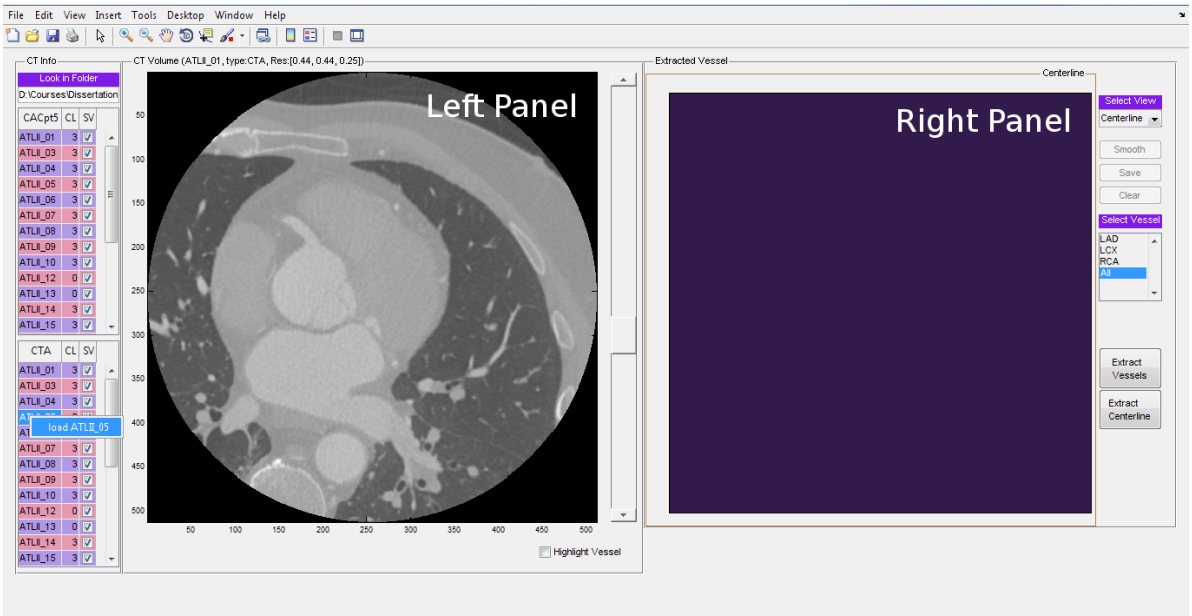

Figure 5.12 Main GUI for browsing CT volumes.

The software tool developed in Chapter 3 for manually annotating and extracting centerline was extended to provide support for automatic extraction, and selection of vessels. A snapshot of the main GUI is shown in figure 5.12. The main GUI was developed programmatically by using nested functions in MATLAB. The main GUI has two different panels in the left and the right. The panel on the left side is for displaying CT volumes. The panel

on the right side is for displaying extracted arteries, centerlines, calcium curve, and calcium profile from a selected CT volume.

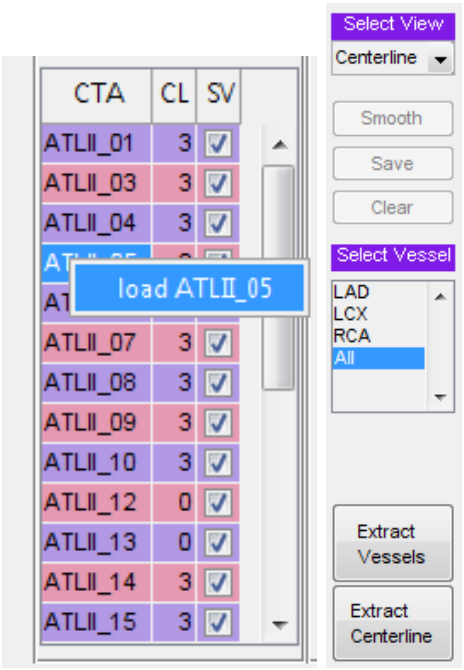

(a) (b)

Figure 5.13 UI Controls (a)Table for browsing and loading CTA volumes(b) Controls for manual and automatic artery extraction.

The non-contrast-enhanced, and contrast-enhanced CT volume files are listed on two separate tables on the left-most side, one of which is shown separately in figure 5.13(a). Each row of the table has a context menu to load the selected file into the software for further processing. After loading a CT volume, a user can scroll through different slices of a volume by using the scroll bar attached to the image panel or by using the mouse scroll wheel.

Different functionalities are achieved through the button control on the right-most side of the software which is also shown in figure 5.13 (b). User can manually annotate a visible section of an artery as shown by the red cross in the figure 5.14. The 3D location of manually clicked points are extracted as shown in the right side panel in figure 5.15. These points are used to approximate a centerline by using the smoothing step.

The dialog for selecting parameters for smoothing and dilation is shown in figure 5.16

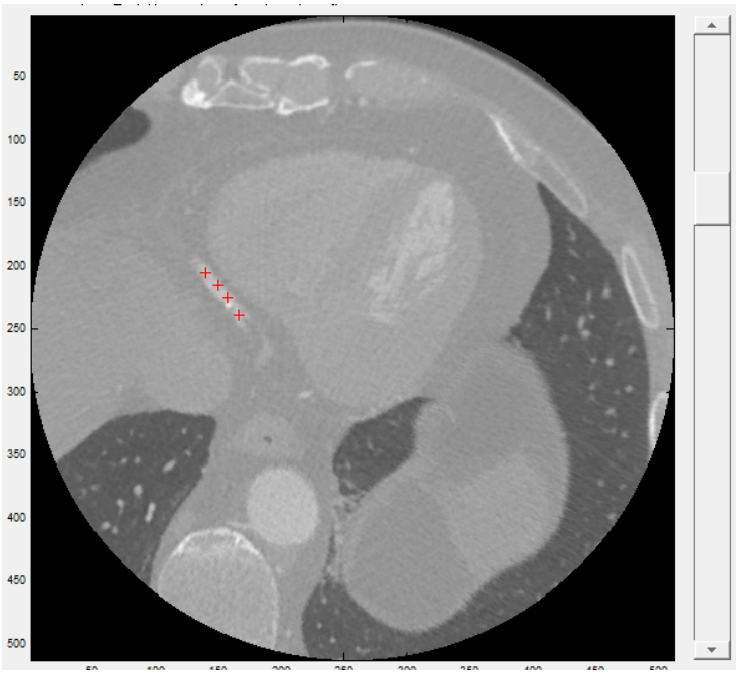

Figure 5.14 Visible section of arteries annotated manually.

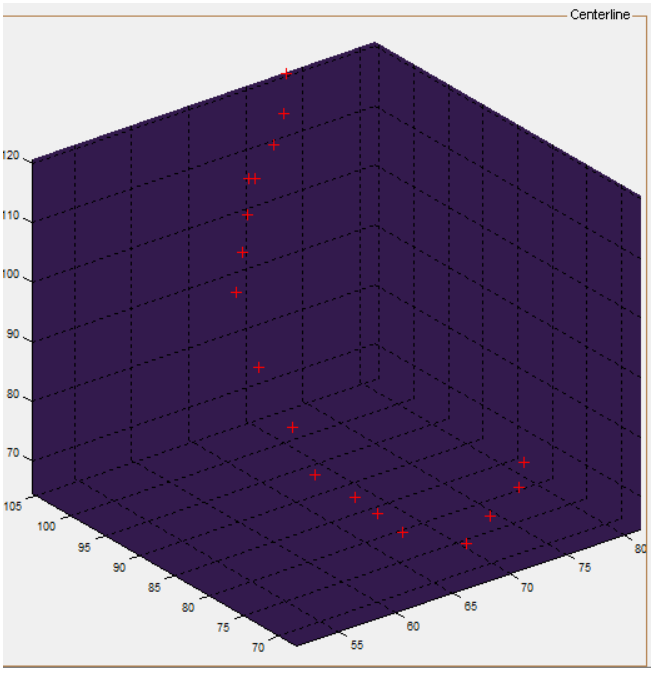

Figure 5.15 Centerpoints extracted in 3D from the annotation.

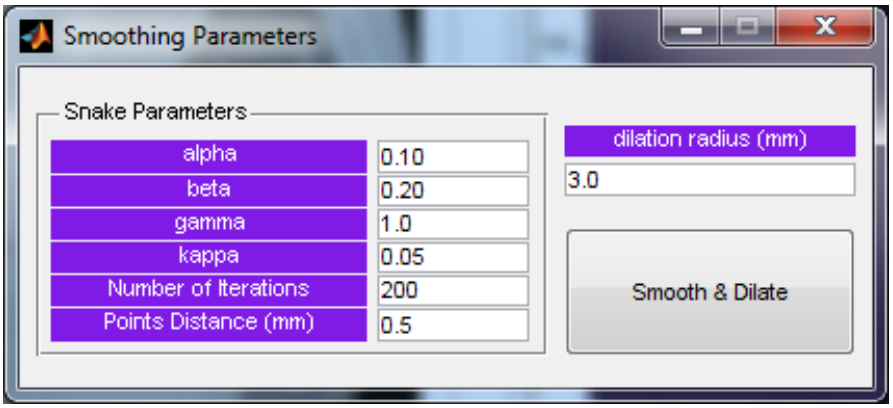

Figure 5.16 Dialog showing different smoothing and dilation parameters.

which is invoked by pressing the 'Smooth' button. Pressing the 'Smooth & Dilate' button in the dialog results in a centerline and a dilated artery as shown in the right panel of figure 5.17

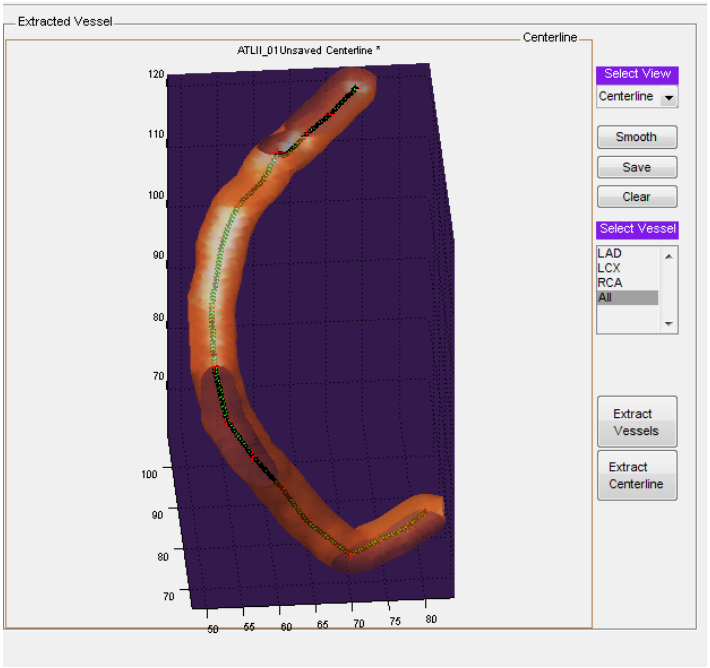

Figure 5.17 The 'centerline' view showing the dilated artery and its centerline.

Figure 5.17 is the centerline view which is the default view. A different view can be selected by changing the selection of combo box 'Select View' in the right side. Figure 5.18 (a) shows the calcium volume view which plots the lengthwise calcium volume (mm^3) of the selected artery. The Hounsfield Unit (HU) threshold for calcium can be changed with the

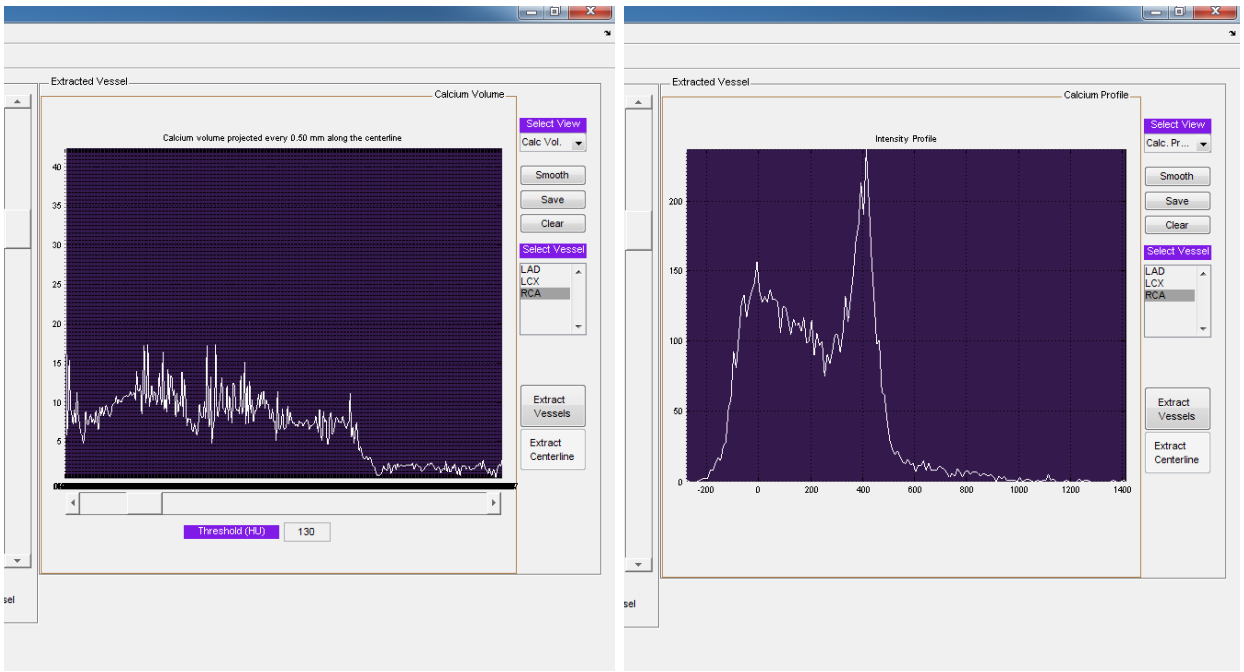

(a) (b)

Figure 5.18 (a) Calcium volume view shows the lengthwise calcium volume in mm^3. The HU threshold can be changed by using the threshold slider and the volume changes accordingly(b) Calcium profile view shows the intensity profile or the histogram of the voxels in the artery.

slider in the bottom. Figure 5.18 (b) shows the calcium profile view which is the intensity profile or the histogram of the HU intensities of the voxels in the selected artery.

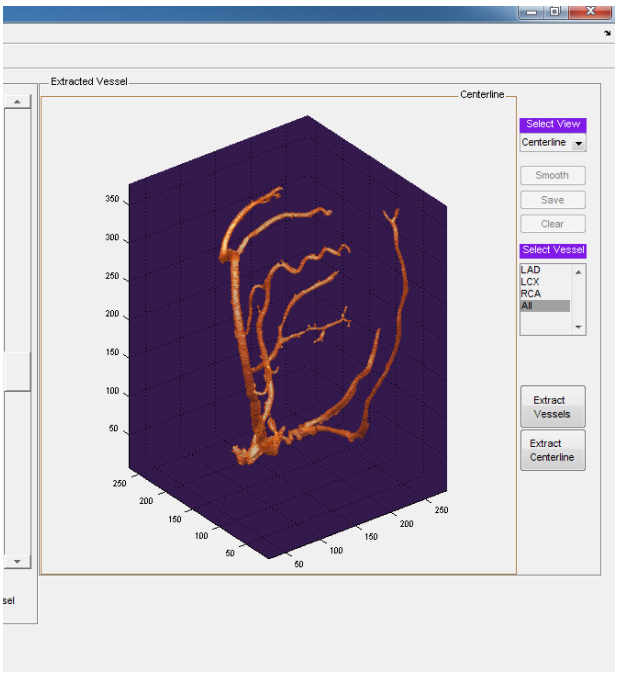

Figure 5.19 Automatically extracted arteries.

Figure 5.19 shows vessels extracted automatically by pressing the 'Extract Vessels' button. In order to select a particular branch and extract its centerline, we developed another GUI shown in figure 5.20

The GUI in figure 5.20 is used to mark end points of a desired vessels. In order to facilitate the end point selection, the arteries can be rotated in 3D by using the two sliders. A desired artery can be isolated for proper point selection by clicking on the artery and pressing the 'Filter' button. Connected component of the clicked point is used to isolate the artery. The isolated artery is shown in figure 5.21. Centerlines between the selected end points are extracted automatically on exiting the GUI.

After automatic centerline extraction and dilation of an artery, the software also automatically segments the dilated voxels into lumen, artery wall, and myocardial tissue. The segmentation can be viewed by checking the 'Highlight Vessel' checkbox and then scrolling through the slices which is shown in figure 5.22.

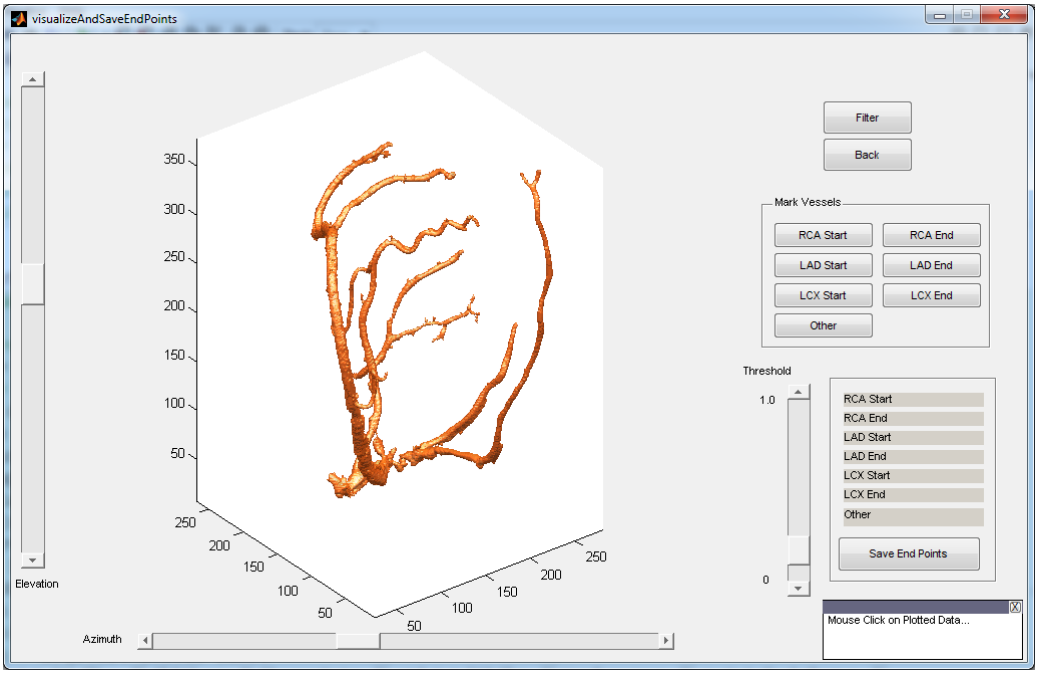

Figure 5.20 GUI visualizing and selecting the end points of a desired artery.

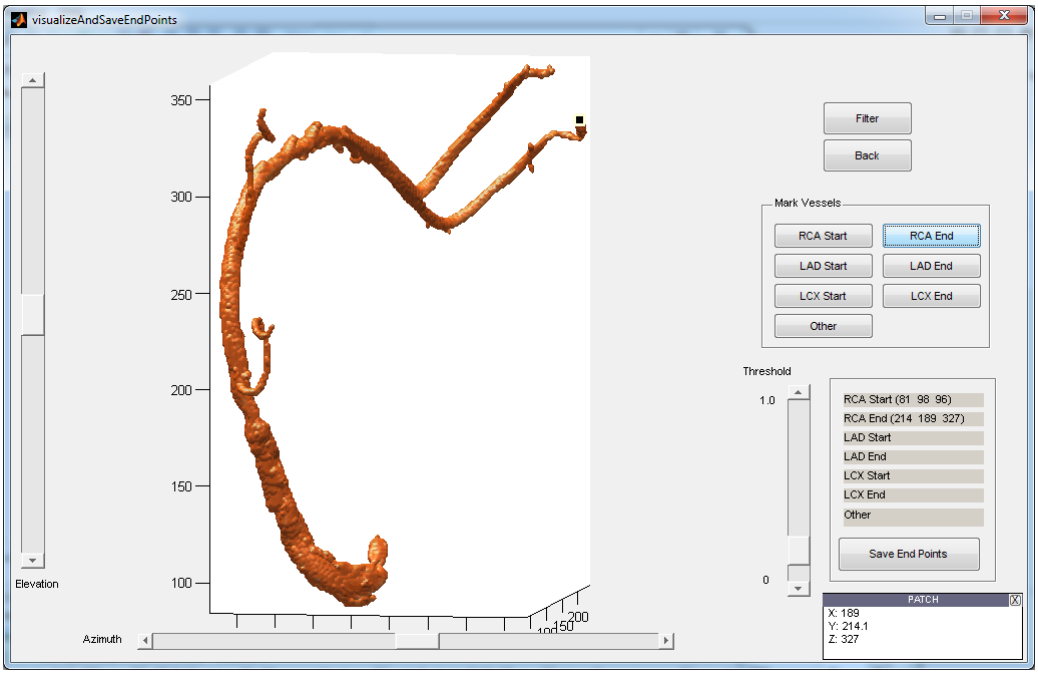

Figure 5.21 Selecting a particular artery for end points selection.

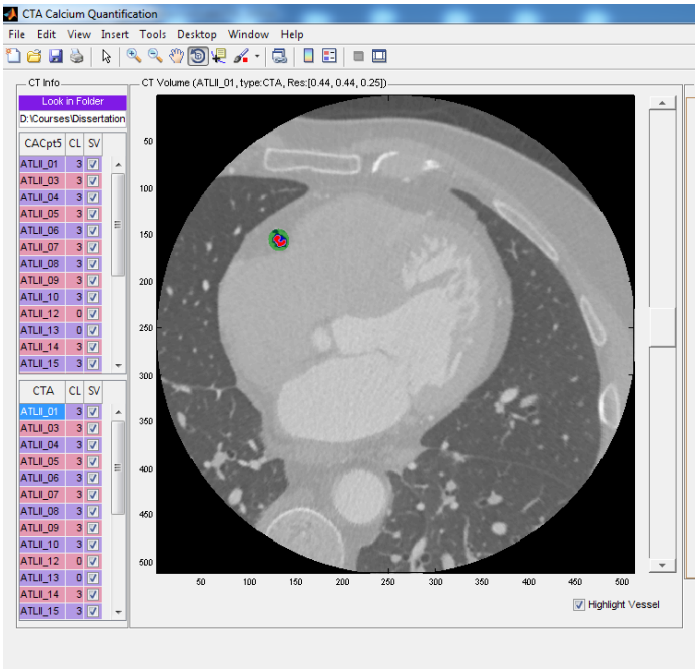

Figure 5.22 Left panel showing a segmented artery section.

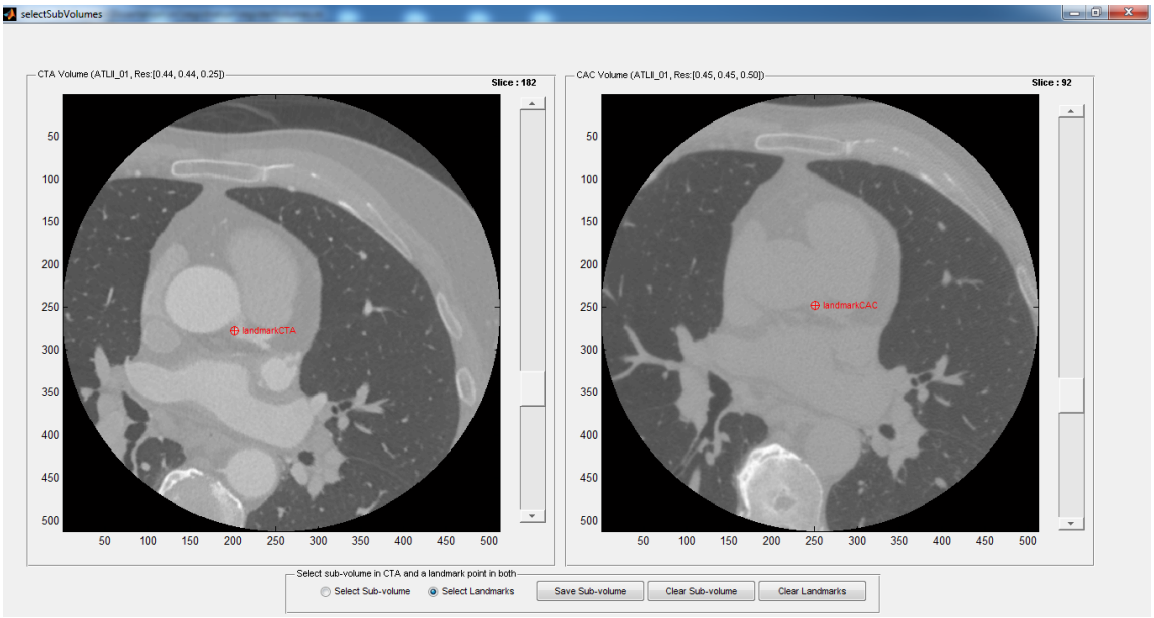

Figure 5.23 GUI for selecting landmarks and extracting subvolume for registration.

We also developed software tool for manual and automatic registration. Figure 5.23 shows the GUI developed for manually registering the non-contrast-enhanced and contrast-enhanced CT scans by selecting landmark points. The GUI also allows subvolume selection from both the CT scans and the selected landmarks are used for a coarse registration by using linear transformation.

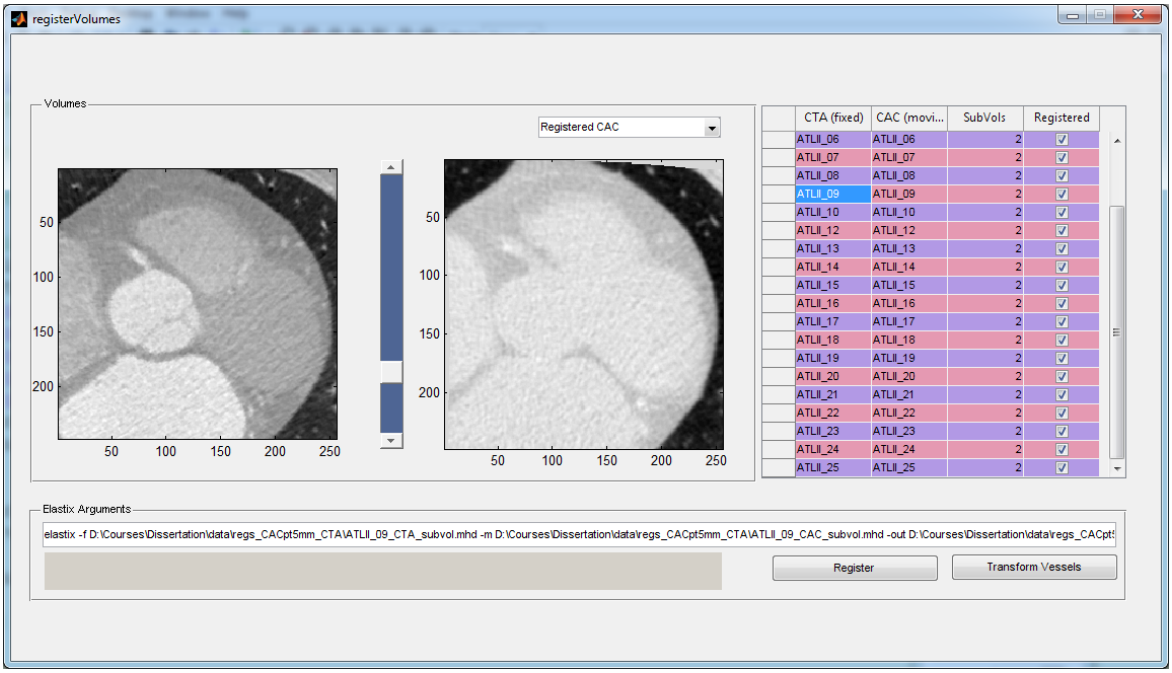

Figure 5.24 Main GUI for registering the contrast-enhanced and non-contrast-enhanced CT subvolumes.

Figure 5.24 shows the main GUI for registering a non-contrast and contrast-enhanced CT. Using this GUI tool, the coarsely registered subvolumes are further refined by using non-rigid registration. The registration parameters can also be used to transform a particular artery in contrast-enhanced CTA to a corresponding artery in non-contrast-enhanced CT. The registration GUI provides interface for the elastix, and transformix tools [107] which are actually used to perform the registration and transformations respectively.

5.4 Summary

In this chapter we developed methodologies to quantify calcium from the non-contrast-enhanced computed tomography angiography (CTA). We developed algorithms to calculate an adaptive cutoff threshold that separates high-density calcium along the length of artery. We also quantified the low-density calcium which are in the overlapped intensity range to the contrast voxels by using a probability based method to estimate the total amount of contrast in the calcified region. The total calcium is then the sum of both high-density and low-density calcium at each position along the length of artery.

CHAPTER 6

VALIDATION OF THE CALCIUM QUANTIFICATION

6.1 Introduction

In this chapter we present the experiments done to automatically extract calcium from contrast-enhanced computed tomography angiography (CTA). This includes extracting vessels and centerline, quantification of the calcium along the length of centerline, validation of the quantification with the intravascular ultrasound, the calcium quantification between contrast-enhanced computed tomography angiography (CTA) and non-contrast-enhanced CT (CAC), and the software tools developed for the tasks. The implementation of the quantification process was done in a GUI based prototype software which can be developed into a fully functional clinical package with minimal efforts. For an accurate, lengthwise comparison, another set of software tools were developed for the registration of subvolumes, and transformation of the blood vessels derived from the CTA to CAC.

In order to validate our methods, we do lengthwise comparison of the calcium volume obtained from CTA with calcium volume obtained from the intravascular ultrasound with Virtual Histology ^{TM} (Volcano Corporation) (IVUS-VH). In addition, we also compare the calcium volume obtained from the CAC to the IVUS-VH, and the volume obtained from the CTA data set.

The IVUS-VH acquires a stack of 2D cross-sectional images from inside an artery and lacks the knowledge of 3D Cartesian coordinates, while CAC is a 3D volumetric data set that includes all the anatomical structures in the thoracic area. Therefore, to compare the calcium obtained from the CT data we need to extract and align the arteries with the artery obtained from the IVUS-VH images. In the following subsections, we also describe the alignments or the registration done for the lengthwise statistical comparison of the calcium volume obtained in these different modalities. The results from our experiment show that the proposed

calcium quantification method using CTA outperformed the best calcium quantification by using 0.5 mm CAC as compared to the IVUS-VH.

6.2 IVUS Image Acquisition and calcium quantification

In IVUS the images are reconstructed by acquiring the ultrasound waves reflected from the artery wall and the surrounding tissues. A catheter travels through artery emitting ultrasound waves which gets reflected from the arterial wall and the surrounding tissues. The amplitude of the reflected waves are used to construct images of different layers of the arterial wall. The frequency of the reflected waves are used to classify different tissue components and different colors are assigned to these components with a technology called Virtual Histology (VH) which is the trademark of Volcano Corporation, San Diego, CA, USA. The white pixels shown in the figure are dense calcium, red ones correspond to the necrotic core, light-green are fibrofatty and green are fibrous tissues. The particular frame in figure 6.1 shows a highly calcified plaque which is found in an arterial wall in the proximity to the lumen.

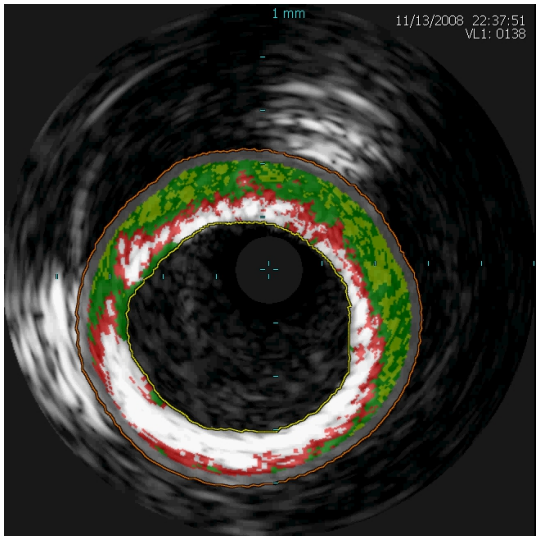

Figure 6.1 A frame of IVUS-VH showing an artery section with highly calcified plaque. The white pixels are dense calcium, red ones correspond to the necrotic core, light-green are fibrofatty and green are fibrous tissues.

The IVUS-VH has been shown to analyze different components with very high predictive accuracies. Nasu et al. demonstrated the accuracy of IVUS-VH by first obtaining IVUS-VH images from inside the arteries and then by comparing the color-coded tissue components in the images with actual histology of the plaque tissues obtained by a procedure called directional coronary atherectomy [25]. The directional coronary atherectomy is a medical intervention to remove the arterial blockage by cutting away the plaque tissue from inside an artery. In another study by Nair et al. the IVUS-VH images were compared against the histology of the plaque tissue obtained from the arteries cut from dead subjects [7]. Both the studies reported the IVUS-VH to have a predictive accuracy of more than 96% for dense calcium. Therefore, we use the IVUS-VH in our preliminary study (Chapter 3) as well as in this chapter to assess the calcium quantification accuracy by using non-contrast-enhanced CT (CAC) and the contrast-enhanced CTA scans.

IVUS-VH images were acquired in a IVUS-VH console with a catheter (Eagle Eye, Volcano Corporation). A medication called Nitroglycerin was injected to enlarge the blood vessels so as to facilitate the movement of the catheter. The catheter was advanced beyond the plaque area target for the study and automated pullback was done at a rate of 0.5 mm/sec. A medical doctor was asked to manually delineate the lumen contour and the outer boundary of the arterial wall on the image. Then, the IVUS-VH console automatically classified the plaque area in between the two contours into 4 plaque compositions, by analyzing the reflected ultrasound signals using a principal component analysis (PCA)-based algorithm [7].

Since, the resolution of each IVUS-VH frame and the distance between each frame are known, the total calcium volume in each frame is obtained by multiplying the total calcified area in frame with the resolution and inter-frame distance. The calcium volume (in mm^3) for each frame in an IVUS-VH image of the right coronary artery (RCA) of a patient is shown in figure 6.2.

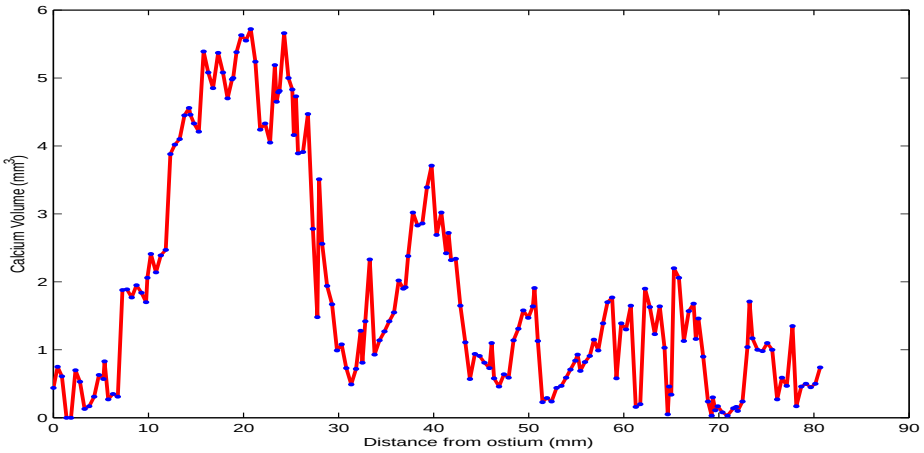

Figure 6.2 Calcium volume for each frame in the right coronary artery. The distance of each frame from the ostium of the coronary artery is shown as the x-axis. The blue dots represents the actual calcium level in each frame.

6.3 Calcium quantification from the computed tomography (CT)

We performed a lengthwise comparison of the calcium volumes obtained from both the contrast-enhanced and non-contrast enhanced CT scans with the IVUS-VH derived calcium volumes. The lengthwise calcium quantification requires a complete extraction of artery, centerline and the analysis of voxel intensities around the centerline. The method for calcium quantification from the contrast-enhanced CTA is described in details in chapter 5 and briefly summarized below. A manual method for calcium quantification from non-contrast-enhanced CT (CAC) is presented in chapter 3. However, for a fair comparison of the calcium quantification, we develop the automated calcium extraction from the non-contrast-enhance CAC in this chapter. The automatic centerline and vessel extraction in the CAC is based on the registration and transformation of vessels extracted from the contrast-enhanced CTA as will be discussed in the subsequent subsections.

6.3.1 Automatic vessel extraction from the contrast-enhanced computed tomography angiography (CTA).

Calcium quantification along the length of an artery required the complete extraction of a desired branch of the artery. Automatic artery extraction is facilitated by the contrast-

enhancement of the lumen. Therefore we used a geometry based approach to automatically extract the arteries by using Frangi's vesselness filter [76]. An experiment of different parameters selection for the filter is presented in chapter 4. Figure 6.3 (a) shows a right coronary artery (RCA) extracted by applying the vesselness filter and by considering the largest connected component. Figure 6.3 (b) shows the cerebral arteries extracted from Magnetic Resonance Angiography (MRA) dataset. Few slices of the MRA are shown in figure (c - f) where the bright structures are the portion of arteries visible in the particular slice. The MRA was obtained from the IXI MRI public dataset [108].

In chapter 4, we also found that the squared magnitude of eigenvalues of Hessian of the distance transform provides a very good response to the centerline of an object. Fast marching method [91] was then used to extract the centerline of a desired branch in between the user specified points. A user interface for selection the endpoints of an artery branch was developed. The extracted centerline of all the branches are shown along with the vessels in figure 6.3.

The geometry based filters extracts only the lumen since the parameters were specifically tuned for the contrast intensity range and the diameters. Calcified plaques may not be large enough to analyze the geometry and are usually excluded as noisy structures. In order to include all possible structures including the arterial wall and any calcifications, we morphologically dilate [58] the centerline uniformly along the length of a desired branch. We used a spherical structural element of radius $3mm$ as it included all of desired artery section without including any extra-arterial calcification. We also used morphologically dilated centerline to segment out lumen, wall, calcified plaques, and the surrounding tissue which is presented in chapter 6. For the segmentation purpose we used a dilation radius of $5mm$ as it provided a better statistical analysis of the voxel intensities.

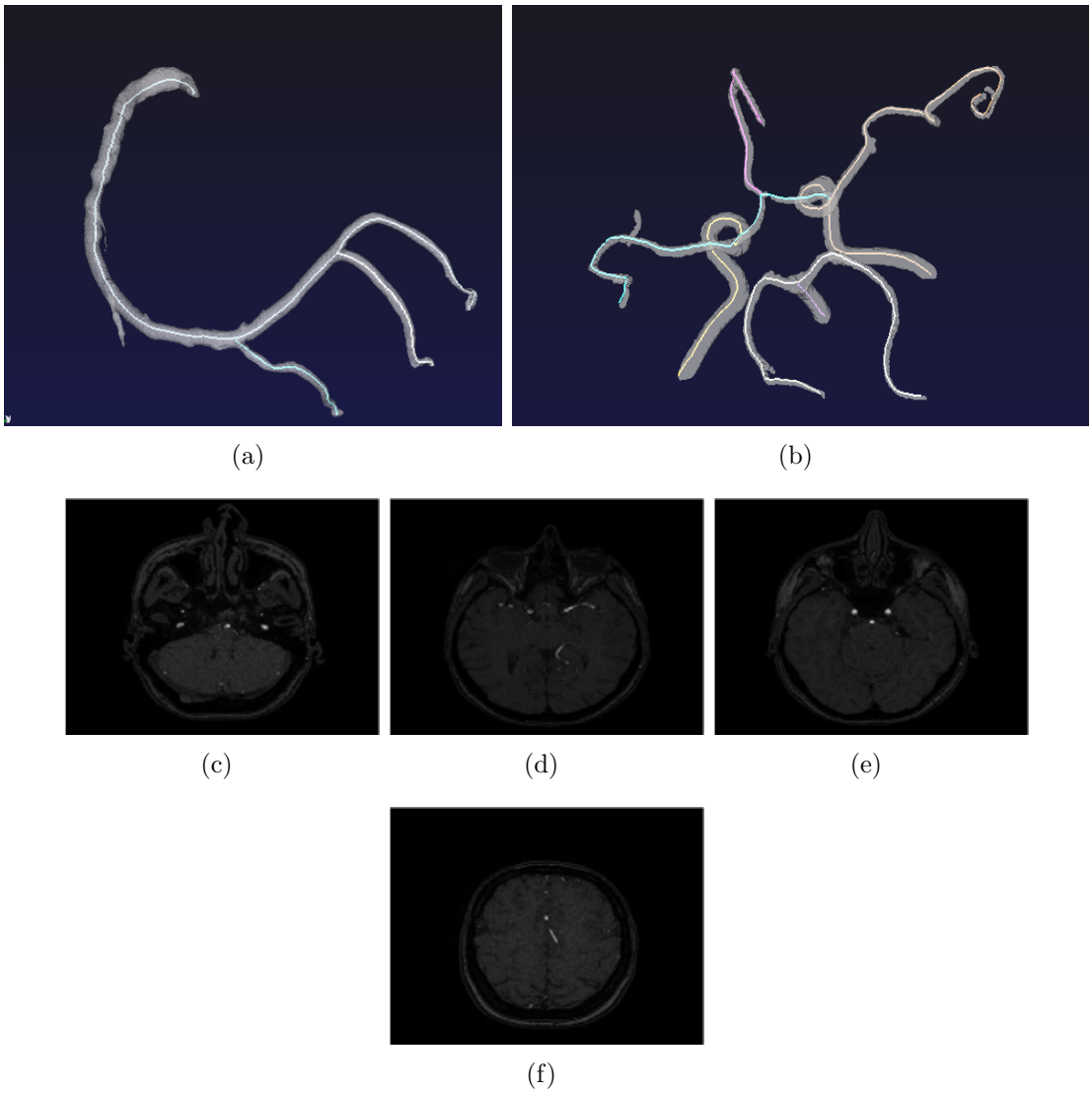

(a) (b)

(c) (d) (e)

(f)

Figure 6.3 Vessels and centerline extracted from a cardiac CT and a brain MRA. (a) Different branches of the RCA with the corresponding centerlines. (b) Different branches of the cerebral arteries the corresponding centerlines. (c, d, e, f) Some of the slices of the MRA used for extracting the cerebral vessels and the centerlines. The arteries appear as the white spots in each slice.

6.3.2 Automatic vessel extraction from the non-contrast-enhanced computed tomography (CAC)

Due to the small size of the arteries and no contrast enhancement in the CAC, we extracted the arteries manually by annotating the centerpoints in the visible sections of the artery, smoothing the centerpoints, and then by morphologically dilating the smooth centerline. In this chapter, however, we compare the calcium quantification obtained in the contrast-enhanced CTA and the non-contrast-enhanced CAC. Therefore we, registered subvolume from the contrast-enhanced CTA with a subvolume extracted from the non-contrast-enhanced CAC and used the registration parameters to transform the automatically extracted centerline in the CTA to obtain a corresponding centerline in the CAC. The centerline was then dilated to include an artery region for further analysis in the non-contrast-enhanced CAC.

The subvolume registration were performed in 2 steps of manual landmark based rough alignment and an automatic non-rigid registration. A landmark point such as artery branch location or the ostium of an artery were identified in both subvolumes which was used to translate the non-contrast-enhanced CAC subvolume to match the contrast-enhanced CTA subvolume. The subvolume in CTA was extracted manually to included all the desired vessels and is the same subvolume used in the automatic extraction of artery by using the vesselness filter. A software tool was developed for manual landmark selection. Since, the contrast-enhanced and non-contrast-enhanced CT are acquired at different time instances, the beating of heart can introduce non-linear differences in the position of arteries captured. Hence the subvolumes were also registered using non-rigid registration method for an accurate transformation of the vessel centerline.

6.3.3 Calcium quantification from contrast-enhanced CTA

The calcium quantification from CTA is made difficult by the contrast enhancement of the lumen which raises the intensity range of the lumen thereby occluding some of the low-density calcium. In chapter 5 we developed an adaptive cutoff threshold and probability

based method to accurately quantify both the high-density as well as low-density calcium along the length of an artery from the CTA which we validate by comparing with the IVUS-VH derived calcium volume. We encourage the readers to refer to chapter 5 for the details of the method.

For comparing with the IVUS-VH derived calcium volume, we obtained 2 different types of calcium quantifications from the morphologically dilated artery voxels in the CTA dataset. First, the calcium was quantified by using a fixed cutoff threshold obtained from the probability density function (PDF) of the voxel intensity histogram. The method for obtaining cutoff in CTA is described in chapter 5. A similar method for the non-contrast-enhanced CT is discussed in this chapter in the following section and illustrated in figure 6.5. Lets refer to the calcium quantified by using this method CTA_{high}. The cutoff threshold is shown by the label "B" in figure 6.4 (a). Any intensity above this cutoff is quantified as calcium. Each dot in the figure represent a voxel intensity and the red curve is the maximum intensity along the length of an artery.

In another method we considered an adaptive cutoff threshold which is different along the length of an artery as shown by the label "A" in figure 6.4 (a). Any voxel with intensity above this threshold is high density calcium. We used the $peakFit$ algorithm developed in chapter 5 for calculating the adaptive cutoff threshold. The adaptive cutoff threshold was then used by the $calcHigh$ algorithm to quantify high-density calcium as discussed in chapter 5. The low-density calcium shown in the green shaded region were also considered in this method. The $probContrast$, and the $calcLow$ algorithms in chapter 5 were used for the quantifying the low-density calcium. Finally the total calcium is obtained by adding the high-density calcium to the low-density at each position of the artery. Let us refer to the total calcium as CTA_{all}. It can be noted from figure 6.4 (a) that the CTA_{high} discards most of the low-density calcium shown by the shaded green region.

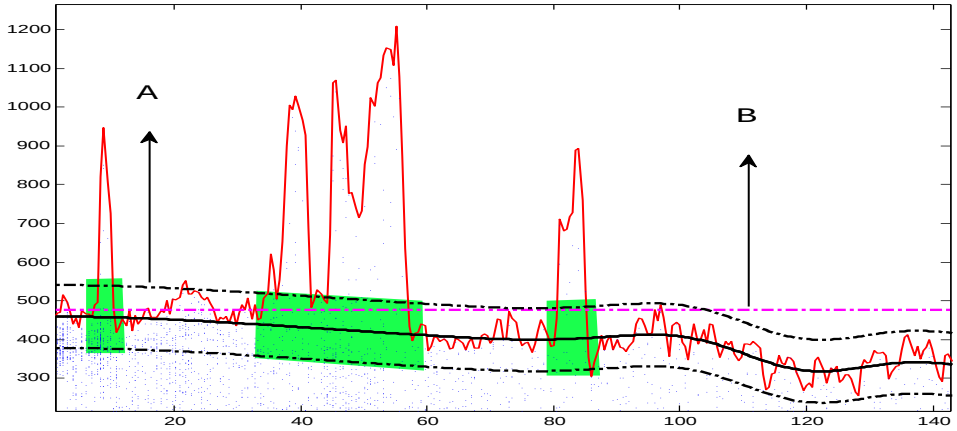

(a)

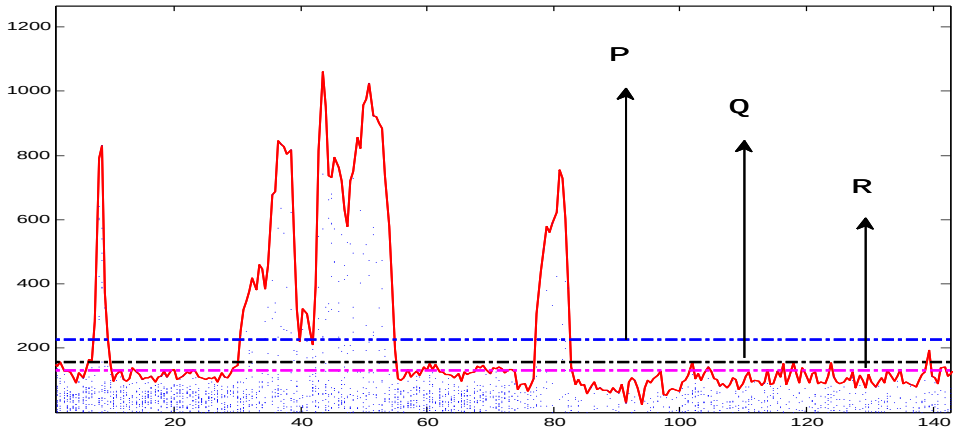

(b)

Figure 6.4 Different calcium quantification methods in the non-contrast-enhanced CT, and the contrast-enhanced CTA. Each dot represent the voxel intensity of an artery plotted along the length of an artery. The red curve in each plot represent the maximum intensity along the length. Figure (a) is the intensity plot for artery extracted form CTA. The label "A" represents the adaptive cutoff developed in chapter 5. Any intensity above "A" are high-density calcium. The shaded region are the regions of low-density calcium. Figure (b) is the intensity plot for artery extracted from CAC. The label "P" is the optimal threshold of 226 HU derived from chapter 3, the label "Q" is individual cutoff threshold for a patient derived from the profile of an artery, and "R" is the conventional threshold of 130 HU unit.

6.3.4 Calcium quantification from non-contrast-enhanced CAC

In chapter 3 we studied the quantification accuracy of the $0.5mm$ and $3.0mm$ slice-thickness reconstructions of the non-contrast enhanced CT (CAC) by comparing them with the IVUS-VH calcium volumes. We found that the $0.5mm$ slice-thickness reconstruction provided better quantification than the $3.0mm$ reconstruction in terms of different statistical parameters. We also suggested that the cutoff should be increased from the conventional threshold of 130 HU to 226 HU to achieve the optimal quantification. Therefore, in this chapter we consider only the comparison of 0.5 mm CAC with the CTA and IVUS-VH scans.

After transformation of the CTA centerline, and its morphological dilation to include voxels around the artery, we used 3 different types of calcium quantification in the non-contrast-enhanced CAC dataset. First, the conventional threshold of 130 HU was used which is labeled "R" in figure 6.4 (b). Second, an optimal cutoff threshold of 226 HU developed in chapter 3 was used which is labeled "Q" in figure 6.4 (b). Finally, we quantified the calcium by using an individual cutoff threshold derived from the voxel intensity distribution of each artery. This is labeled "P" in figure 6.4 (b). Lets refer to the calcium quantified by these three methods as CAC_{130}, CAC_{226}, and CAC_{ind} respectively.

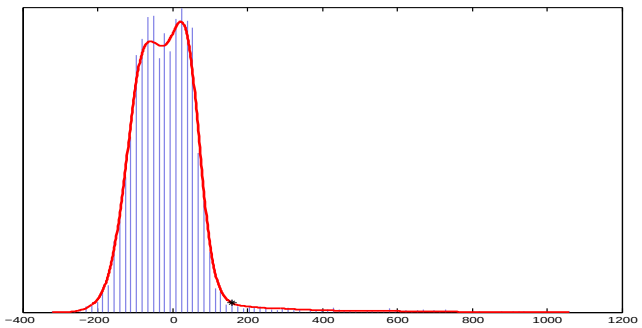

Figure 6.5 The PDF estimation of a non-contrast-enhanced CAC by using Parzen window method. The asterisk at the right end is the cutoff developed by finding a point at which the curve starts to flatten.

The last cutoff threshold differed not only across different patient, but also across dif-

ferent arteries. We do not need a lengthwise adaptive cutoff threshold in the non-contrast-enhanced CAC because unlike the contrast-enhanced CTA the intensity distribution of the lumen does not taper along the distal end of the artery. This can be observed by comparing figures 6.4 (a) and (b). To find the individual cutoff threshold the probability density function (PDF) of the voxel intensities in an artery was estimated by using the Parzen window [98] method. The PDF estimated for an artery is shown as the red curve in figure 6.5. The calcium voxels appears as a shallow tail on the right-most end of the PDF curve. A cutoff point as shown by the black asterisk in figure 6.5 can then be found by calculating the first derivative of the PDF and find the right-most point at which the PDF has required amount of flatness. The cutoff point labeled "P" in figure 6.4 (b) correspond to the cutoff indicated by the asterisk in figure 6.5. This method of cutoff estimation from the PDF is also used in the CTA as a preprocessing step and discussed in detail in chapter 5.

Table 6.1 summarizes a total of 5 different types of calcium quantification considered for comparing to the calcium quantified from IVUS-VH.

Table 6.1 Different calcium quantification methods considered to compare with the IVUS-VH derived calcium volume lengthwise.

Method	CT Type	Description
CTA_{high}	CTA	High-density calcium. Only the intensities above "A" in figure 6.4 (a).
CTA_{all}	CTA	High-density and low-density calcium. Also includes the calcium in the shaded regions in figure 6.4 (a) .
CAC_{130}	CAC	Conventional cutoff threshold of 130 HU. All the intensities above "R" in figure 6.4 (b).
CAC_{226}	CAC	Optimal cutoff threshold derived in chapter 3. All the intensities above "Q" in figure 6.4 (b).
CAC_{ind}	CAC	Individual cutoff threshold derived from the PDF of voxel intensities. All the intensities above "P" in figure 6.4 (b).

6.3.5 Registration of CT with the IVUS-VH for calcium comparison

For a slice-by-slice comparison of calcium volume in the CT and IVUS, these two different modalities should be registered lengthwise at a very fine level. The two different modalities are difficult to align because IVUS-VH provides a very detailed resolution from the interior of an artery while in CT the smallest voxel that can be captured is only $0.5mm$ in side. Further difficulty in registration is added by the fact that in an IVUS-VH we do not have the 3D geometry information of a pixel with respect to an anatomical location. The lengthwise calcium quantifications obtained from the CT volume, the voxels assigned to a centerline location may not necessarily correspond to the frame-by-frame pixels of the IVUS-VH.

Previous studies in computed tomography (CT) and IVUS registration were done specifically for the contrast-enhanced CTA only. Leber et al. for example, registered CT vessel with IVUS by visual comparison by looking at landmarks such as side branches in order to study the accuracy of 64-slice CT in classifying and quantifying plaque volume [59]. Marquering et al. matched IVUS and CTA data manually along the longitudinal views, and semi-automatically registering segmented vessel contours in 2D cross-sectional views [60]. More recently, Qian et al. registered CTA images obtained from 64-slice CT with IVUS/VH by simulating the CTA image from IVUS/VH, and by using mutual information based registration algorithm [61]. All of these works used contrast enhanced CTA volumes. Different from the previous works, we developed a general 2-step process for registering both non-contrast-enhanced CAC and the contrast-enhanced CTA with the IVUS-VH dataset. In the first step we manually perform the visual alignment of the straight vessel views extracted from the IVUS-VH and the CT scans and in the second step we align the calcium curves directly by panning and adjusting the data location.

The manual registration by visually comparing the straight vessel view of the non-contrast-enhanced CAC and the IVUS-VH is discussed in chapter 3. The same process of straight-vessel view extraction and alignment by comparing the landmark is also applicable for the contrast-enhanced CTA. In the following subsection we discuss the automatic curve

alignment done after the manual alignment process.

Automatic calcium curve alignment In chapter 3 we achieved the curve alignment manually by panning one of the curves and its points sideways to match the peaks of the other. Since the manual process can introduce errors, we use an automatic curve alignment in this chapter for aligning lengthwise calcium quantification obtained from chapter 5 with the IVUS-VH derived calcium curve. The alignment of the curve is based on maximizing correlation by sliding a curve on top of another and by realigning the points to different x-axis location to match the target curve. This automated method for curve registration is known as correlation optimized warping (COW) [109]. The COW algorithm registers two curves piecewise by a panning a source, also known as the moving curve over a target curve to maximizes the correlation coefficient between the two. It is similar to manually panning a curve and its points but can be controlled with factors such as maximum horizontal panning thus enabling a fair comparison across different datasets.

Figure 6.6 (a) shows the calcium quantification of the RCA obtained from the IVUS-VH frames and the CTA by using the methods discussed in chapter 5. The red curve is obtained from the IVUS-VH image and treated as the stationary or the target curve. In both IVUS-VH and CTA the quantification was done in an interval of 0.5 mm. In order to improve the accuracy of comparison the calcium were first smoothed by summing at an interval of 3.0 mm length as shown in figure 6.6 (b), and finally the COW algorithm was applied to maximize the correlation coefficient between the two curves. The registered curves are shown in figure 6.6 (c). The same process is applied for comparing non-contrast enhanced (CAC) and the IVUS-VH derived calcium curves.

A similar curve registration was also performed for comparing the lengthwise calcium quantification from non-contrast-enhanced CAC and contrast-enhanced CTA. Therefore comparing the CAC and CTA was done after 3 different registration steps.

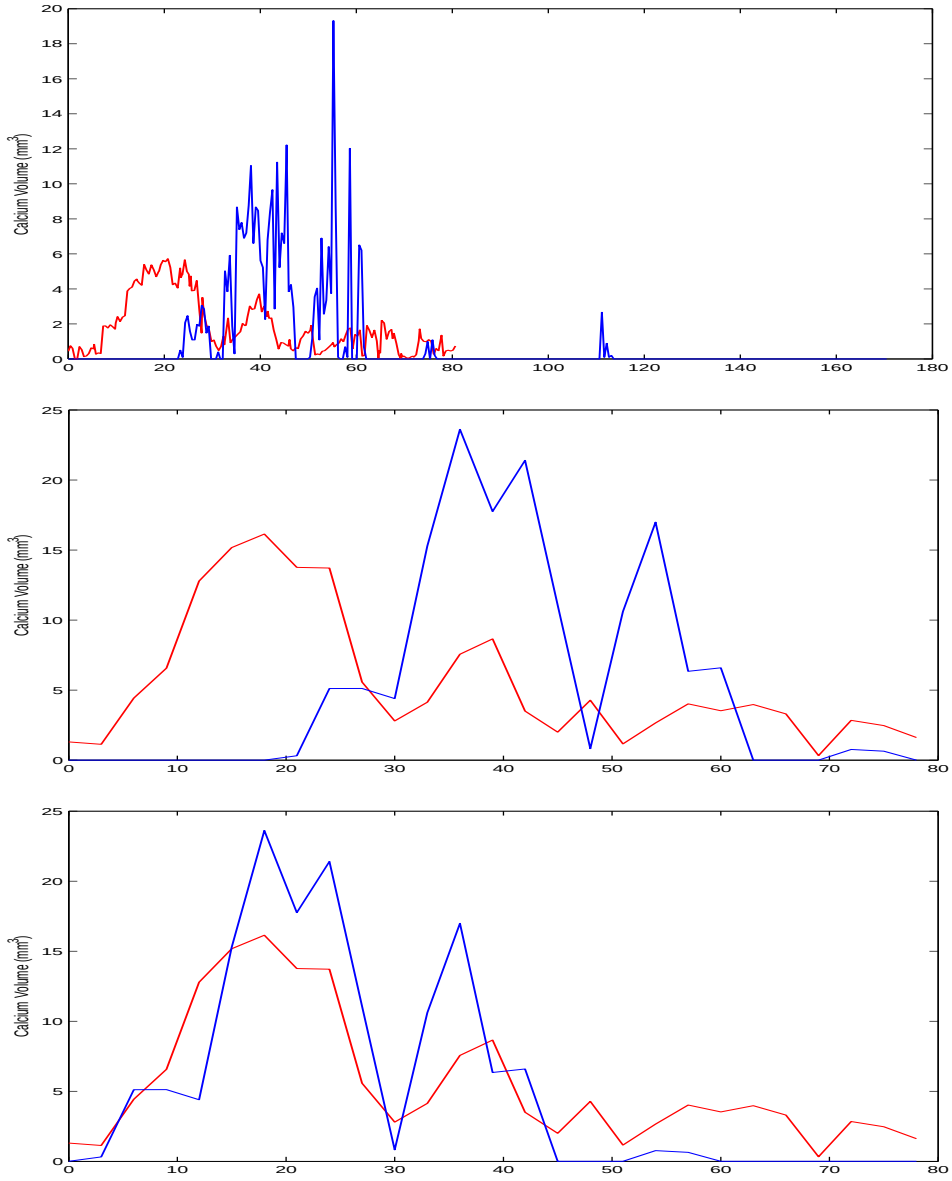

Figure 6.6 Correlation optimized warping for aligning the calcium curves automatically. The red-curve is the calcium quantified from IVUS-VH frames and the blue one is from the CTA volume. Figure (a) shows unregistered curves, (b) shows the smoothing by summing the calcium volume at an 3.0 mm interval for increasing accuracy of comparison and (c) shows the alignment of the curves by applying the correlation optimized warping (COW) algorithm.

6.4 Statistical analysis

We compared 5 different quantification methods in the contrast-enhanced and the non-contrast-enhanced CT by conducting linear regression analysis and calculated the correlation coefficients (r) with the calcium volumes derived from IVUS-VH. These 5 different methods are outlined in table 6.1. Considering the IVUS-VH calcium volume data as ground truth, sensitivity ($sens$), specificity ($spec$), positive predictive value (PPV) and negative predictive value (NPV) assessment were done for each of the 5 quantification methods. In our case, the true positive (tp) is the total number of slices having calcium in both CT and IVUS-VH, the true negative (tn) is the total number of slices without calcified plaques in both the modalities, false positive (fp) is the total number of slices having calcium in the CT but not in the IVUS-VH , and false negative (fn) is the total number of slices having calcium in IVUS-VH images but not in CT . Then, the statistical measures are defined as,

$$sens = \frac{tp}{tp + fn}, \tag{6.1}$$

$$spec = \frac{tn}{tn + fp}, \tag{6.2}$$

$$PPV = \frac{tp}{tp + fp}, \tag{6.3}$$

$$NPV = \frac{tn}{tn + fn}. \tag{6.4}$$

A high value for each of the statistical measures are desired for better accuracy. A compound index based on the correlation coefficient, sensitivity, specificity PPV, and NPV is constructed to compare the accuracy of 5 different quantification methods. Existing methods such as the F1-score combines only the precision and recall [110] which are equivalent to the PPV and the sensitivity in our case. The F1-score takes the harmonic mean of sensitivity and PPV and given by,

$$F1 = \frac{2.PPV.sens}{PPV + sens} \tag{6.5}$$

We construct a similar metric by taking the harmonic mean of the $sens$, $spec$, PPV, and NPV as follows,

$$HM = \frac{4.sens.spec.PPV.NPV}{spec.PPV.NPV + sens.PPV.NPV + sens.spec.PPV + sens.spec.NPV} \tag{6.6}$$

Then a compound index is constructed by putting equal weight on the correlation coefficient r and the harmonic mean HM as follows.

$$M = r \times HM \tag{6.7}$$

Other parameters were also measured for comparing the five different quantification methods. The Bland-Altman analysis [52] was used to find the mean difference in the calcium volume reported by CT and IVUS-VH. For better accuracy a low mean difference is desired since the actual amount of calcium in a patient should be reported same by both the imaging modalities. The total overestimation of calcium by each method was compared with respect to the IVUS-VH. The overestimation or the underestimation are not desired as it can re-assign a patient into a different risk category.

6.5 Results and Discussion

12 patients (8 M and 4 F, age: 60 ± 8.5) undergoing all three of 0.5 mm isotropic non-contrast-enhanced CAC, contrast-enhanced CTA, and the IVUS-VH were studied. Isotropic CAC was obtained using the conventional CAC imaging protocol with no increase in radiation dose. Imaging parameters included: prospective volumetric mode with a tube voltage of 120 kV, tube current of 100 - 550 mA, 0.5 mm detector width. Images were reconstructed using 0.5 mm slice thickness. CTA was acquired prospectively using 60 to 80 ml of intravenous iodinated contrast followed by 30 ml of normal saline flush. Imaging parameters were: tube voltage was 100-120 kV, tube current was 100550 mA, and reconstruction slice thickness was 0.5 mm. IVUS-VH image acquisition and calcium quantification was done in selected

vessels with intermediate to severe diseases as discussed in section 6.2. The isotropic CAC and CTA were registered with IVUS-VH using the 2-steps registration method discussed in section 6.3.5 and the calcium quantification obtained by methods outlined in table 6.1 were compared with the registered IVUS-VH slice-by-slice calcium volume. The calcium volume in the thinner slices were added to obtain volumes of $3.0mm$ artery sections along the artery length. This is illustrated in figure 6.6 (a) and (b) for an artery. Thus a total of 528 calcium volumes from each CT and IVUS-VH were obtained for comparison.

Table 6.2 shows the comparison of these five quantification methods with respect to the statistical measures discussed in section 6.4. The method of calcium quantification is given in the first column. Second column is the CT scan type either contrast-enhanced (CTA) or the non-contrast-enhanced (CAC) from which the quantification was obtained. Third column is the correlation coefficient. Columns $4-7$ are the sensitivity, specificity, PPV, and NPV respectively. Column 8 is the harmonic mean of these four measured obtained by using equation 6.6, column 9 is the final metric obtained by combining the correlation coefficient and the harmonic mean by using equation 6.7. Column 10 gives the overestimation or underestimation of the calcium as compared to the IVUS-VH calcium quantification. A value of overestimation greater than 1 is overestimation and less than 1 indicate underestimation of the calcium volume. A value close to 1 is desired for optimal calcium quantification. The last column is the difference in calcium quantification obtained by using Bland-Altman analysis.

Table 6.2 Comparison of five different calcium quantification obtained from the non-contrast-enhanced, and the contrast-enhanced CT by validating against the IVUS-VH slice-by-slice calcium volume.

Method	Type	r	$sens$	$spec$	PPV	NPV	HM	M	overest	diff. (HU)
CTA_{high}	CTA	0.70	0.68	0.92	0.76	0.89	0.80	0.56	1.04	0.12 ± 4.34
CTA_{all}	CTA	0.76	0.70	0.88	0.77	0.85	0.79	0.60	2.01	-1.64 ± 8.04
CAC_{130}	CAC	0.78	0.95	0.32	0.89	0.56	0.56	0.44	3.50	-5.25 ± 15.11
CAC_{226}	CAC	0.76	0.82	0.60	0.78	0.65	0.70	0.53	2.47	-1.45 ± 10.54
CAC_{ind}	CAC	0.74	0.85	0.57	0.81	0.64	0.70	0.51	2.65	-1.79 ± 12.01

Table 6.2 shows that the metric constructed by combining all the statistical measures is highest (0.59) for the calcium quantification obtained from the contrast-enhanced CTA by using the method CTA_{all}. The calcium quantification method considers both the high-density as well as low-density calcium quantification in the vicinity of the high-density calcium. The high-density calcium are based on the adaptive cutoff threshold and the low-density calcium are quantified based on the probability of calcium in the neighborhood of high-density calcium. Different algorithms are developed for this calcium quantification include the $peakFit$, $calcHigh$, $probContrast$, and $calcLow$ algorithms which are discussed in chapter 5. This method has the very low difference range of $-0.23 \pm 3.65HU$ and the amount of calcium is close to the IVUS-VH level with and underestimation factor of only 0.96.

CTA_{high} which considers only the high-density calcium quantification is the next best method in our ranking. However, since it does not consider the low-density calcium, it underestimates the total calcium volume with a factor of 0.52 and the correlation coefficient is lower than that of the $calc_{all}$. CAC_{130} has the highest correlation coefficient. However this conventional method of calcium quantification from non-contrast-enhanced CAC with the fixed cutoff threshold of 130 HU has an unacceptable specificity of 0.26. The combined metric of $r \times HM$, NPV, overestimation factor, and the difference range are also the worst of all the methods. As indicated by our preliminary study, increasing the threshold of the 0.5 mm CAC to 226 HU (the CAC_{226} method) improved the statistical measure and provided the best quantification among the non-contrast-enhanced quantification method. The individual cutoff threshold based on the probability density function (PDF) of an artery follows very close to the CAC_{226} in most of the statistical parameters.

Based on different statistical parameters discussed in section 6.4, our method of calcium quantification from the contrast-enhanced CTA dataset by considering both the high-density and low-density calcium was the most accurate and reliable method for calcium quantification among all the methods considered. Among the non-contrast-enhanced quantification methods, the quantification done with the cutoff threshold of 226 provided the best results. A comparison of the best CAC and CTA methods are shown in figure 6.7. The figures on

the left shows the linear regression of the lengthwise CT calcium volume with the slice-by-slice IVUS-VH calcium volume. The figures on right show the Bland-Altman analysis of the calcium quantification. Each point in the figure represents calcium volume in a 3.00 mm long section of CT or IVUS.

We also compared the calcium quantification by CAC with respect to the calcium quantified with the CTA. We had a total of 23 patients with CTA and CAC data out of which 4 were excluded due to noise or artifact. For example, figure 6.8 shows the CTA dataset with high noise and stent which is a metallic mesh inserted to support a weak artery from inside the artery. Therefore we compared a dataset of 19 patients (13 M, 6 F, age: 58 ± 9). Three major arteries, right coronary artery (RCA), left anterior descending (LAD), and left circumflex (LCX) arteries were chosen from the automatically extracted set of arteries in CTA. The arteries extracted were registered to obtain corresponding arteries from CAC as discussed in section 6.3.4 and further calcium curve alignment was done for a fair comparison by using curve registration as discussed in section 6.3.5. Some of the arteries with higher registration errors were excluded from comparison resulting in a total of 1701 slices at $3mm$ interval for comparison.

A comparison of all the CAC quantification methods with the CTA_{all} method is shown in table 6.3. The CAC_{226} method for calcium quantification by using the fixed cutoff threshold of 226 HU was closest to our calcium quantification method by using the contrast-enhanced CTA based on different statistical measures shown in the table . The linear regression and bland-Altman analysis between the two methods is shown in figure 6.9.

Table 6.3 Comparison of 3 different calcium quantification obtained from the non-contrast-enhanced with the calcium quantification obtained from the CTA by using the CTA_{all} method.

Method	Type	r	$sens$	$spec$	PPV	NPV	HM	M	overest	diff. (HU)
CAC_{130}	CAC	0.80	0.48	0.93	0.44	0.94	0.62	0.49	1.59	-5.19 ± 25.77
CAC_{226}	CAC	0.83	0.79	0.91	0.87	0.84	0.85	0.70	1.14	-0.71 ± 15.28
CAC_{ind}	CAC	0.82	0.69	0.92	0.78	0.89	0.81	0.66	1.34	-2.01 ± 19.18

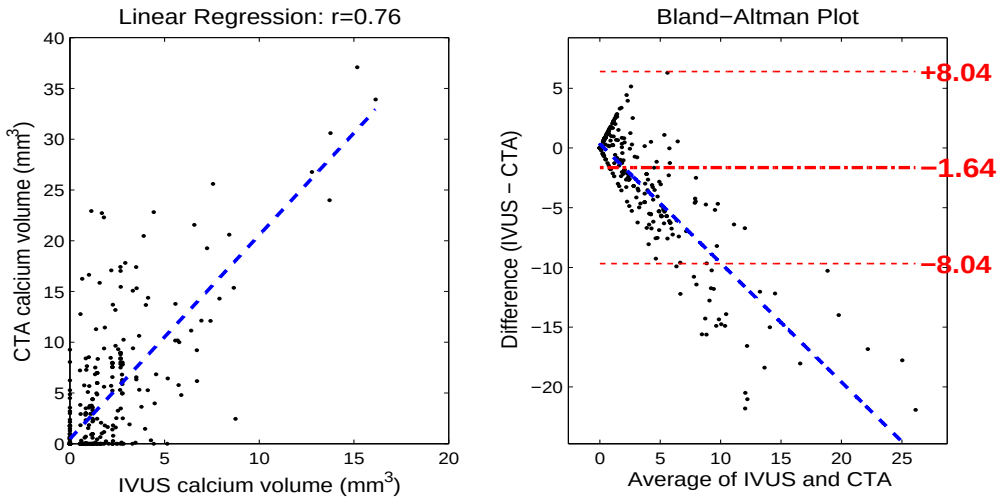

(a)

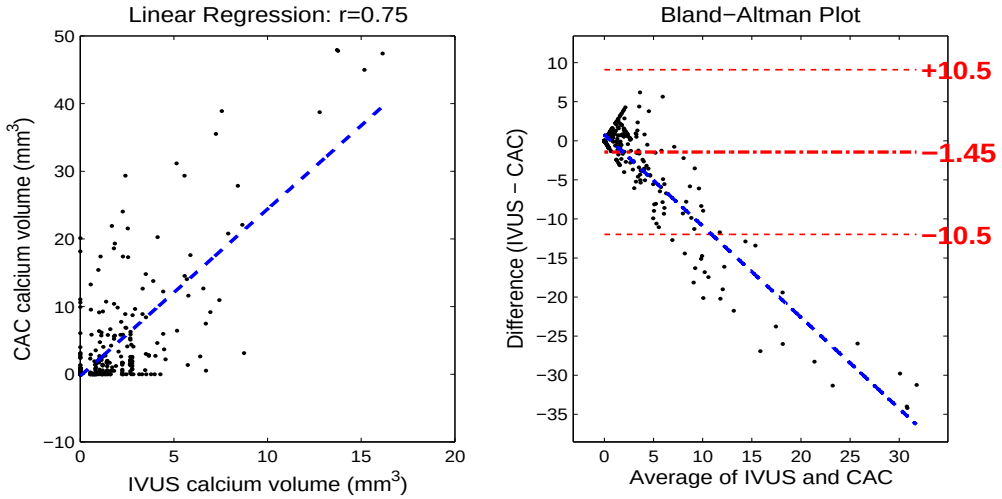

(b)

Figure 6.7 (a) Linear regression analysis, and the Bland-Altman analysis of the calcium quantification obtained from CTA by using the $calc_{all}$ method with the calcium obtained from IVUS-VH. (b) Linear regression analysis, and the Bland-Altman analysis of the calcium quantification obtained from CAC by using the $calc_{226}$ method with the calcium obtained from IVUS-VH. Only 2 methods among the 5 method considered are shown as these provided the best quantification for CTA and CTA.

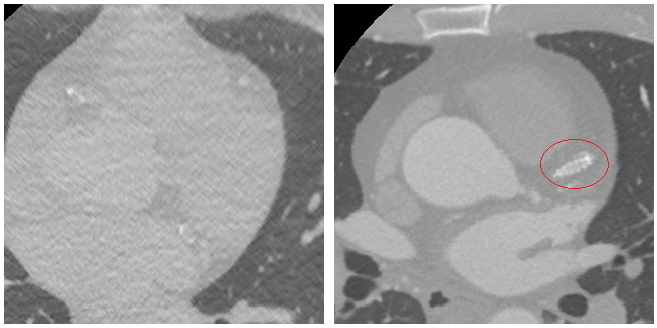

(a) (b)

Figure 6.8 Examples of some CTA data excluded from comparison. (a) CT volume with high noise and (b) with a stent in the Left Anterior Descending (LAD) artery shown by the red ellipse.

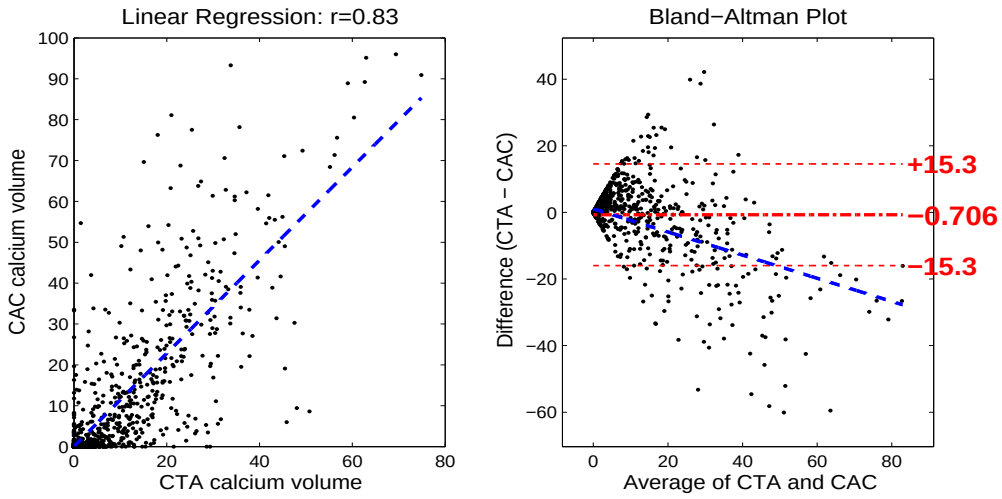

Figure 6.9 A comparison of calcium quantification between CAC by using the CAC_{226} method and CTA by using CTA_{all} method.

In this section we validated different calcium quantification obtained from the contrast-enhanced CTA by using 2 different methods and from the non-contrast-enhanced CAC by using 3 different methods against the IVUS-VH derived calcium volumes. Both the CAC and CTA had a reconstruction slice thickness of 0.5 mm. The comparison was done at a very detailed level of $3.0mm$ artery length sections in terms of correlation coefficient, sensitivity, specificity, npv, ppv, calcium overestimation, and difference range in quantification. We found that the calcium quantification done by considering both the high-density as well as low-density calcified voxels from the contrast-enhanced CTA had the highest accuracy of all the methods. The accuracy was found to be better than that of the non-contrast-enhanced CAC by using different cutoff thresholds.

In order for the quantification to be accurate it is important to quantify the low-density calcium in the periphery of high-density calcium. The low-density calcium usually have their intensity range overlapped with the intensity range of the contrast material flowing in the lumen and hence is difficult to be identified. A complete method for calcium quantification based on an adaptive cutoff threshold for high-density quantification and a probability based method for quantifying low-density method has been developed in chapter 5.

CHAPTER 7

SEGMENTATION BY USING THE EXPECTATION-MAXIMIZATION ALGORITHM

In this chapter we develop a method to segment the morphologically dilated voxels obtained in chapter 5 to high density calcium, high probability contrast region, artery wall, and the surrounding myocardial tissue. The method is based on the combination of our high-density calcium extraction algorithm discussed in chapter 5 and the expectation maximization (EM) algorithm [26] which calculates the probability of each voxel belonging to one of the possible classes of tissue considered. The described method of segmentation accurately separates high-density calcified plaque and the artery lumen from the background myocardial tissue and is useful in the visualization of the calcium, lumen and any narrowing or stenosis of the lumen. First, we describe the EM algorithm in the following section and the use of EM algorithm for tissue segmentation is subsequent section.

7.1 The Expectation-maximization (EM) algorithm

The Expectation-Maximization (EM) algorithm developed by Dempster et al. [26] estimates the probability density function (PDF) of an observed random variables as a sum of the PDFs of underlying components. The number of components should be specified as an input, and the PDFs of the components are usually assumed to be of a parametric form such as Gaussian, Poisson distribution etc. The application of EM algorithm is appropriate for segmentation in our case for two reasons. First, we know the number of tissue components in a selected subvolume of the CTA. The majority of voxels in the segmented and dilated arteries are either contrast filled lumen or the surrounding tissue including arterial wall and the myocardial tissue. Hence the intensity profile of the artery can be modeled as a mixture of (PDFs) for each of the tissue components. Second, the EM algorithm returns the mem-

bership probability of a voxel to each class of tissues instead of "hard" assignment to the classes. Due the limited resolution, different tissue types can be captured in a single voxel in a CTA. Therefore, for a segmentation of low resolution structures such as coronary arteries a "soft" clustering approach of the EM algorithm is preferred.

In the next two sections, we briefly describe the derivation of the EM algorithm and formulate its application to our problem of separating tissue types in a morphologically dilated subvolume of a CTA. For a complete and detailed analysis of the EM algorithm, please refer to Dempster et al. [26].

7.2 The Expectation Maximization (EM) algorithm

Let $X = \{x_1, x_2, ..., x_N\}$ be a set of the observed arterial HU intensity values in a desired subvolume of the CTA, then we need to find functions that are most likely to generate the observed data X. Assuming the functions can be described in terms of some parameters θ, the total likelihood of the data being generated from the functions can be written as,

$$L(\theta) = \sum_{z} P(X, Z|\theta) \tag{7.1}$$

where Z is set of the two classes that are most likely to generate each data point x_i. $P(X, Z|\theta)$ is the joint probability of the observed data X and the unobserved or latent variable Z. The joint probability and the corresponding likelihood function can be expanded as follows,

$$L(\theta) = \sum_{z} P(X|Z, \theta)P(Z|\theta), \tag{7.2}$$

where $P(X|Z, \theta)$ is the probability density function (PDF) of observed data given a particular class and $P(Z|\theta)$ is the probability of occurrence of each class. The sum of probability over all classes gives the total probability. Equation 7.2 describes the PDF of observed data as the linear mixture of the PDF of each class weighted by $P(Z|\theta)$.

The EM algorithm finds the parameters (θ) that maximize the log-likelihood function

($l(\theta)$) by applying the Expectation or E-step and the Maximization or M-steps alternatively. The function $l(\theta)$ is the logarithm and the lower bound of the likelihood function $L(\theta)$. Therefore, the maximization of $L(\theta)$ may be replaced by the maximization of $l(\theta)$. The E-step in each iteration calculates the following conditional likelihood given the current estimates of the parameters ($\theta^{(t)}$),

$$l(\theta|\theta^{(t)}) = \sum_{z} P(Z|X, \theta^{(t)}) lnP(X, Z|\theta), \tag{7.3}$$

The idea of the E-step or the equation 7.3 is to calculate the log-likelihood of the data at each step. However, since the new parameters are unknown, equation 7.3 finds the expected or the average log-likelihood over the classes Z given the observed data X and the current parameter estimate $\theta^{(t)}$. Representing this conditional expectation as $\mathbf{E}_{Z|X,\theta^{(t)}}$, equation 7.3 can be written as,

$$l(\theta|\theta^{(t)}) = \mathbf{E}_{Z|X,\theta^{(t)}}(lnP(X, Z|\theta)). \tag{7.4}$$

The M-step finds a new set of parameters (θ) that maximizes the log-likelihood $l(\theta|\theta^{(t)})$ at each iteration step,

$$\arg\max_{\theta} l(\theta|\theta^{(t)}). \tag{7.5}$$

The EM algorithm is started by guessing an initial set of parameters. The E-step finds the conditional expectation and the M-step finds a new set of parameters to maximize the expectation. The algorithm maximize the likelihood incrementally and is guaranteed to converge. The likelihood function can have multiple local maxima and the parameter estimation can stop at a local maximum without giving the optimal result. In practice, the convergence to the global maximum can be checked by applying the EM multiple times with different random parameters [26].

7.3 EM algorithm formulation for the arterial tissue separation

The latent variable $Z = \{z_1, z_2, ..., z_N\}$ in our case represent the three different classes of voxels. In the next section we provide a discussion that the assumption of 3 components after the removal of high-density calcium and low-intensity lung voxel provides optimal segmentation. Hench, for each x_i in X, the corresponding $z_i \in Z$ represents the membership of x_i to one of the classes $z_i = 1$, $z_i = 2$ or, $z_i = 3$. For simplicity, we will assume the PDFs of all the classes follow Gaussian distribution. Therefore, the probability that the observed variable X is generated from these classes are,

$$P(x_i|z_i = k) = \mathcal{N}(x_i; \mu_k, \sigma_k^2), k \in \{1, 2, 3\} \tag{7.6}$$

where,

$$\mathcal{N}(x_i; \mu_k, \sigma_k^2) = \frac{1}{\sqrt{2\pi\sigma_k^2}} e^{-\frac{1}{2}(\frac{x-\mu}{\sigma})^2}, \tag{7.7}$$

μ_k and σ_k^2 are the mean and covariance of Gaussian functions corresponding to the class $k \in \{1, 2, 3\}$. Then the E-step becomes,

$$l(\theta|\theta^{(t)}) = \sum_{i=1}^{N} \sum_{k=1}^{2} P(z_i = k|x_i, \theta_k^{(t)}) ln P(Z_k|\theta) P(x_i|z_i = k|\theta_k), \tag{7.8}$$

Since the current parameter estimates $\theta^{(t)}$ is a known quantity, the membership probability $P(z_i = k|x_i, \theta_k^{(t)})$ can be calculated by using the Bayesian rule as follows,

$$P(z_i = k|x_i, \theta_k^{(t)}) = \frac{P(x_i|z_i = k, \theta_k^{(t)}) P(Z_k|\theta_k^{(t)})}{\sum_{k=1}^{2} P(x_i|z_i = k, \theta_k^{(t)}) P(Z_k|\theta_k^{(t)})}, \tag{7.9}$$

where $P(x_i|z_i = k|\theta_k^{(t)}) = \mathcal{N}(x_i; \mu_k^{(t)}), \sigma_k^{2(t)}$. The quantity $P(Z_k|\theta_k^{(t)})$ represents probability of occurrence of each class. Since we have three distinct classes of voxels the following equation holds true for the probability,

$$\sum_{k=1}^{3} P(Z_k|\theta_k^{(t)}) = 1. \tag{7.10}$$

Let $P(Z_1|\theta_k^{(t)}) = \lambda_1$, $P(Z_2|\theta_k^{(t)}) = \lambda_2$ and, $P(Z_3|\theta_k^{(t)}) = \lambda_3$. Since, the λ is also an unknown parameter, the E-step begins by guessing the parameters $\theta^{(t)} = (\mu_1, \sigma_1^2, \mu_2, \sigma_2^2, \mu_3, \sigma_3^2, \lambda_1, \lambda_2, \lambda_3)$, and calculates the membership probabilities $M_{i,k} = P(z_i = k|x_i, \theta_k^{(t)})$ from the current parameter estimates at each step. The M-step finds a new set of parameters that maximize the equation 7.8. Substituting $M_{i,k} = P(z_i = k|x_i, \theta_k^{(t)})$, $P(x_i|z_i = k|\theta_k) = \mathcal{N}(x_i; \mu_k), \sigma_k^2$, and $P(Z_k|\theta_k) = \lambda_k$, the equation 7.8 can be written as,

$$l(\theta|\theta^{(t)}) = \sum_{i=1}^{N}\sum_{k=1}^{3} M_{i,k}(ln\lambda_k + ln(\frac{1}{\sqrt{2\pi\sigma_k^2}} e^{-\frac{1}{2}(\frac{x-\mu}{\sigma})^2})). \tag{7.11}$$

By setting the partial derivatives $\frac{\partial l(\theta|\theta^{(t)})}{\partial \mu_k}$, $\frac{\partial l(\theta|\theta^{(t)})}{\partial \sigma_k}$, and $\frac{\partial l(\theta|\theta^{(t)})}{\partial \lambda_k}$ to 0, the M-step finds the new parameters that maximize equation 7.11 as follows,

$$\mu_k^{(t+1)} = \frac{\sum_i^N M_{i,k}^{(t)} x_i}{\sum_i^N M_{i,k}^{(t)}}, \tag{7.12}$$

$$\sigma_k^{2(t+1)} = \frac{\sum_i^N M_{i,k}^{(t)} (x_i - \mu_k^{(t+1)})^2}{\sum_i^N M_{i,k}^{(t)}}, \tag{7.13}$$

$$\lambda_k^{(t+1)} = \frac{1}{N}\sum_{i}^{N} M_{i,k}^{(t)}. \tag{7.14}$$

The EM algorithm starts with an initial guess of parameters $\theta^{(0)} = (\mu_k^{(0)}, \sigma_k^{2(0)}, \lambda_k^{(0)})$ and alternates between E and M step until the difference $\theta^{(t+1)} - \theta^{(t)}$ is small enough. The difference may be determined empirically.

7.4 Application of the Expectation-maximization (EM) algorithm for arterial segmentation

We apply the EM algorithm to the morphologically dilated centerline obtained from section 5.2.2 in chapter 5. Since the centerline was dilated to include 4 different types of tissues, viz., the lumen, calcium, arterial wall, and the myocardial tissue, we can assume 4 different components in applying the EM algorithm. However, assumption of a parametric density function for the calcium often introduce inaccuracy as the frequency of calcified voxels is variable and is typically much less compared to the voxels of other tissues. In some cases, the dilation also includes a small portion of lung voxels which appears separately in the left part of the profile and can be another source of inaccuracy. Therefore we remove the calcium and the lung tissues and apply EM assuming 3 components.

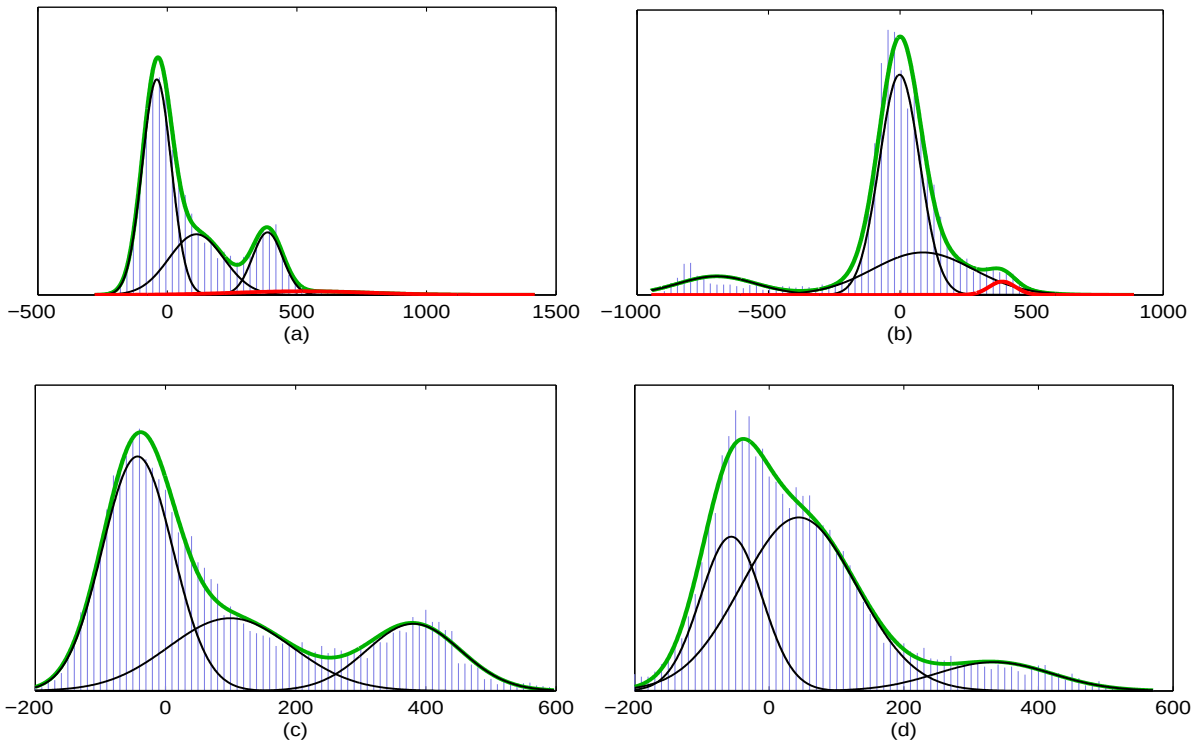

Figure 7.1 EM algorithm applied assuming different numbers of underlying Gaussian components. (a), (b) 4 Gaussian components. (c), (d) 3 Gaussian components after the removal of high-density calcium and the low intensity lung tissues.

Figure 7.1 (a), and (b), show the EM algorithm applied for 4 different components assuming Gaussian distribution for each. The green curve is the sum of all component and the overall estimate of the probability density function of all the voxels. The black curves represent the first 3 components, and the red is the component corresponding to calcium. As can be observed from both (a) and (b), the Gaussian component for calcium expands across the entire profile. The fourth Gaussian component in the figure does not resolve calcium accurately as the calcified voxels occur only within higher intensity range. Furthermore, the frequency of calcium is typically less compared to other tissue and it is difficult to assume any parametric model for the calcium. Nonetheless, we have developed a method for accurately quantifying calcium in the preceding sections. Therefore, we remove any high density calcium voxels with intensities greater than the cutoff $Ymean + 2.5 \times sd$, where sd is the standard deviation of the peak contrast intensity and $Ymean$ is the mean peak contrast intensity calculated by using the $peakFit$ algorithm described in chapter 5.

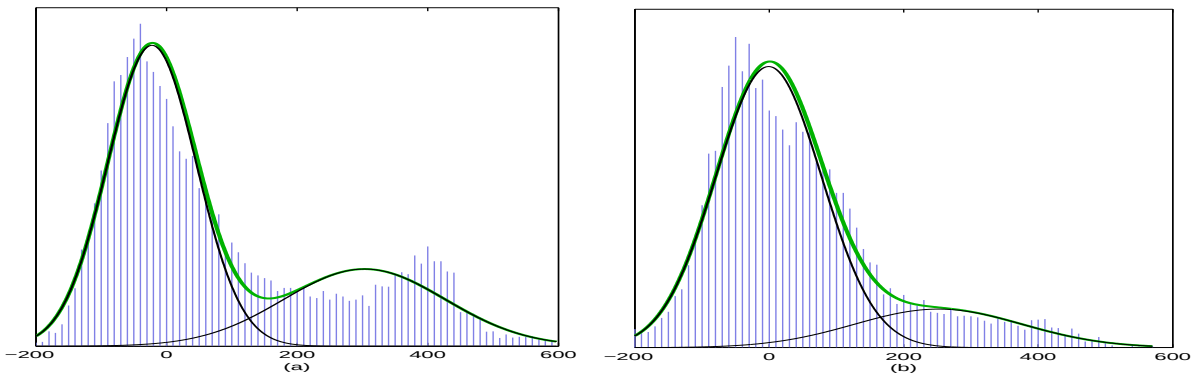

Figure 7.2 EM algorithm applied assuming 2 Gaussian components is not accurate for segmenting the contrast.

Figure 7.1 (b) shows a first Gaussian component centered near the $-500HU$ which appears due to the inclusion of a small portion of lung voxels. Since the lung mostly contains air, it has a low attenuation value and appears black in the CT scan with large negative HU values. To remove the lung tissue we use a fixed threshold of -200 HU such that any voxels below this threshold are removed. After removal of any high-density calcium and the lung tissues, we apply the EM by assuming 3 Gaussian components. Figure 7.1 (c), and (d) shows

the application of EM for 3 Gaussian components after removing the high-density calcium and the lung voxels from figures (a), and (b) respectively. The first 2 components do not always separate the myocardial tissue and the arterial walls completely but are required for accurately resolving the third component. For example, figure 7.2 (a) and (b) shows the EM algorithm for the same profiles of figure 7.1 (a), and (b) but considering 2 components only. In both profiles and all of the CTA profiles of our data set 3 components provides a better fit and in most of them the arterial wall and myocardial tissues are resolved fairly accurate.

The segmentation of each component on the CTA slice are visualized in figure 7.3, which shows different sections of a right coronary artery (RCA) and a section of the left main artery. The blue area in the segmentation corresponds to the contrast or the lumen, the dark green regions surrounding the blue lumen correspond to the arterial wall, the light green region are the myocardial tissue voxels included in the dilation and red regions correspond to calcium. Figure 7.3 (a) shows the RCA branching out from the Aorta, (b) shows a cross section of a highly-calcified region in the RCA, (c) shows a narrowed portion or stenosis in the artery; the wall in this section appears to be thickened probably due to deposition of non-calcified plaque, (d) shows a normal segment of the RCA, (e) shows the left main artery with some calcification, and (f) shows the magnified view of the calcified section in (b). The high-density calcium voxels seen as bright-red in the magnified view were obtained by applying the cutoff from the $peakFit$ algorithm described in chapter 5. Since the low-density calcium surrounds the high-density calcium as shown in the surface plot in figure 5.10, we obtained the low-density calcium voxels by using the 8-connected neighbors of the high-density calcium voxels. Any low-density voxels overlapping with high-probability arterial wall, or contrast components obtained from the EM algorithm were removed. The low-density calcium voxels can be seen as light red voxels surrounding the high-density calcium in figure 7.3 (f).

Figure 7.4 shows the visualization of the segmented artery by using the ray casting method [68]. The semi-transparent outer layer is the dilated portion of the artery including both the myocardial tissue and the arterial wall. The blue solid region in the center is the contrast or the lumen and the red patches are the high-density calcium. There are

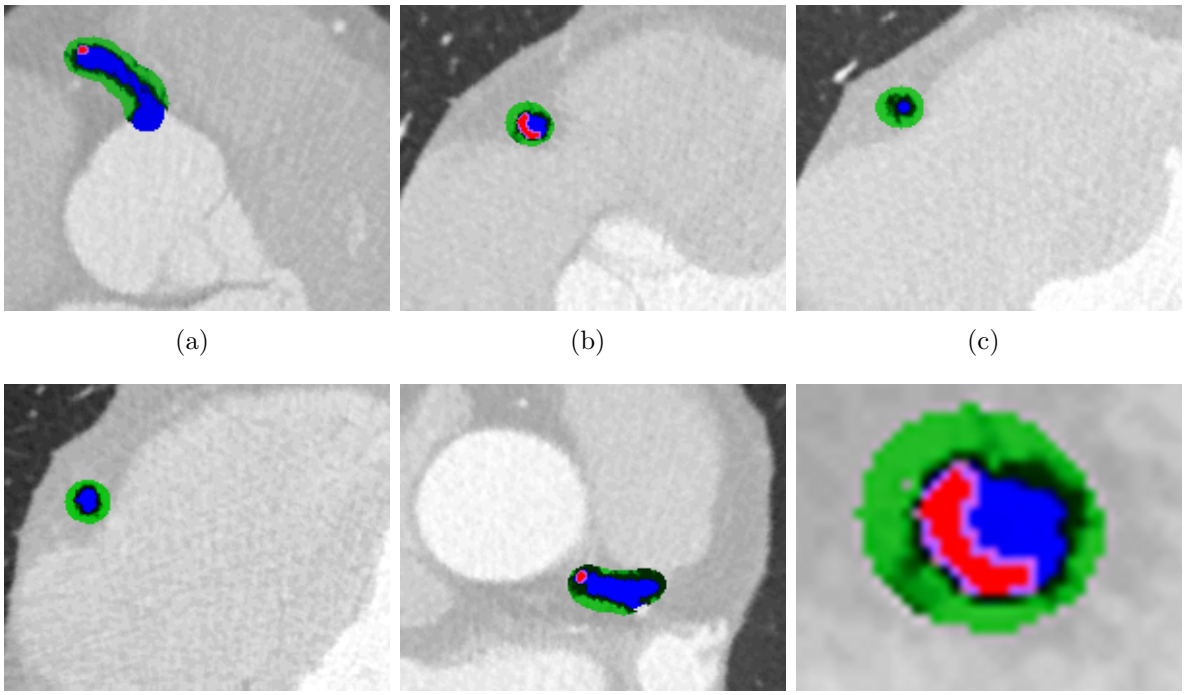

(a) (b) (c)

(d) (e) (f)

Figure 7.3 Segmentation done by applying the EM algorithm and the *peakFit* algorithm described in chapter 5. Blue component in the center is the lumen, red is calcium, dark green surrounding the lumen is the arterial wall, and light green on the periphery is myocardial tissue. Figure (a) shows RCA branching out from the Aorta, (b) a highly-calcified region in the RCA, (c) a stenosis in the artery (d) a normal segment of the RCA, (e)the left main artery with some calcification, and (f) magnified view of the calcified section in (b).

few possibilities for improvement to the segmentation. For example, the accuracy of the segmented lumen can further be increased by combining the EM segmentation with geometry based approaches such as the Frangi's method [76] discussed in chapter 4. Also, a very accurate centerline of the artery can be extracted by applying our centerline extraction algorithm discussed in chapter 4 to the segmented lumen. Based on the distance of a voxel from the centerline, the low-density calcium can be separated more accurately from the lumen. We plan to address these in our future works.

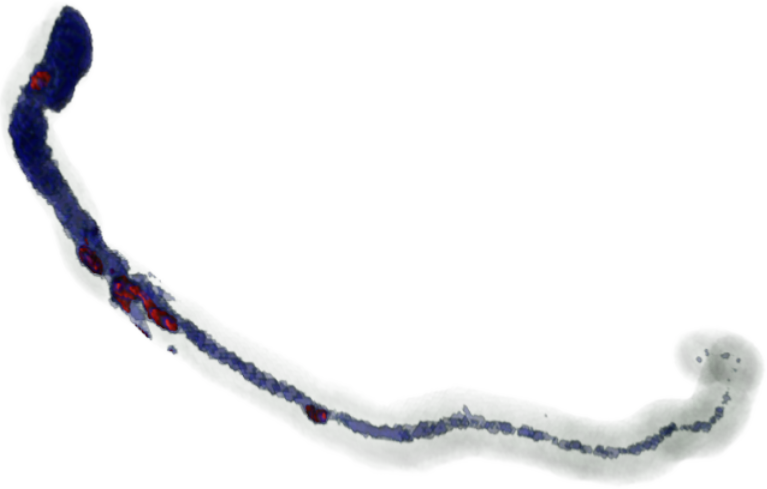

Figure 7.4 Visualization of the segmented artery by using the ray casting method. The inner solid region is the lumen and the red patches are the high density calcium. The outer semi-transparent layer consists of both myocardial tissue and the arterial wall.

CHAPTER 8

SUMMARY AND FUTURE WORKS

In this dissertation we studied the coronary artery calcium quantification by using contrast-enhanced computed tomography angiography (CTA). The CTA constructs a volumetric images of an anatomical region of a body based on the attenuation of x-ray passed through the body. The CTA procedure is done by injecting a patient with a dye known as contrast material. The dye is opaque to x-ray and therefore helps to visualize the blood flow path such as artery and different chambers of heart which otherwise are not readily visible. Therefore, CTA is performed to assess the morphology of the arteries in order to rule out the blockage or abnormalities in the artery. The CTA is done in conjunction with another scan for measuring the total coronary artery calcium (CAC) which does not involve any contrast dye injection. Calcium quantification is an important clinical procedure as the presence of calcium in the coronary arteries is highly indicative of the presence or the future risk of coronary artery diseases. The CTA itself is not suitable for assessing a particular calcium as the contrast material has attenuation value similar to some of the low-density calcium. As a result, the intensity range of some of the calcium and contrast range overlap with each other thus resulting in inaccurate calcium quantification. We developed an accurate method for calcium quantification from the contrast-enhanced CTA thus obviating the need for a scan done solely for quantification of the calcium. As a result, the total time required for the CT scan procedure and the patient's exposure to x-ray radiation is reduced.

In chapter 3 of the dissertation, we compared the calcium quantification accuracy of 0.5 mm slice thickness and 3.0 mm slice thickness reconstructions width from the non-contrast-enhanced CAC scan by comparing against the intravascular ultrasound with radiofrequency analysis of backscatter data (IVUS-VH). We studied the effect of different cutoff thresholds in the accuracy of calcium quantification and found a range of thresholds that are optimal for

quantification in both the 3.0 mm and 0.5 mm slice thickness volumes. Although the 3.0 mm slice thickness reconstruction, and the cutoff threshold of 130 HU are used conventionally for calcium quantification, our result showed that the 0.5 mm with higher cutoff thresholds provides better quantification accuracy. The results in this work can be clinically useful in deciding an appropriate threshold for calcium quantification. Although our method of calcium quantification from CTA provides a better accuracy than both of the CAC based quantification, the 0.5 mm reconstruction width can be implemented in clinics until calcium quantification from the CTA becomes a practice.

In chapters 4, and 5 we develop the methodologies for extracting calcium from a desired vessel in a CTA volume. In chapter 4 we implemented a method to extract artery information by analyzing their shape using eigenvalues of the Hessian matrix. Then, eigenvalues of Hessian was also used to find the centerline by first finding the distance transform on the interior of the extracted artery. The centerline extracted in chapter 4 was used for finding a set of voxels located at its certain distance (3 to 5 mm). These voxels were then analyzed statistically for finding an appropriate cutoff threshold for quantifying high-density calcium in chapter 5. Algorithm for finding low-density calcium in the vicinity of high-density calcium was also developed. The total calcium was then the sum of both high-density and low-density calcium.

In chapter 5 we also presented the software developed for quantification of calcium in contrast-enhanced CTA. The software was developed for facilitating the automatic and manual extraction of arteries from CTA and CAC, visualizing, registering the CTA, CAC and IVUS-VH, and for quantifying calcium in the CTA as well as CAC. With minimal effort the software can be scaled to a fully working clinical application for calcium quantification.

However, IVUS-VH produces acoustic shadow behind the lining of dense calcium which may result in an inaccurate quantification of calcium. The IVUS-VH uses sound wave reflected from different tissue to construct their image. The sound wave emitted from the IVUS-VH catheter may not penetrate the calcium lining in the arterial wall and the tissue underneath the calcium lining appears as a dark area in the IVUS-VH image known as

the acoustic shadow. The possible under-estimation of calcium volume due to the shadow might be another factor contributing to the apparent over-estimation by CT quantification of calcium. Other limitations of the study may be due to the manual extraction of vessels and manual registration using visual alignment and curve panning. The manual steps might alter the accuracy of calcium quantification and registration.

In chapter 6 we validated our calcium quantification method against the calcium quantified from the IVUS-VH images by comparing the calcium volumes on a slice-by-slice basis. The proposed calcium quantification method from CTA outperformed the best calcium quantification by using 0.5 mm CAC as compared to the IVUS-VH thus making our method preferable to the conventional method of calcium quantification using non-contrast-enhanced CT scan.

In chapter 7, we used the expectation maximization method for segmenting the dilated region around centerline into lumen, artery wall, and the myocardial tissue. The method first used the algorithm developed in chapter 5 to exclude all the high-density calcium in order produce an accurate segmentation of the remaining tissues.

Therefore in this dissertation, we study the quantification accuracy of conventional methods from the CAC, developed a method to accurately quantify calcium from CTA thus contributing to an accurate quantification of calcium which is very important for better risk assessment of a patient. Since the CTA based quantification was found to be more accurate than the CAC based quantification, the first phase of scan can be eliminated, thus reducing time, and most importantly the radiation exposure in performing the scans. The software tools developed for the dissertation can serve as a prototype for developing a full clinical application. In addition, we also developed an algorithm for segmenting the calcified plaque, lumen, artery wall and the surrounding tissue, which in general can be applied for separating any tissue types.

Topics of future interest include, further refinement of segmentation developed in chapter 6. For instance, the geometry based vessel extraction done in chapter 4 can be combined with the expectation maximization based segmentation to delineate lumen. The algorithms

developed can also be extended to quantify and segment non-calcified plaques as the resolution and image quality of the CTA improves in future.

One of the limitations of the current study is the validation by using IVUS-VH. IVUS-VH produces acoustic shadow behind the lining of dense calcium and may result in an inaccurate quantification of calcium. Therefore, further improvement in the quantification accuracy may be achieved by using machine learning technique to quantify calcium based on the spatial distribution of calcium learned from actual histological study. Another limitation could be due to the number of data available for validation. Although we have tried to curb the problem by extracting multiple slices from a single artery, a larger validation study is desirable for better predictability.

REFERENCES

[1] "Your coronary arteries," http://my.clevelandclinic.org/heart/heart-blood-vessels/coronary-arteries.aspx, accessed: Oct. 25, 2012.

[2] "What is angina?" http://www.nhlbi.nih.gov/health/health-topics/topics/angina/, accessed: Oct. 25, 2012.

[3] M. Naghavi, E. Falk, H. S. Hecht, M. J. Jamieson, S. Kaul, D. Berman, Z. Fayad, M. J. Budoff, J. Rumberger, T. Z. Naqvi *et al.*, "From vulnerable plaque to vulnerable patientpart iii: executive summary of the screening for heart attack prevention and education (shape) task force report," *The American journal of cardiology*, vol. 98, no. 2, pp. 2–15, 2006.

[4] "What is a heart attack ?" http://www.nhlbi.nih.gov/health/health-topics/topics/heartattack/, accessed: Oct. 25, 2012.

[5] M. Naghavi, P. Libby, E. Falk, S. W. Casscells, S. Litovsky, J. Rumberger, J. J. Badimon, C. Stefanadis, P. Moreno, G. Pasterkamp *et al.*, "From vulnerable plaque to vulnerable patient a call for new definitions and risk assessment strategies: part i," *Circulation*, vol. 108, no. 14, pp. 1664–1672, 2003.

[6] "Myocardial ischemia," http://www.mayoclinic.com/health/myocardial-ischemia/DS01179, accessed: Oct. 25, 2012.

[7] B. D. K. D. G. V. Anuja Nair, M Pauliina Margolis, "Automated coronary plaque characterization with intravascular ultrasound backscatter: Ex vivo validation," *EuroIntervention*, vol. 3, no. 1, pp. 113–120, 2007.

[8] M. J. Budoff, L. J. Shaw, S. T. Liu, S. R. Weinstein, T. P. Mosler, P. H. Tseng, F. R. Flores, T. Q. Callister, P. Raggi, and D. S. Berman, "Long-term prognosis associated

with coronary calcificationobservations from a registry of 25,253 patients," *Journal of the American College of Cardiology*, vol. 49, no. 18, pp. 1860–1870, 2007.

[9] R. Salzer, *Biomedical Imaging: Principles and Applications*. Wiley, 2012, vol. 1.

[10] A. S. Agatston, W. R. Janowitz, F. J. Hildner, N. R. Zusmer, M. Viamonte Jr, and R. Detrano, "Quantification of coronary artery calcium using ultrafast computed tomography," *Journal of the American College of Cardiology*, vol. 15, no. 4, pp. 827–832, 1990.

[11] R. L. McClelland, H. Chung, R. Detrano, W. Post, and R. A. Kronmal, "Distribution of coronary artery calcium by race, gender, and age results from the multi-ethnic study of atherosclerosis (mesa)," *Circulation*, vol. 113, no. 1, pp. 30–37, 2006.

[12] D. E. Bild, R. Detrano, D. Peterson, A. Guerci, K. Liu, E. Shahar, P. Ouyang, S. Jackson, and M. F. Saad, "Ethnic differences in coronary calcification the multi-ethnic study of atherosclerosis (mesa)," *Circulation*, vol. 111, no. 10, pp. 1313–1320, 2005.

[13] R. Detrano, A. D. Guerci, J. J. Carr, D. E. Bild, G. Burke, A. R. Folsom, K. Liu, S. Shea, M. Szklo, D. A. Bluemke *et al.*, "Coronary calcium as a predictor of coronary events in four racial or ethnic groups," *New England Journal of Medicine*, vol. 358, no. 13, pp. 1336–1345, 2008.

[14] A. Sarwar, L. J. Shaw, M. D. Shapiro, R. Blankstein, U. Hoffman, R. C. Cury, S. Abbara, T. J. Brady, M. J. Budoff, R. S. Blumenthal *et al.*, "Diagnostic and prognostic value of absence of coronary artery calcification," *JACC: Cardiovascular Imaging*, vol. 2, no. 6, pp. 675–688, 2009.

[15] K. Akram, R. E. ODonnell, S. King, H. R. Superko, A. Agatston, and S. Voros, "Influence of symptomatic status on the prevalence of obstructive coronary artery disease in patients with zero calcium score," *Atherosclerosis*, vol. 203, no. 2, pp. 533–537, 2009.

[16] V. Y. Cheng, N. E. Lepor, H. Madyoon, S. Eshaghian, A. L. Naraghi, and P. K. Shah, "Presence and severity of noncalcified coronary plaque on 64-slice computed tomographic coronary angiography in patients with zero and low coronary artery calcium," *The American journal of cardiology*, vol. 99, no. 9, pp. 1183–1186, 2007.

[17] J. M. Otton, J. T. Lønborg, D. Boshell, M. Feneley, A. Hayen, N. Sammel, K. Sesel, L. Bester, and J. McCrohon, "A method for coronary artery calcium scoring using contrast-enhanced computed tomography," *Journal of Cardiovascular Computed Tomography*, vol. 6, no. 1, pp. 37–44, 2012.

[18] M. Teßmann, F. Vega-Higuera, B. Bischoff, J. Hausleiter, and G. Greiner, "Automatic detection and quantification of coronary calcium on 3d ct angiography data," *Computer Science-Research and Development*, vol. 26, no. 1-2, pp. 117–124, 2011.

[19] M. Teßmann, F. V. Higuera, B. Bischoff, J. Hausleiter, and G. Greiner, "Robust automatic calcium scoring for ct coronary angiography." in *Bildverarbeitung für die Medizin*, 2010, pp. 430–434.

[20] S. C. Saur, H. Alkadhi, L. Desbiolles, G. Székely, and P. C. Cattin, "Automatic detection of calcified coronary plaques in computed tomography data sets," in *Medical Image Computing and Computer-Assisted Intervention–MICCAI 2008*. Springer, 2008, pp. 170–177.

[21] G. Mühlenbruch, J. E. Wildberger, R. Koos, M. Das, T. G. Flohr, M. Niethammer, C. Wei, R. W. Günther, and A. H. Mahnken, "Coronary calcium scoring using 16-row multislice computed tomography: nonenhanced versus contrast-enhanced studies in vitro and in vivo," *Investigative radiology*, vol. 40, no. 3, pp. 148–154, 2005.

[22] C. Hong, C. R. Becker, U. J. Schoepf, B. Ohnesorge, R. Bruening, and M. F. Reiser, "Coronary artery calcium: Absolute quantification in nonenhanced and contrast-enhanced multi–detector row ct studies1," *Radiology*, vol. 223, no. 2, pp. 474–480, 2002.

[23] B. Glodny, B. Helmel, T. Trieb, C. Schenk, B. Taferner, V. Unterholzner, A. Strasak, and J. Petersen, "A method for calcium quantification by means of ct coronary angiography using 64-multidetector ct: very high correlation with agatston and volume scores," *European radiology*, vol. 19, no. 7, pp. 1661–1668, 2009.

[24] K. T. Bae, "Technical aspects of contrast delivery in advanced ct," *Applied Radiology*, vol. 32, no. 12; SUPP, pp. 12–19, 2003.

[25] K. Nasu, E. Tsuchikane, O. Katoh, D. G. Vince, R. Virmani, J.-F. Surmely, A. Murata, Y. Takeda, T. Ito, M. Ehara *et al.*, "Accuracy of in vivo coronary plaque morphology assessmenta validation study of in vivo virtual histology compared with in vitro histopathology," *Journal of the American College of Cardiology*, vol. 47, no. 12, pp. 2405–2412, 2006.

[26] A. P. Dempster, N. M. Laird, and D. B. Rubin, "Maximum likelihood from incomplete data via the em algorithm," *Journal of the Royal Statistical Society. Series B (Methodological)*, pp. 1–38, 1977.

[27] A. Dhungel, Z. Qian, G. Vazquez, S. Rinehart, M. Weeks, and S. Voros, "Optimal cutoff threshold for calcium quantification in isotropic ct calcium scans by validating against registered intravascular ultrasound with radiofrequency backscatter," in *Engineering in Medicine and Biology Society (EMBC), 2012 Annual International Conference of the IEEE*. IEEE, 2012, pp. 4982–4985.

[28] A. Dhungel, Z. Qian, S. Rinehart, K. Bhatt, W. Odeh, J. Gustavo, V. Figueroa, M. Weeks, and S. Voros, "Validation of isotropic coronary artery calcium measurements using 320-detector row ct against intravascular ultrasound with radiofrequency backscatter," *Journal of the American College of Cardiology*, vol. 59, no. 13s1, pp. E165–E165, 2012.

[29] A. Dhungel, Z. Qian, S. Rinehart, K. Bhatt, W. Odeh, M. Weeks, and S. Voros, "Coronary artery calcium quantification on 320-detector row ct reconstructed with

0.5 mm slice thickness correlates better with ivus/vh, compared to 3.0 mm reconstruction slice thickness," *Journal of Cardiovascular Computed Tomography*, vol. 6, no. 4, Supplement, pp. S8–S9, 2012, abstracts of the 7th Annual Scietific Meeting of the Society of Cardiovascular Computed Tomography. [Online]. Available: http://www.sciencedirect.com/science/article/pii/S1934592512002158

[30] A. Dhungel, Z. Qian, M. Weeks, J. Lee, V. Varghese, R. Pitts, W. Odeh, G. Vazquez, and S. Rinehart, "A novel calcium quantification method with adaptive cutoff in contrast-enhanced coronary ct angiography," *Journal of Cardiovascular Computed Tomography*, vol. 7, no. 3, Supplement, pp. S54–S55, 2013, abstracts of the 8th Annual Scientific Meeting of the Society of Cardiovascular Computed Tomography. [Online]. Available: http://www.sciencedirect.com/science/article/pii/S1934592513003651

[31] A. Dhungel and M. Weeks, "Performance measurement for a wavelet transform-based video compression," in *Proceedings of the 49th Annual Southeast Regional Conference*. ACM, 2011, pp. 216–220.

[32] A. Dhungel and M. Weeks, "Study of multi-scale temporal extension and minkowski pooling for MSSIM," in *Communications and Information Technologies (ISCIT), 2010 International Symposium on*. IEEE, 2010, pp. 887–890.

[33] D. Agarwal, S. Wilf, A. Dhungel, and S. K. Prasad, "Acceleration of bilateral filtering algorithm for manycore and multicore architectures," in *Parallel Processing (ICPP), 2012 41st International Conference on*. IEEE, 2012, pp. 78–87.

[34] T. Q. Callister, B. Cooil, S. P. Raya, N. J. Lippolis, D. J. Russo, and P. Raggi, "Coronary artery disease: improved reproducibility of calcium scoring with an electron-beam ct volumetric method." *Radiology*, vol. 208, no. 3, pp. 807–814, 1998.

[35] R. Detrano, X. Kang, P. Mahaisavariya, W. Tang, A. Colombo, S. Molloi, D. Garner, and S. Nickerson, "Accuracy of quantifying coronary hydroxyapatite with electron beam tomography," *Investigative radiology*, vol. 29, no. 8, pp. 733–738, 1994.

[36] N. van der Bijl, R. M. Joemai, J. Geleijns, J. J. Bax, J. D. Schuijf, A. de Roos, and L. J. Kroft, "Assessment of agatston coronary artery calcium score using contrast-enhanced ct coronary angiography," *American Journal of Roentgenology*, vol. 195, no. 6, pp. 1299–1305, 2010.

[37] B. Bischoff, C. Kantert, T. Meyer, M. Hadamitzky, S. Martinoff, A. Schömig, and J. Hausleiter, "Cardiovascular risk assessment based on the quantification of coronary calcium in contrast-enhanced coronary computed tomography angiography," *European Heart Journal–Cardiovascular Imaging*, vol. 13, no. 6, pp. 468–475, 2012.

[38] S. Voros and Z. Qian, "Agatston score tried and true: By contrast, can we quantify calcium on cta?" *Journal of Cardiovascular Computed Tomography*, vol. 6, no. 1, pp. 45–47, 2012.

[39] M. A. Gülsün and H. Tek, "Robust vessel tree modeling," in *Medical Image Computing and Computer-Assisted Intervention–MICCAI 2008*. Springer, 2008, pp. 602–611.

[40] W. A. Barrett and E. N. Mortensen, "Interactive live-wire boundary extraction," *Medical Image Analysis*, vol. 1, no. 4, pp. 331–341, 1997.

[41] Y. Y. Boykov and M.-P. Jolly, "Interactive graph cuts for optimal boundary & region segmentation of objects in nd images," in *Computer Vision, 2001. ICCV 2001. Proceedings. Eighth IEEE International Conference on*, vol. 1. IEEE, 2001, pp. 105–112.

[42] G. Slabaugh and G. Unal, "Graph cuts segmentation using an elliptical shape prior," in *Image Processing, 2005. ICIP 2005. IEEE International Conference on*, vol. 2. IEEE, 2005, pp. II–1222.

[43] W. E. Lorensen and H. E. Cline, "Marching cubes: A high resolution 3d surface construction algorithm," in *ACM Siggraph Computer Graphics*, vol. 21, no. 4. ACM, 1987, pp. 163–169.

[44] D. Vukadinovic, T. van Walsum, R. Manniesing, S. Rozie, R. Hameeteman, T. T. de Weert, A. van der Lugt, and W. J. Niessen, "Segmentation of the outer vessel wall of the common carotid artery in cta," *Medical Imaging, IEEE Transactions on*, vol. 29, no. 1, pp. 65–76, 2010.

[45] D. Vukadinovic, T. van Walsum, S. Rozie, T. de Weert, R. Manniesing, A. van der Lugt, and W. Niessen, "Carotid artery segmentation and plaque quantification in cta," in *Biomedical Imaging: From Nano to Macro, 2009. ISBI'09. IEEE International Symposium on.* IEEE, 2009, pp. 835–838.

[46] R. Malladi, J. A. Sethian, and B. C. Vemuri, "Shape modeling with front propagation: A level set approach," *Pattern Analysis and Machine Intelligence, IEEE Transactions on*, vol. 17, no. 2, pp. 158–175, 1995.

[47] J. Friedman, T. Hastie, and R. Tibshirani, "Additive logistic regression: a statistical view of boosting (with discussion and a rejoinder by the authors)," *The annals of statistics*, vol. 28, no. 2, pp. 337–407, 2000.

[48] M. de Bruijne, B. van Ginneken, M. A. Viergever, and W. J. Niessen, "Interactive segmentation of abdominal aortic aneurysms in cta images," *Medical Image Analysis*, vol. 8, no. 2, pp. 127–138, 2004.

[49] T. F. Cootes, C. J. Taylor, D. H. Cooper, and J. Graham, "Active shape models-their training and application," *Computer vision and image understanding*, vol. 61, no. 1, pp. 38–59, 1995.

[50] S. D. Olabarriaga, M. Breeuwer, and W. J. Niessen, "Segmentation of abdominal aortic aneurysms with a non-parametric appearance model," in *Computer Vision and Mathematical Methods in Medical and Biomedical Image Analysis.* Springer, 2004, pp. 257–268.

[51] D. Terzopoulos and K. Fleischer, "Deformable models," *The Visual Computer*, vol. 4, no. 6, pp. 306–331, 1988.

[52] D. G. Altman and J. M. Bland, "Measurement in medicine: the analysis of method comparison studies," *The statistician*, pp. 307–317, 1983.

[53] A. Criminisi, K. Juluru, and S. Pathak, "A discriminative-generative model for detecting intravenous contrast in ct images," in *Medical Image Computing and Computer-Assisted Intervention–MICCAI 2011*. Springer, 2011, pp. 49–57.

[54] J. R. Romero, S. K. Alexander, S. Baid, S. Jain, and M. Papadakis, "The geometry and the analytic properties of isotropic multiresolution analysis," in *Advances in Computational Mathematics, special issue on Mathematical Imaging*. DUSSAUD, 2009.

[55] M. Papadakis, B. G. Bodmann, S. K. Alexander, D. Vela, S. Baid, A. A. Gittens, D. J. Kouri, S. D. Gertz, S. Jain, J. R. Romero *et al.*, "Texture-based tissue characterization for high-resolution ct scans of coronary arteries," *Communications in Numerical Methods in Engineering*, vol. 25, no. 6, pp. 597–613, 2009.

[56] M. de Bruijne, "A pattern classification approach to aorta calcium scoring in radiographs," in *Computer Vision for Biomedical Image Applications*. Springer, 2005, pp. 170–177.

[57] M. Kass, A. Witkin, and D. Terzopoulos, "Snakes: Active contour models," *International journal of computer vision*, vol. 1, no. 4, pp. 321–331, 1988.

[58] W. R. Gonzalez RC, *Digital image processing*. Prentice Hall, 2002, vol. 2.

[59] A. W. Leber, A. Becker, A. Knez, F. von Ziegler, M. Sirol, K. Nikolaou, B. Ohnesorge, Z. A. Fayad, C. R. Becker, M. Reiser *et al.*, "Accuracy of 64-slice computed tomography to classify and quantify plaque volumes in the proximal coronary systema comparative study using intravascular ultrasound," *Journal of the American College of Cardiology*, vol. 47, no. 3, pp. 672–677, 2006.

[60] H. A. Marquering, J. Dijkstra, Q. J. Besnehard, J. P. Duthé, J. D. Schuijf, J. J. Bax, and J. H. Reiber, "Coronary ct angiography: Ivus image fusion for quantitative plaque

and stenosis analyses," in *Medical imaging*. International Society for Optics and Photonics, 2008, pp. 69 181G–69 181G.

[61] Z. Qian, G. Vazquez, and S. Voros, "Intermodal registration of cta and ivus-vh, and its application on cta-based plaque composition analysis," in *Biomedical Imaging: From Nano to Macro, 2011 IEEE International Symposium on*. IEEE, 2011, pp. 419–423.

[62] J. Martin Bland and D. Altman, "Statistical methods for assessing agreement between two methods of clinical measurement," *The lancet*, vol. 327, no. 8476, pp. 307–310, 1986.

[63] M. Coffin and S. Sukhatme, "Receiver operating characteristic studies and measurement errors," *Biometrics*, pp. 823–837, 1997.

[64] M. Greiner, D. Pfeiffer, and R. Smith, "Principles and practical application of the receiver-operating characteristic analysis for diagnostic tests," *Preventive veterinary medicine*, vol. 45, no. 1, pp. 23–41, 2000.

[65] T. Sharir, D. S. Berman, P. B. Waechter, J. Areeda, P. B. Kavanagh, J. Gerlach, X. Kang, and G. Germano, "Quantitative analysis of regional motion and thickening by gated myocardial perfusion spect: normal heterogeneity and criteria for abnormality," *Journal of Nuclear Medicine*, vol. 42, no. 11, pp. 1630–1638, 2001.

[66] J. Dehmeshki, X. Ye, H. Amin, M. Abaei, X. Lin, and S. D. Qanadli, "Volumetric quantification of atherosclerotic plaque in ct considering partial volume effect," *Medical Imaging, IEEE Transactions on*, vol. 26, no. 3, pp. 273–282, 2007.

[67] C. Li, C. Xu, C. Gui, and M. D. Fox, "Distance regularized level set evolution and its application to image segmentation," *Image Processing, IEEE Transactions on*, vol. 19, no. 12, pp. 3243–3254, 2010.

[68] S. D. Roth, "Ray casting for modeling solids," *Computer graphics and image processing*, vol. 18, no. 2, pp. 109–144, 1982.

[69] "Vtk - the visualization toolkit," http://www.vtk.org/, accessed: May 18, 2013.

[70] W. E. Lorensen and H. E. Cline, "Marching cubes: A high resolution 3d surface construction algorithm," in *ACM Siggraph Computer Graphics*, vol. 21, no. 4. ACM, 1987, pp. 163–169.

[71] G. M. Nielson and B. Hamann, "The asymptotic decider: resolving the ambiguity in marching cubes," in *Proceedings of the 2nd conference on Visualization'91*. IEEE Computer Society Press, 1991, pp. 83–91.

[72] E. K. Chong and S. H. Zak, *An introduction to optimization*. John Wiley & Sons, 2013, vol. 76.

[73] D. Marr and E. Hildreth, "Theory of edge detection," *Proceedings of the Royal Society of London. Series B. Biological Sciences*, vol. 207, no. 1167, pp. 187–217, 1980.

[74] C. Lorenz, I.-C. Carlsen, T. M. Buzug, C. Fassnacht, and J. Weese, "Multi-scale line segmentation with automatic estimation of width, contrast and tangential direction in 2d and 3d medical images," in *CVRMed-MRCAS'97*. Springer, 1997, pp. 233–242.

[75] Y. Sato, S. Nakajima, N. Shiraga, H. Atsumi, S. Yoshida, T. Koller, G. Gerig, and R. Kikinis, "Three-dimensional multi-scale line filter for segmentation and visualization of curvilinear structures in medical images," *Medical image analysis*, vol. 2, no. 2, pp. 143–168, 1998.

[76] A. F. Frangi, W. J. Niessen, K. L. Vincken, and M. A. Viergever, "Multiscale vessel enhancement filtering," in *Medical Image Computing and Computer-Assisted Interventation*MICCAI98*. Springer, 1998, pp. 130–137.

[77] T. Lindeberg, "Edge detection and ridge detection with automatic scale selection," *International Journal of Computer Vision*, vol. 30, no. 2, pp. 117–156, 1998.

[78] H. Blum *et al.*, "A transformation for extracting new descriptors of shape," *Models for the perception of speech and visual form*, vol. 19, no. 5, pp. 362–380, 1967.

[79] F.-E. Wolter and K.-I. Friese, "Local and global geometric methods for analysis, interrogation, reconstruction, modification and design of shape," in *Computer Graphics International, 2000. Proceedings.* IEEE, 2000, pp. 137–151.

[80] H. Xia and P. G. Tucker, "Distance solutions for medial axis transform," in *Proceedings of the 18th International Meshing Roundtable.* Springer, 2009, pp. 247–265.

[81] A. Rosenfeld and J. L. Pfaltz, "Sequential operations in digital picture processing," *Journal of the ACM (JACM)*, vol. 13, no. 4, pp. 471–494, 1966.

[82] M. W. Jones, J. A. Baerentzen, and M. Sramek, "3d distance fields: A survey of techniques and applications," *Visualization and Computer Graphics, IEEE Transactions on*, vol. 12, no. 4, pp. 581–599, 2006.

[83] R. Fabbri, L. D. F. Costa, J. C. Torelli, and O. M. Bruno, "2d euclidean distance transform algorithms: A comparative survey," *ACM Computing Surveys (CSUR)*, vol. 40, no. 1, p. 2, 2008.

[84] A. Meijster, J. B. Roerdink, and W. H. Hesselink, "A general algorithm for computing distance transforms in linear time," in *Mathematical morphology and its applications to image and signal processing.* Springer, 2002, pp. 331–340.

[85] C. R. Maurer Jr, R. Qi, and V. Raghavan, "A linear time algorithm for computing exact euclidean distance transforms of binary images in arbitrary dimensions," *Pattern Analysis and Machine Intelligence, IEEE Transactions on*, vol. 25, no. 2, pp. 265–270, 2003.

[86] "Matlab version 7.6.0.324(r2008a)," natick, Massachusetts: The MathWorks Inc., 2008.

[87] L. D. Cohen and R. Kimmel, "Global minimum for active contour models: A minimal path approach," *International journal of computer vision*, vol. 24, no. 1, pp. 57–78, 1997.

[88] H. Li and A. Yezzi, "Vessels as 4-d curves: Global minimal 4-d paths to extract 3-d tubular surfaces and centerlines," *Medical Imaging, IEEE Transactions on*, vol. 26, no. 9, pp. 1213–1223, 2007.

[89] M. A. Gülsün and H. Tek, "Robust vessel tree modeling," in *Medical Image Computing and Computer-Assisted Intervention–MICCAI 2008*. Springer, 2008, pp. 602–611.

[90] E. W. Dijkstra, "A note on two problems in connexion with graphs," *NUMERISCHE MATHEMATIK*, vol. 1, no. 1, pp. 269–271, 1959.

[91] J. A. Sethian, "A fast marching level set method for monotonically advancing fronts," *Proceedings of the National Academy of Sciences*, vol. 93, no. 4, pp. 1591–1595, 1996.

[92] R. Kimmel and J. Sethian, "Fast marching methods for robotic navigation with constraints," *Center for Pure and Applied Mathematics Report, University of California, Berkeley*, 1996.

[93] D. Lesage, E. D. Angelini, I. Bloch, and G. Funka-Lea, "A review of 3d vessel lumen segmentation techniques: Models, features and extraction schemes," *Medical image analysis*, vol. 13, no. 6, pp. 819–845, 2009.

[94] M. Schaap, C. T. Metz, T. van Walsum, A. G. van der Giessen, A. C. Weustink, N. R. Mollet, C. Bauer, H. Bogunović, C. Castro, X. Deng *et al.*, "Standardized evaluation methodology and reference database for evaluating coronary artery centerline extraction algorithms," *Medical Image Analysis*, vol. 13, no. 5, pp. 701–714, 2009.

[95] C. Xu and J. L. Prince, "Snakes, shapes, and gradient vector flow," *Image Processing, IEEE Transactions on*, vol. 7, no. 3, pp. 359–369, 1998.

[96] C. Bauer and H. Bischof, "A novel approach for detection of tubular objects and its application to medical image analysis," in *Pattern Recognition*. Springer, 2008, pp. 163–172.

[97] M. Naghavi, E. Falk, H. S. Hecht, M. J. Jamieson, S. Kaul, D. Berman, Z. Fayad, M. J. Budoff, J. Rumberger, T. Z. Naqvi *et al.*, "From vulnerable plaque to vulnerable patientpart iii: executive summary of the screening for heart attack prevention and education (shape) task force report," *The American journal of cardiology*, vol. 98, no. 2, pp. 2–15, 2006.

[98] E. Parzen, "On estimation of a probability density function and mode," *The annals of mathematical statistics*, vol. 33, no. 3, pp. 1065–1076, 1962.

[99] R. O. Duda, P. E. Hart, and D. G. Stork, *Pattern classification*. John Wiley & Sons, 2012.

[100] S. J. Sheather and M. C. Jones, "A reliable data-based bandwidth selection method for kernel density estimation," *Journal of the Royal Statistical Society. Series B (Methodological)*, pp. 683–690, 1991.

[101] B. U. Park and J. S. Marron, "Comparison of data-driven bandwidth selectors," *Journal of the American Statistical Association*, vol. 85, no. 409, pp. 66–72, 1990.

[102] Z. Botev, J. Grotowski, and D. Kroese, "Kernel density estimation via diffusion," *The Annals of Statistics*, vol. 38, no. 5, pp. 2916–2957, 2010.

[103] M. C. Jones, J. S. Marron, and S. J. Sheather, "A brief survey of bandwidth selection for density estimation," *Journal of the American Statistical Association*, vol. 91, no. 433, pp. 401–407, 1996.

[104] N.-B. Heidenreich, A. Schindler, and S. Sperlich, "Bandwidth selection for kernel density estimation: a review of fully automatic selectors," *AStA Advances in Statistical Analysis*, pp. 1–31, 2013.

[105] R. Bartels, J. Beatty, and B. Barsky, "Hermite and cubic spline interpolation," *An Introduction to Splines for Use in Computer Graphics and Geometric Modelling*, pp. 9–17, 1998.

[106] "Matlab gui," http://www.mathworks.com/discovery/matlab-gui.html, accessed: Aug 20, 2013.

[107] "Elastix," http://elastix.isi.uu.nl/, accessed: Feb. 21, 2013.

[108] "Ixi mra dataset," http://biomedic.doc.ic.ac.uk/brain-development/index.php?n=Main.Datasets, accessed: April 01, 2013.

[109] N.-P. V. Nielsen, J. M. Carstensen, and J. Smedsgaard, "Aligning of single and multiple wavelength chromatographic profiles for chemometric data analysis using correlation optimised warping," *Journal of Chromatography A*, vol. 805, no. 1, pp. 17–35, 1998.

[110] C. D. Manning, P. Raghavan, and H. Schütze, *Introduction to information retrieval*. Cambridge University Press Cambridge, 2008, vol. 1.